BROADBAND PLASMONIC ABSORBERS FOR SUNLIGHT PHOTOCATALYSIS

TAN FURUI

Ph.D

The Hong Kong Polytechnic University

2017

THE HONG KONG POLYTECHNIC UNIVERSITY

DEPARTMENT OF APPLIED PHYSICS

BROADBAND PLASMONIC ABSORBERS FOR SUNLIGHT PHOTOCATALYSIS

TAN Furui

A thesis submitted in partial fulfilment of the

requirements for the degree of Doctor of Philosophy

August 2015

CERTIFICATE OF ORIGINALITY

I hereby declare that this thesis is my own work and that, to the best of my knowledge and belief, it reproduces no material previously published or written, nor material that has been accepted for the award of any other degree or diploma, except where due acknowledgement has been made in the text.

____________________________________ (Signature)

Furui Tan (Name of candidate)

ABSTRACT

Recently, plasmonic photocatalysis has been regarded as a very promising technology since the localized surface plasmon resonance (LSPR) effect of noble metal nanoparticles (NPs) can boost up the utilization of visible light significantly. As the visible light takes up about 43% of solar energy, plasmonic photocatalysis increases the prospect of sunlight for environmental and energy applications such as water treatment, water splitting and photosynthesis. Plasmonic resonance of the noble metal NPs can enhance the visible response of wide bandgap photocatalysts like TiO_2 drastically, but the current technology has two fundamental problems: narrow absorption band and low absorption, which limit the efficiency of photocatalysis using sunlight energy.

In this study, different types of hybrids based on TiO_2 are designed, fabricated and characterized with the aims to enhance the absorption, to improve the charge carrier separation and transfer, and subsequently to enhance the photoreactivity under the irradiation of visible light. In this thesis, original work focuses on a couple of broadband plasmonic absorbers. In the first work, a TiO_2-Au bilayer that consists of a rough Au film under a TiO_2 film is investigated using the atomic laser deposition (ALD) method. This TiO_2-Au bilayer aims to enhance the photocurrent of TiO_2 over the whole visible region and is a novel attempt to use rough Au films to sensitize TiO_2. Experiments show that the bilayer structure gives the optimal optical and photoelectrochemical performance when the TiO_2 layer is 30 nm thick, measuring the absorption 80% – 90% over 400–800 nm and the photocurrent intensity of 15 $\mu A \cdot cm^{-2}$, much better than those of the TiO_2-AuNP hybrid (i.e., Au NPs covered by the TiO_2 film) and the bare TiO_2 film. The superior properties of the TiO_2-Au bilayer can be attributed to the plasmonic resonance of the rough Au film as the hot electron generator and the photoactive TiO_2 film as the electron accepter. Although this TiO_2-Au bilayer exhibits excellent photocatalytic activity, the fabrication complexity and the relative low electron transfer from the device to the electrolyte limit its large-scale applications. The second work further proposes and investigates another broadband plasmonic absorber with a sandwich structure that makes use of the combined plasmonic effects of the rough Au surface (100 nm thick) and the random Au NPs that are separated by a 150-nm TiO_2 layer made by the sol-gel method. The absorber measures a strong absorption (72% – 91%) over 400 – 900 nm and significantly enhances the photocurrent (by 20 folds) as compared to the bare TiO_2 film. The FDTD simulations have proved the broadband strong absorption is the result of interaction of rough Au film and TiO_2 film.

In summary, novel broadband plasmonic absorbers have been introduced to help improve the performance of the photocatalysis under visible light, such as the visible light absorption and the generation and transfer of electrons and holes. These broadband plasmonic absorbers, as excellent photoelectrodes, may find niche applications in solar photocatalysis and may also be promising for large-scale industrial applications with a long-term stability.

LIST OF PUBLICATIONS

Journal Publications

1. **F. R. Tan**, N. Wang, D. Y. Lei, W. X. Yu and X. M. Zhang, Plasmonic black absorbers for enhanced photocurrent of visible-light photocatalysis, Advanced Optical Materials (accepted). (**Back cover**) *DOI: 10.1002/adom.201600399.* IF: 5.108

2. **F. R. Tan**, T. H. Li, N. Wang, S. K. Lai, C. C. Tsoi and X. Ming Zhang, Rough gold films as broadband absorbers for plasmonic enhancement of TiO_2 photocurrent over 400 – 800 nm, Scientific Reports, vol. 6, paper no. 33049, 9 Sep 2016. *DOI: 10.1038/srep33049.* IF: 5.578

3. N. Wang, **F. R. Tan,** Y. Zhao, C. C. Tsoi, X. D. Fan, W. X. Yu and X. M. Zhang, Optofluidic UV-Vis spectrophotometer for online monitoring of photocatalytic reactions, Scientific Reports, vol. 6, paper no. 28928, 29 Jun2016. *DOI:10.1038/srep28928.* IF: 5.578

4. N. Wang, **F. R. Tan**, L. Wan, M. C. Wu and X. M. Zhang, Microfluidic reactors for visible-light photocatalytic water purification assisted with thermolysis, Biomicrofluidics, vol. 8, no. 5, pp. 54122, 24 Octorber (2014). IF: 3.357

4. S. K. Lai, C. Xie, K. S. Teng, Y. Y. Li, **F. R. Tan**, F. Yan, and S. P. Lau, Polymeric Carbon nitride nanosheets/graphene hybrid phototransistors with high responsivity. Advanced Optical Materials, *DOI:* 10.1002/adom.201500662. IF: 5.106

5. S. Cao, T. S. Wang, J. L. Zhao, **F. R. Tan**, X. M. Zhang, and W. X. Yu, Hierarchic random nanosphere model for broadband solar energy absorbers. Optical Material Express, vol. 5, 2777 (2015). IF: 2.84

Conference papers

1. **F. R. Tan**, N. Wang, X. M. Zhang, Plasmonic black absorbers for solar photocurrent enhancement, Young Giants of Nanoscience 2016, May 29 – 2 June 2016, Hong Kong, paper P-020.

2. **F. R. Tan,** N. Wang, S. Cao, Q. Q. Liang, W. X. Yu and X. M. Zhang, Plasmonic blackbody absorber for photocatalytic microreactors, The 5th International Conference on Optofluidics (**Optofluidics 2015**), 26 – 29 July 2015, Taipei, Taiwan.

3. **F. R. Tan,** N. Wang, S. Cao, Q. Liang, W. X. Yu, X. M. Zhang, Visible-light photocatalysis using plasmonic coupling effect for optofluidic microreactors, Symposium on Design, Test, Integration and Packaging of MEMS/MOEMS (**DTIP 2015**), 27 - 30 April 2015, Montpellier, France.

4. **F. R. Tan**, N. Wang and X. M. Zhang, Visible-light photocatalysis using plasmonic coupling for optofluidic microreactors, The 4th International Conference on Optofluidics (Optofluidics 2014), 28-30 August 2013, Guangzhou, China, P08.

5. **F. R. Tan**, N. Wang and X. M. Zhang, Bubble microreactors for photocatalytic water treatment, The 3rd International Conference on Optofluidics (Optofluidics 2013), 15-

17 August 2013, Hong Kong, paper P22, pp. 113-114.

6. N. Wang, **F. R. Tan**, C. C. Tsoi and X. M. Zhang, Microfluidic reactors for photocatalytic conversion of solar energy into chemical energy, The 8th International Symposium on Microchemistry and Microsystems (**ISMM2016**), 30 May – 1 June 2016, Hong Kong.
7. N. Wang, **F. R. Tan**, C. C. Tsoi and X. M. Zhang, Integrated optofluidic device with on-chip UV-Vis spectrophotometer for online monitoring of photocatalytic reactions, The 8th International Symposium on Microchemistry and Microsystems (**ISMM2016**), 30 May –1 June 2016, Hong Kong.
8. N. Wang, **F. R. Tan**, Y. Liu and X. M. Zhang, Photocatalytic water purification using microfluidic platform, The IWA Nano and Water Regional Conference (**IWA2015**), Dalian, China, 20 – 23 May 2015, paper O27.
9. N. Wang, **F. R. Tan,** C. C. Tsoi and X. M. Zhang, Optofluidic microreactors for visible-light photocatalysis, The Conference on Lasers and Electro-Optics (**CLEO2015**): Laser Science & Applications, 10 – 15 May 2015, San Jose, CA, USA, paper AW4K.3.
10. N. Wang, **F. R. Tan** and X. M. Zhang, Optofluidics microreactors for photocatalytic water purification, The 4th International Conference on Optofluidics (**Optofluidics 2014**), 28 – 30 August 2014, Guangzhou, China, paper P06 (**Best Poster Awards**).
11. N. Wang, N. Y. Chan, C. H. To, **F. R. Tan** and X. M. Zhang, Photocatalytic microreactors for water purification: Selective control of oxidation pathways, The 8th Annual IEEE International Conference on Nano/MicroEngineered and Molecular

Systems (**IEEE NEMS 2013)**, 7-10 April 2013, Suzhou, China, pp. 368 – 371.

12. N. Wang, **F. R. Tan** and X. M. Zhang, Photocatalytic water purification using planar microreactor, Photonics Global Conference **(PGC 2012)**, 13-16 December 2012, Singapore, paper 3-2G-5.

ACKNOWLEDGMENTS

I would like to express my sincerest appreciation to my chief supervisor **Dr. Xuming Zhang** and co-supervisor **Prof. Jiyan Dai** in Department of Applied Physics in The Hong Kong Polytechnic University. Without their excellent guidance, constant encouragement and support during the past three years of my PhD study, it would be impossible for me to complete my research work. Their high standard, profound academic insight and inspired discussions contribute greatly to improve the quality of my doctorial research.

I would also like to thank Prof. Shu Ping Lau, Dr. Haitao Huang and Dr. Dangyuan Lei in Department of Applied Physics in The Hong Kong Polytechnic University for their assistance on my doctorial research.

Besides, I would like to thank all the past and present group members for their great help and friendship, including Dr. Ning Wang, Mr. Terry Chi Chung Choy, Dr. Yang Liu, Mr. Qingming Chen, Mr. Tenghao Li, Ms. Xiaowen Huang and Ms. Yujiao Zhu. Especially, thanks to my friends and colleagues Dr. Lili Tao, Mr. Shenghua Liu and Mr. Zhiyong Bao for their help in my experiments.

My special gratitude is sent to my husband, Mr. J.B. Zhang, for his great assistance and moral support.

Finally, I would like to thank my parents for their support on my study and life.

TABLE OF CONTENTS

LIST OF FIGURES

List of tables

CHAPTER 1

INTRODUCTION AND LITERATURE REVIEW

1.1 Overview

The growing world population is driving up an urgent need for both clean water and renewable source of energy in recent years. It is well known that many worldwide problems are associated with the lack of fresh and clean water.[1,2,3,4] About 1.2 billion people are suffering from the shortage of healthy drinking water and tens of thousands of people die annually, including 3900 children per day who suffer from the diseases from unhealthy water or human excreta. Both the developing and industrialized nations are facing serious water shortages. According to World Bank statistics, 80% of countries are lack of civil and industrial water. With the rising cost of resources, environmental awareness is increased gradually. Many factories begin to use green technology to minimize carbon emissions and to reduce sewage discharge, for which in the water treatment technology becomes increasingly important.[5,6]

Besides the clean water, another predicament of the human beings is the shortage of renewable energy.[7,8] The total world energy consumption in 2013 (from Wikipedia) indicates that about 77.8% of the primary energy consumption is from fossil fuels (including petroleum, coal and natural gas), 2.6% from nuclear fuels, 19% from renewable resources, of which the main is 9% traditional biomass and 3.8% hydropower (in Figure 1.1). Currently, the world relies heavily on coal, oil and natural gas currently for the energy, all of which are finite and will be depleted someday. Compared to those conventional energy technologies, renewable technologies are able to provide clean energy with much lower environmental impact. Thanks to its high energy capacity and environmental friendliness, hydrogen has been regarded as an excellent and promising energy transfer medium.

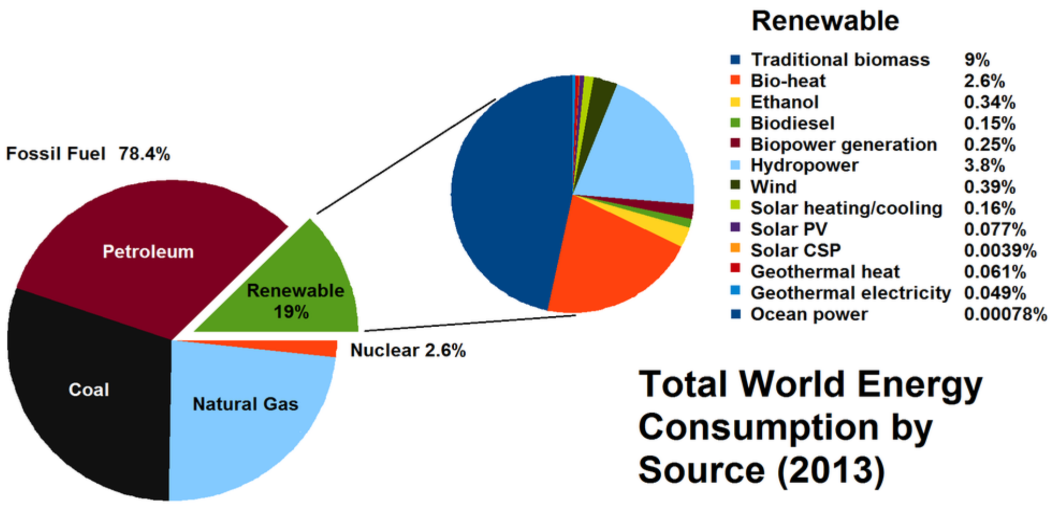

Figure 1.1 The source distribution of total world energy consumption in 2013, from Wikipedia.

If the hydrogen is derived from hydrocarbons (mainly including the biomass and the fossil fuels), nitric oxide, CO and some other pollution gases will bring a heavy burden to the environment.[9,10,11] On the other hand, hydrogen energy obtained from water will not bring the undesirable side effect, however, an external resource is needed for energy supply. If hydrogen can be generated from some renewable energy sources such as solar energy, it would be ideal for green energy.

In order to satisfy the booming demand for clean water and to improve the deteriorating water supply in contemporary society, we need to develop a progressive and cost-effective water treatment technology to recycle and reuse wastewater, at the same time, to avoid more serious pollution. Meanwhile, another urgent issue is to satisfy the increasing need. As we known, solar and wind powers are two major renewable energy sources, both of which are abundant.[12,13] However, they only take a very few percentage of the current world energy consumption (0.08% for solar and 0.39% for wind), inferring a huge potential for further development. (see in Figure 1.1). For example, the global energy consumption in 2010 is 1.6 TW while the total solar energy at the earth's surface is 1.3×10^5 TW. The difference is by roughly four orders of magnitude.[14,15]

Recently the capture of solar energy for useful purposes has attended more and more attention in the scientific and engineering world. The potential utilization of solar energy to purify wastewater and to produce renewable hydrogen source, is a goal pursued worldwidely.[16,17,18,19] Efficient utilization of solar energy could alleviate many environmental and energy issues simultaneously.

In 1972, the photocatalysis of water was first reported by Honda and Fujishima by using TiO_2 electrodes. Those days were known as the time of "oil crisis" since the crude oil experienced a sudden price rise and was facing future shortage. Photocatalysis has demonstrated potential applications in extensive areas such as recycling polluted water or air, converting solar energy, and so on.[20,21] Therefore, that report has attracted many scientists in a broad area to conduct numerous studies since then.

The working principle of the photocatalysis is simple. When the semiconducting photocatalyst (TiO_2, ZnO et al.) absorbs photons from sunlight, it will produce active electrons and holes, which can then initiate the reduction and/or oxidation of chemicals. The holes can oxidize organic pollutants and certain bacteria, and turn the wastewater into clean water (Figure 1.2(a)). On the other side, the electrons can be used for reduction reactions, for instance, $2H^+ + 2e^- \rightarrow H_2$ (gas), which has been considered as one of the most promising approaches to obtain hydrogen with solar energy. Over the past 40 years, many photocatalysts have been reported to exhibit excellent photocatalytic properties for water splitting, which results in a stoichiometric mixture of H_2 and O_2 (2:1 by molar ratio) under the irradiation of the ultraviolet (UV) light.[22,23,24,25] A diagram of photocatalytic hydrogen generation system is shown in Figure 1.2(b).

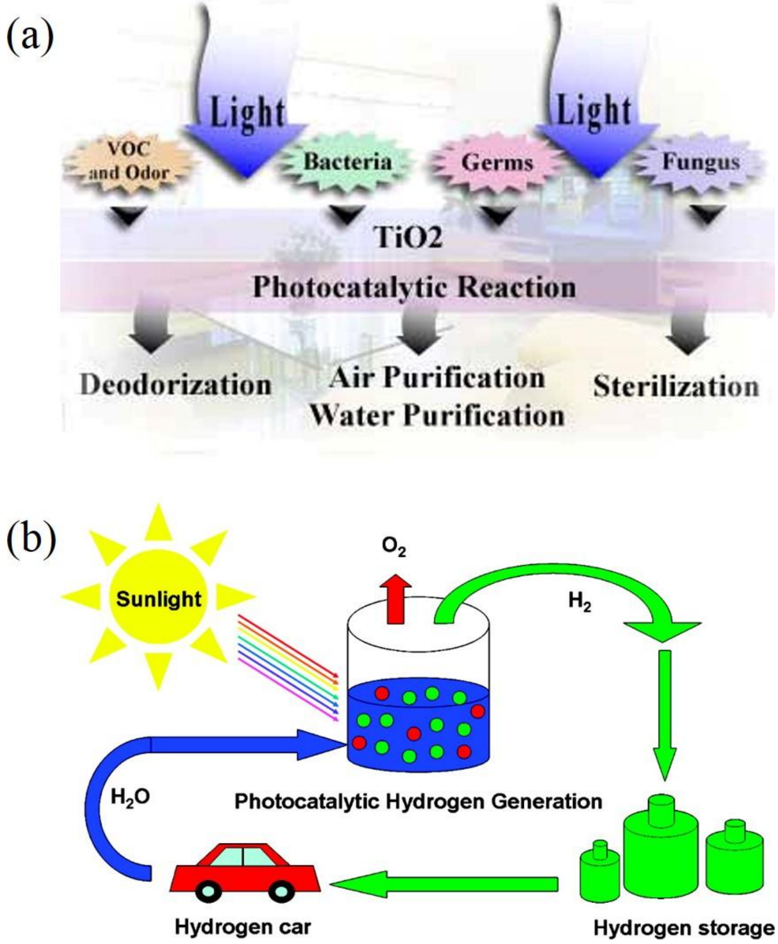

Figure 1.2 Schematic diagram of (a) photocatalytic degradation (from http://gamma-nano.ca/what-is-a-photocatalyst/) and (b) photocatalytic hydrogen generation application.[22]

Photocatalysis realizes direct solar-to-electric conversion, which stores the solar energy in chemical bands and then releases it without harmful byproducts, mainly CO_2 and H_2O. The photocatalysis has been used in a broad range of research areas, including air purification, electric appliance, residence, et al. (see in Figure 1.3). Its achievements in environmental and energy-related fields are most attractive.[26,27,28,29]

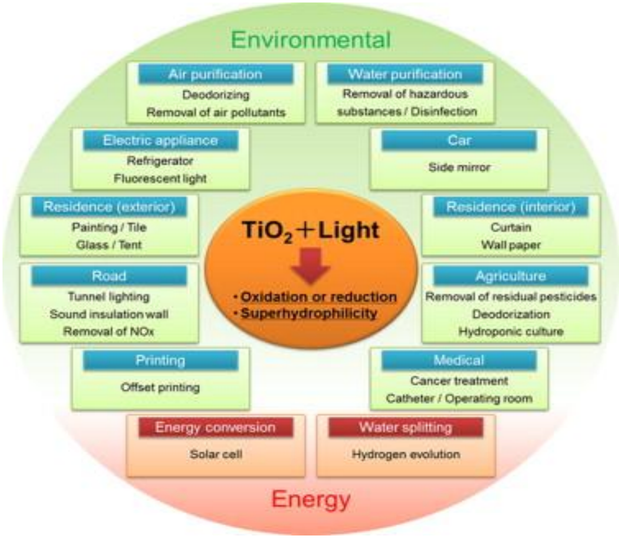

Figure 1.3 Application of TiO_2 photocatalysis.[26]

The traditional photocatalysts, mainly the semiconductor metal oxides including TiO_2 and ZnO, are demonstrated to store the solar energy in forms of chemical energy under the UV illumination, but not under visible illumination.[30,31] Actually, the incident solar light on the Earth's surface consists of ~5% UV, ~43% visible, and ~52% infrared.[32] Although solar energy provides an abundant resource for energy alternative, the UV light takes up only a small portion of the irradiated solar energy, whereas the visible and infrared lights contribute to the major part. Thus, the utilization of natural solar light for a photocatalytic or photoelectrochemical process can enhanced by enabling the response of photocatalyst to the visible range. Recently, the need for efficient utilization of sunlight has sparked more and more research interest in the visible-light photocatalysis. Many researchers have been focusing on the studies of better visible-light-responsive photocatalysts.[33,34,35]

One of the most popular photocatalysts is TiO_2. It has a bandgap of ~3.2 eV and has an absorption cut-off wave length of ~ 380 nm. Considering the solar spectrum, it indicates that a very small amount of solar photons (< 380 nm) can be utilized to drive TiO_2, while most solar photons in a wide wavelength range (> 380 nm) are wasted. Therefore, an effective visible-light-responsive photocatalyst is essential to harvesting the solar energy as much as possible. Although TiO_2 is limited to its short cut-off wavelength and works under UV irradiation only, it is still one of the most promising photocatalysts due to its many benefits such as chemical stability, non-toxicity, and so on. Many attempts have been made to extend the short cutoff wavelength of TiO_2, including doping addition and defect creation. These result in a slight enhancement in the absorption of visible light, but still leave the majority of the solar spectrum invalid.[34,35] Till now, much research progress has been made to develop visible-light-responsive TiO_2, but largescale applications in the environment and energy are still rare.

1.2 Organization and Objectives

The photocatalysis utilizes solar light to oxidize organic contaminants in wastewater or to initiate water splitting to produce hydrogen energy, both of which are fast developing applications. The combination of solar light and photocatalysis has turned out to be a technology with great promise. Although a number of photocatalysts have been reported, many challenges still remain in improving the energy conversion efficiency, such as utilizing photons of longer wavelength, increasing the lifetime of photogenerated charge carriers in the semiconductor materials. It is the objective of this thesis to design, fabricate and study the plasmonic photocatalysts in wide wavelength range in the solar spectrum.

In Chapter 1, an investigation that are responsive to the current demand of clean water and renewable energy is presented and the developing potential of photocatalysis with solar light is discussed. The organizations and objectives of the thesis are also described in this chapter.

Chapter 2 expounds the mechanism of photocatalysis and presents a literature review on the current TiO_2-based photocatalysis under visible light. In the survey, the development of different strategies to modify TiO_2 for the utilization of visible light are compared. The physical mechanisms and advantages of plasmonic photocatalysis will be identified. Additionally, the background on TiO_2 structural property and electron is properties for photocatalysis is presented, and the optical properties of noble metal NPs are discussed as well. The motivation of this thesis is also presented in this chapter.

Chapter 3 presents the fabrication processes and characterization methods of plasmonic photocatalysts. The fabricated films are characterized by XRD, AFM and SEM. The UV-vis absorption spectra are measured to detect the light absorption ability of these absorbers in the visible range, while the FDTD method is introduced to simulate the absorption and the electromagnetic field of these absorbers. Their photocatalytic activities are measured using a three-electrode system.

Chapter 4 presents the experimental study of a novel broadband plasmonic absorber for photocatalysis. The thin film TiO_2 photocatalysts are prepared by the ALD method to obtain the TiO_2-Au bilayer, which can overcome the limitations of the traditional noble metal-doped TiO_2. The absorption and photocatalytic efficiency of three TiO_2-based structures are compared and investigated. Particularly, the absorption spectrum of the TiO_2-Au bilayer is flat over the whole range of 400 – 800 nm, with the minimum absorption of 80% and the maximum 90%, as compared to the bare TiO_2 film and the TiO_2-AuNP hybrid (Au NPs covered by the TiO_2 film). When the TiO_2 layer is 30 nm thick, the TiO_2-Au bilayer structure exhibits the strongest absorption and the best photoactivity. The photocurrent intensity of the TiO_2-Au bilayer is 15 $\mu A \cdot cm^{-2}$, much better than those of the TiO_2-AuNP hybrid and the bare TiO_2 film.

Based on the previous photocatalyst, Chapter 5 reports another advanced design of plasmonic absorber made by the sol-gel method, which is easy for the fabrication of large-scale TiO_2 films. This plasmonic blackbody-like absorber is made of a three-layer nanostructure that sandwiches a thin TiO_2 film layer between a rough gold film and a gold nanoparticle layer. As a result, the photocatalytic performance of TiO_2 is enhanced in the whole visible range. The absorber achieves an absorption above 80% in the wavelength range of 400-900 nm, matching well with the electromagnetic simulations. The order of photocurrent response is Au NPs/TiO_2-Au film > TiO_2/Au film > Au NPs/TiO_2 > the bare TiO_2 film, which is in good agreement with the prediction based on the measured absorption spectra.

In Chapter 6, a general conclusion is drawn to sum up the limitations of photocatalytic efficiency overcome by our plasmonic absorbers. The recombination of photo-excited electrons and holes, may be eliminated to achieve better visible-light photocatalysis. The future work is also proposed in this chapter.

CHAPTER 2

BACKGROUND of PLASMONIC Photocatalysis

This chapter will review the basic principles of photocatalysis and the major mechanisms of plasmonic photocatalysis. It provides the base of physical understandings for the following chapters, which will elaborate my studies of new broadband plasmonic absorbers.

2.1 Fundamentals of semiconductor-based photocatalysis

2.1.1 Principle of photocatalysis

Since the 1970s, the development of semiconductor photoelectrochemistry has gained extensive knowledge that greatly assisted the development of photocatalysis.[36,37,38] Photocatalysis is the acceleration of the oxidation and reduction reaction with the presence of photocatalyst and light. According to the phase of the photocatalysts and reactants, photocatalysis can be mainly divided into two types: homogenuous photocatalysis and heterogeneous photocatalysis. In a homogeneous photocatalysis system, the reactants exist in the same phase as the photocatalysts. The most popular homogeneous photocatalysts include the ozone and the photo-Fenton systems (Fe^+ and Fe^+/H_2O_2).[39,40] In a heterogeneous photocatalysis system, the catalyst is in a different phase from the reactants and the photo-induced reactions occur at the surface of the catalyst. The photocatalytic substrate excites the initial photons and then transfers an electron or energy into the reactants. Subsequently, the transferred electron or energy causes the chemical reactions during the process of the heterogeneous photocatalysis. The surface reactive site or a molecular can be a reactive center.[27,41] Till now, the popular heterogeneous photocatalysts are mainly transition metal oxides and semiconductors, which have their unique characteristics. Different from the metals with continuous electron states, the semiconductor possesses a void energy region named as the bandgap, which lays between the conduction band with higher energy and the valence band with lower energy. When the semiconductor absorbs a photon with energy equal to or greater than its bandgap, an electron is excited from the valence band to the conduction band, leaving a positive hole in the valence band. The excited electron and hole can then initiate the reduction and/or oxidation of chemicals. At present, photocatalysis is useful in a wide range of applications, for example, wastewater treatment, water splitting, air purification, self-cleaning surface, et al.

2.1.2 Fundamental Mechanism of TiO_2 photocatalyst

Since 1977, when Frank and Bard first introduced TiO_2 to decompose cyanide in water, more and more researchers have focused on its environmental applications.[42,43] In particular, TiO_2 turns out to be an excellent photocatalyst to break down organic compounds. If the catalytically active TiO_2 powder is taken into a shallow pool with sewage water and is illuminated under solar light, the water will be purified gradually.

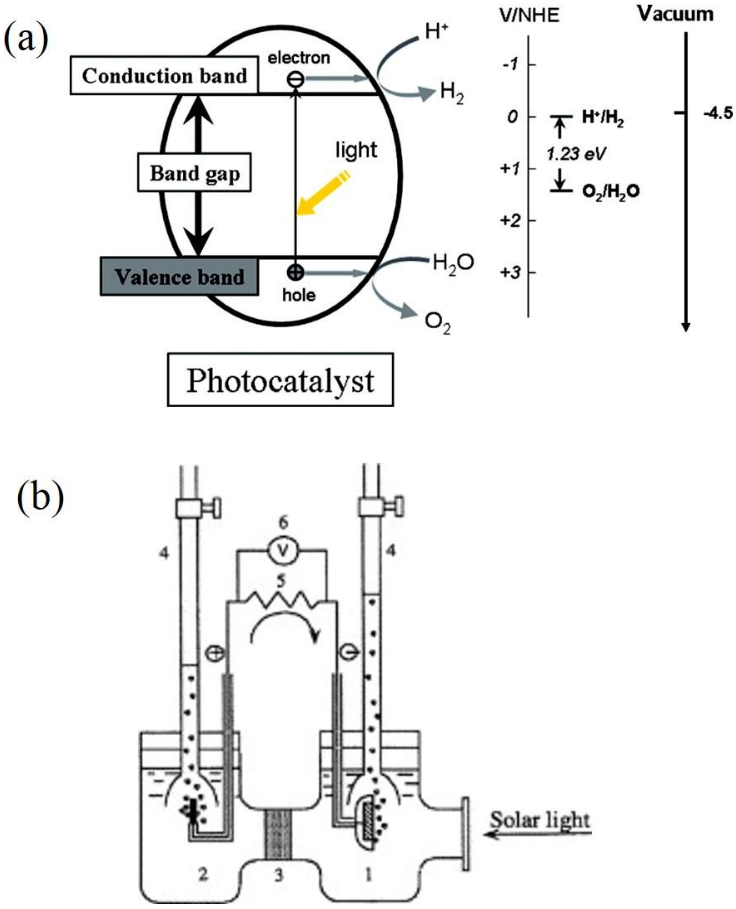

Figure 2.1 (a) Schematic representation of a photoelectrochemical cell.[20,22] (b) Fundamental photocatalytic principle of water splitting for hydrogen production.[44]

In Fujishima and Honda's pioneering work, the water was deposited into hydrogen and oxygen with an electrochemical cell, as shown in Figure 2.1 (a). Ever since, the semiconductor TiO_2 has been utilized widely as a photocatalyst to transform the solar energy into chemical energy. The formation of photogenerated charge carriers (hole and electron) initiates a series of reductive and oxidative reactions on the surface of semiconductors. Figure 2.1 (b) describes the formation mechanism of the charge carrier when the TiO_2 particle is irradiated with sufficient photon energy ($h\nu$). When the photons with energy greater than or equal to the bandgap energy of TiO_2 are irradiated onto the surface, the lone electron (e^-) will be excited to the empty conduction band in femtoseconds, leaving a positive hole (h^+) in the valence band.[44] A chain reactions of oxidative and reductive processes take place on the surface activated by photons, which is widely postulated as following equations:

Photoexcitation: $TiO_2 + h\nu \rightarrow e^- + h^-$ (2.1)

Charge carriers can be trapped in the defects of Ti^{3+} and O^- sites in the TiO_2 lattice, or they also may recombine and dissipate the energy by heat (Eq. 2.2).

$e^- + h^+ \rightarrow$ energy (2.2)

Alternatively, the electrons migrated to the catalyst's surface without recombination can reduce the adsorbates while the holes can oxidize them, which are the basic photocatalytic mechanisms for waste water purification and hydrogen production by water splitting method, respectively.[12]

(i) For the water purification

On one side, the positive holes can oxidize OH^- or water on the surface to produce hydroxyl (·OH) radicals, which are extremely powerful oxidants (Eq. 2.3) that can subsequently oxidize the pollutants into some mineral salts, CO_2 and H_2O (Eq. 2.4).

$H_2O + h^+ \rightarrow \cdot OH + H^+$ (2.3)

$\cdot OH + \text{pollutant} \rightarrow \rightarrow \rightarrow H_2O + CO_2$ (2.4)

On the other side, the negative electrons in the conductive band can be captured by the adsorbed oxygen molecules on the TiO_2's surface, which may be reduced into superoxide radical anions ($O_2\cdot^-$) (Eq. 2.5). Those $O_2\cdot^-$ radical will further react with H^+ to produce hydroperoxyl (·OOH) radical (Eq. 2.6). These relative $O_2\cdot^-$ and ·OOH radical species may also contribute to the degradation of pollutant into mineral salts, CO_2 and H_2O (Eq. 2.8 and 2.9). Besides, the further electrochemical reduction of ·OOH may yield H_2O_2, which contributes to the pollutant degradation to some extend (Eq. 2.7).

$$O_2 + e^- \rightarrow O_2\cdot^- \tag{2.5}$$

$$O_2\cdot^- + H^+ \rightarrow \cdot OOH \tag{2.6}$$

$$\cdot OOH + \cdot OOH \rightarrow H_2O_2 + O_2 \tag{2.7}$$

$$O_2\cdot^- + \text{pollutant} \rightarrow \rightarrow \rightarrow CO_2 + H_2O \tag{2.8}$$

$$\cdot OOH + \text{pollutant} \rightarrow \rightarrow \rightarrow CO_2 + H_2O \tag{2.9}$$

(ii) For the hydrogen production by water splitting

Hydrogen production from photocatalytic water splitting is also a representative application for redox catalysis. To split water into hydrogen and oxygen, the level of the conductive band should be more negative than that of the hydrogen production ($E_{H+/H2}$) while the valence band should be more positive than the oxidation level of water ($E_{O2/H2O}$) as shown in Figure 2.1 (b). The water oxidation reaction is presented in Eq. 2.10, while the water reduction is in Eq. 2.11. In theory, semiconductors satisfied the requirement mentioned above can be used as photocatalysts to split water into hydrogen and oxygen.

$$4OH^- + 4h^+ \rightarrow 2H_2O + O_2 \tag{2.10}$$

$$4H^+ + 4e^- \rightarrow 2H_2 \tag{2.11}$$

2.1.3 Semiconductor photocatalysts and their characteristics

Currently, most photocatalysts are chosen as n-type semiconductors, which depend on their unique optical characteristics. Figure 2.2 provides energy band positions of several photocatalytic semiconductors used commonly, including TiO_2, ZnO, CdS, CdSe. Among them, some photocatalysts with narrow bandgaps, like some sulfides (CdS, etc.), are attractive photocatalytic materials to transfer solar energy into chemical energy under visible-light illumination, which is beneficial for both water purification and water splitting.[45] Generally, as compared to the bandgap counterparts, these visible-light-responsive materials have the conductive band edge more negative than the potential level required for the reduction reaction. However, these low-bandgap chalcogenide semiconductors still suffer from several limitations such as low stability. For a photocatalyst material, the stability and durability under irradiation are the fundamental prerequisites, especially in the aqueous phase. Take CdS for example, the CdS particles tend to aggregate and form larger particles, which reduce the surface area and lead to an increased recombination rate of the photo-induced electron-hole pairs. As a result, these CdS particles cannot maintain the photoactivity over a long time. Many efforts have been made to solve these problems, including the preparation of quantum-sized CdS, the fabrication of heterogeneous semiconductors, and the corporation of semiconductor particles in the interlayer region of layered compounds, all of which turn out to be complex. In general, these metal sulfides are not ideal for photocatalysis though they exhibit a high initial photocatalytic activity.[46,47] Among these photocatalysts, TiO_2 stands out as the most effective photocatalyst thanks to its excellent properties such as low cost, high thermal and photonic stability, non-toxicity, chemical and biological inertness, making it close to an ideal photocatalyst. It has been extensively used in wastewater treatment and water splitting applications.

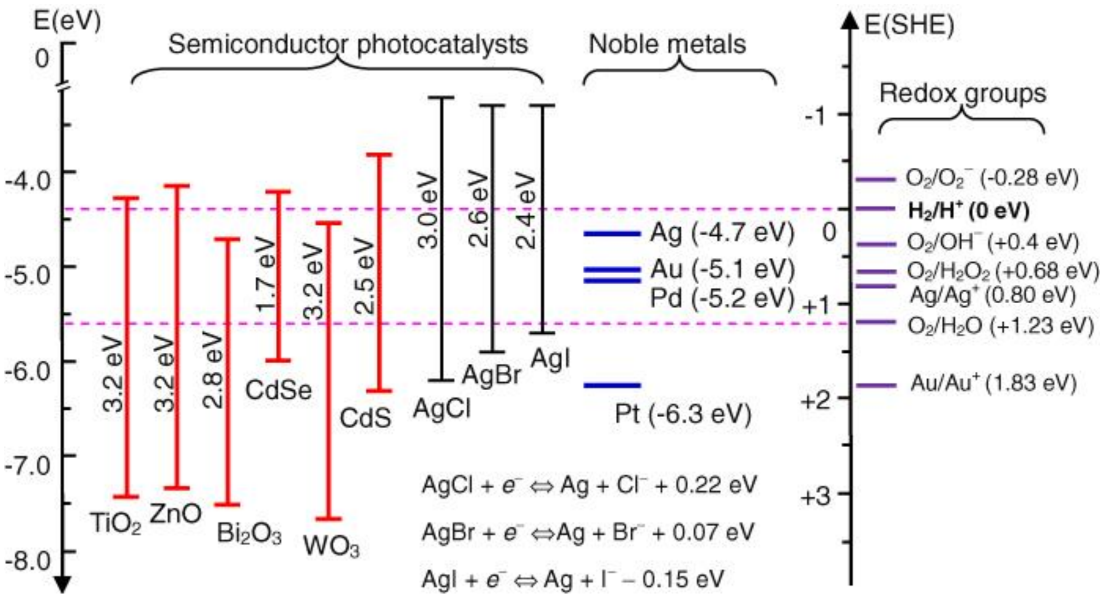

Figure 2.2 Energy band position of several popular photocatalysts, including the valence and conductive bands of the semiconductor, the work functions of the noble metals and the electrochemical potentials of the redox groups.[48]

2.2 Strategies for visible-light-responsive TiO_2 photocatalysts

Among various photocatalysts, TiO_2 is the most popular one because of its strong catalytic activity and high chemical stability. However, there are still two main limitations:

large bandgap and fast recombination. Since the bandgap of TiO_2 are usually 3.2 eV (anatase) or 3.0 eV (rutile), the light wavelength with energy greater than its bandgap is usually $\lambda < 400$ nm, thus the visible light is not effective. In addition, the photo-generated electron-hole pairs are unstable due to fast recombination. As a result, the energy conversion efficiency of TiO_2 photocatalyst is still low at present. To achieve a fundamental enhancement of the photocatalytic efficiency based on the bare TiO_2 under visible light irradiation, two problems must be overcome. One issue is how to produce more photo-excited electrons and holes; another is how to separate these electrons and holes efficiently. To make the normal UV-active TiO_2 become visible-light-responsive, various modification strategies have been carried out, such as impurity doping (chemically and physically), semiconductor coupling, dye sensitization, etc.[34,49,50] After the incorporation of a small quantity of components such as ions and metal oxides, the TiO_2 photocatalyst shows an increased absorption of the visible light and also an enhanced photocatalytic efficiency under the visible light illumination. The doped TiO_2 usually exhibits considerable photocatalytic activity for the degradation of organic pollutants and even for water splitting upon visible light illumination. The fundamental mechanisms, current developments, advantages and disadvantages of these methods for visible-light-responsive TiO_2 photocatalysts are discussed in the following section based on the three categories: chemical doping, physical doping and plasmonic enhancement.

2.2.1 Visible-light-responsive TiO_2 photocatalysts by chemical doping

Various chemical synthesis methods are used for the doping of TiO_2, which can mainly be divided into metal doping and non-metal doping.[36] After the incorporation of small amounts of ions, the visible light-responsible TiO_2 photocatalysts can be prepared.

(i) Non-metal Ion Doping

Dye photosensitization has been demonstrated to be one of the most efficient approaches to expand the TiO_2's photoresponse to the visible region.[51] The visible-light photon absorbed by a dye excites an electron from the highest occupied molecular orbital (HOMO) to the lowest unoccupied molecular orbital (LUMO). Subsequently, the excited electrons are transferred to the conduction band of TiO_2, leaving the dye in the cationic radical state. The TiO_2 functions as a mediator to transfer electrons from the sensitizer to the proximate substrate. As electron acceptors, the valence band of TiO_2 remains unaffected. This electron injection depends on the character of the sensitizer, the semiconductor, and the interaction between them.[52] The photosensitizers mainly include fluorescein derivative, ruthenium pyridine complex, erythrosine B, eosin, leaf green acid, rose red and so on. Although the photosensitive photocatalyst has been extensively conducted in research, some disadvantages still exist: (1) the adsorption sites of the semiconductor material is reduced since a large surface area is occupied by the sensitizer; (2) the photosensitizer is easy to fall off the surface of the catalyst, leading to a decreased photosensitive capacity. Besides, there is often some secondary contamination when the contaminants is degraded in sewage water.[53]

Since the nitrogen-doped TiO_2 was reported to exhibit excellent visible light absorption and photocatalytic activity by Asahi et al. in 2001, nitrogen has become one of the most promising dopants because of its comparable atomic size with oxygen.[52] Some other non-metal, such as carbon, fluorine, phosphorous and sulphur with a similar atomic radius to that of the oxygen atom, have also been attempted to dope TiO_2 and have shown improvement for visible light activity.[54,55,56] Compared with those bulk modifications, surface modifications seem preferable mainly because these doping ions in the underneath crystalline lattice may serve as recombination centers, which may decrease the photocatalytic activity.[57,58]

(ii) Metal Ion doping

Since the magnitude of TiO_2's bandgap is a crucial factor to determine the utilization efficiency of the visible light, the modification of the bandgap is expected to remarkably enhance the formation of electrons and holes. An appropriate amount of metal ions doped into TiO_2 can introduce electron capture centers as well as some defects due to the changed crystallinity of TiO_2, which would decrease the recombination probability of the electron and hole. Therefore, metal ion doping is recognized as an effective modification approach to obtain visible-light-responsive TiO_2.

There are three methods to dope metal ions into the TiO_2 matrix. The first method involves transition metal ions. On the early stage, the photocatalytic oxidation of chloroform and the photocatalytic reduction of carbon tetrachloride were set as model reactions, then 21 different transition metal ions were introduced to dope TiO_2 and the photoactivity of these doped TiO_2 were investigated. It found that the TiO_2 doping with Fe^{3+}, Mo^{5+}, Ru^{3+}, Os^{3+}, Re^{5+}, V^{4+}, and Rn^{3+} cations were beneficial for the photodegradation of chloroform.[59,60,61,62] Recently, Yan et al. synthesized Ce^{3+}-doped TiO_2 with the sol-gel method, which generates additional electronic states above the TiO_2's valence band. Consequently, the recombination rate of photogenerated electrons and holes is decreased.[63] The second method involves rare-earth metal ions. A good example is La-doped TiO_2. Sun et al investigated the influence of La-doping on the electronic structure and the photocatalytic activity of TiO_2 using the density function theory. It is found that the enhanced absorption of La-TiO_2 in the visible region is due to the doping La^{3+} rather than the substitution.[64] On the contrary, Anandan et al. suggested that the La^{3+} dopant cations present in the TiO_2 matrix and the ·OH radicals transferred by the surface trapping of excess holes enable to suppress the electron-hole recombination and to realize the rapid mineralization of monocrotophos under visible light irradiation.[65] Recently, some other lanthanide metals, including Yb, Eu, and Sm, are also introduced as the dopants for TiO_2 are to enhance the visible-light photocatalytic activities.[66,67,68] Moreover, some other metal ions, especially Ti(III) self-doping and Sn doping[69], have become a rather hot research topic to dope TiO_2.[70,71] However, the Ti^{3+} centers are easily oxidized into Ti^{4+} by the oxygen dissolved in water, thus the surficial Ti^{3+} centers and oxygen defects are usually not stable on TiO_2. Therefore, most research has been focused on Ti^{3+} self-doped TiO_2 to obtain better stability and higher photocatalytic activity, including the one-step calcination method[72], the vacuum activation method[73] and the one-step solvo-thermal method.[74]

2.2.2 Visible-light-responsive TiO_2 photocatalysts by physical doping

The metal ion-implantation method is an alternative approach for the TiO_2-doping preparation by bombarding TiO_2 photocatalysts with high energy metal ions to modify its electronic properties. This enables to modify the electronic state of TiO_2 by the physical method. Currently, the physical doping methods are focusing on two different modes of ion-implantation techniques： transition metal ion implantation and anion implantation.

(i) Transition metal ion implantation

Metal ion implantation accelerates various transition metal ions (M^+ ion: M= Cr, V, Fe, Mn and Ni) with a high voltage field to bombard the TiO_2, which is then annealled in air. The transition metal ions in the crystal lattice of the titania can form new energy levels between conductive band and valence band, resulting in the absorption shift towards the visible light region.[52,75,76] However, these transition metals may also act as the recombination centers for the photo-excited electrons and holes, resulting in a low quantum efficiency. Especially, among those tested ions, Cr and V are found to be relatively effective to induce a red-shift of the absorption band of TiO_2.[77] Take Cr for example, the implanted Cr ions are stabilized in the lattice of TiO_2 matrix as Cr^{3+} ion, while Cr ions chemically doped within TiO_2 exist as the mixture of tetrahedrally and octahedrally coordinated Cr-oxide species (Cr_2O_3-like cluster).[78,79] The ion-implantation method enhances the stability of the implanted cations as well as the visible light absorption.

(ii) Anion implantation.

As compared to the transition metal ion implantation, the anion implantation for visible-light-responsive TiO_2 is rather rare. This kind of implanted anions is mostly been limited to the nitrogen anion. Ghicov et al. pointed out the preparation of N-implanted TiO_2 nanotubes and their photocurrent response under the visible light illumination.[77] The re-annealing treatment of N-implanted TiO_2 nanotube layers increases the photocurrent response in the visible light range remarkably since the defect sites contribute to the charge separation within the TiO_2 nanotube structure.

2.2.3 Plasmonic enhanced photocatalysis with TiO_2

In addition to these above mentioned chemical and physical doping methods, the modification of TiO_2 with noble metals has also been used to enhance the visible absorption.[48,80] The noble metal nanoparticles (mainly Au or Ag, in the sizes of tens to hundreds of nanometers) are dispersed into semiconductor photocatalysts to obtain drastic improvement of photoreactivity under UV and/or a extensive range of visible light. For example, the Au nanoparticles (NPs) are able to absorb visible light, different from the TiO_2 absorption towards the UV light. Because of the located surface plasmon response (LSPR) in the Au NPs, the free electrons in Au NPs are driven into a collective oscillation, forming the surface plasmon (SP) states. Since the Au NPs are commonly scattered on the surface of metal oxide, the electrons in SP state will flow into the conductive band of the metal oxide and will be then injected to the surrounding electron acceptors immediately (such as O_2). Simultaneously, the organic substrate will quench the left holes in the Au NPs to finish the photocatalytic cycle. This is the fundamental and distinctive mechanism of plasmonic photocatalysis, which makes active electrons and holes generate in the TiO_2 NPs even without any light absorption by TiO_2. Therefore, the deposition of noble metals on the TiO_2's surface creates a device that gains charge carriers from the LSPR decay, which extends the absorption spectra of TiO_2 well into the visible region.[81,82] The device acts as an electron trap, promotes the interfacial charge transfer and improves the photoactivity of the semiconductor in the visible region apparently.[83] Many recent studies have reported plasmonically-driven pollutant degradation and solar water-splitting process to evolve hydrogen.[33,84,85]

2.2.4 Comparison of modification strategies for TiO_2-based photocatalysis

Figure 2.3 summarizes the pros and cons of chemical and physical doping methods. For the chemical doping, metal doping or non-metal doping are two complementary approaches that have been most frequently employed to modify TiO_2 into visible light photo-response. However, the metal dopant undergoes corrosion and may cause decay of the photocatalytic performance in a long term. On the other hand, non-metal doping requires harsh preparation conditions and the doping level is difficult to determine using the chemical analyses. Specifically, the doping approach is strongly dependent on the exact preparation procedure and thus an optimal doping level is difficult to obtain. Higher or lower dopant loading can lead to an adverse effect on the photocatalytic activity, causing low reproducibility of the photocatalytic activity. For the above-mentioned physical doping, one approach is to substitute the Ti site with transition metal (Cr, Fe, or Ni).[86] Another approach is to form Ti^{3+} sites by introducing an oxygen vacancy in TiO_2. However, both of the two physical approaches are not widely accepted due to the low chemical stability and reproducibility.[87]

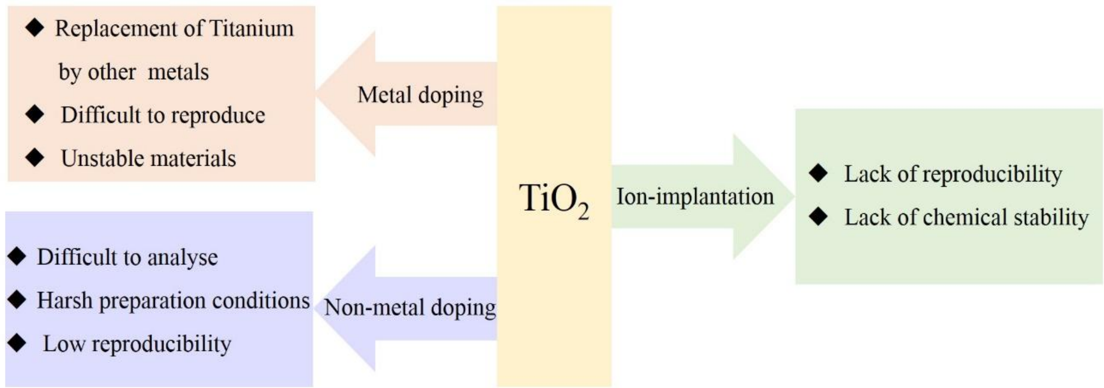

Figure 2.3 Pros and cons of the two alternative doping methods used to achieve visible-light photoresponse in TiO_2.

Compared with the chemical and physical doping methods, the plasmonic photocatalysis possesses two characters— the Schottky junction and the LSPR effect, due to the introduce of the noble metal NPs.[48] These two features bring various benefits for photocatalysis in different aspects. The Schottky junction is caused by the contact of the semiconductor and the noble metal, which builds up an internal electric field in a space-charge region close to the metal/semiconductor interface. The holes and electrons near and/or inside the Schottky junction will be moved towards different directions after the generation. Additionally, the metal part acts as a charge-trap center to provide more active sites for photoreactions and provides a fast lane for charge transfer. The internal electric field and the fast-lane for charge transfer cooperate to suppress the recombination of electrons and holes. The LSPR is the more prominent feature of plasmonic photocatalysis, which brings several significant advantage into the photocatalysis. The major advantages are listed in Figure 2.4. First, the resonance wavelength for Au or Ag NPs can be tailored to be in the visible range or the near-UV range, by tuning the shape, the size or the surroundings of NPs. This makes the large- bandgap photocatalysts be responsive to visible light (e.g., TiO_2). Second, the LSPR can drastically improve the UV absorption of the large-bandgap materials, which is benefiticial for the materials with weak absorption ability. Thirdly, 10 nm under the surface of a thin layer is an efficient absorption distance with the help of LSPR, which is equivalent to the minority length of carrier diffusion (~10 nm). The poor electron transport of some materials can be improved. Lastly, the LSPR enhances the local electric field, that can benefit the photocatalysis in several respects.[88] Specifically, it excites more electrons and holes, which can be better adsorbed by the polarized nonpolar molecules. The heated surrounding environment can further accelerate the redox reaction rate and the mass transfer. Some other effects, such as the quantum tunneling effect and the inherent catalytic effect of the noble metal (e.g. Pt for hydrogen generation), may also contribute to photocatalysis. Every effect has specific requirements. It may not be efficient in one circumstance and some effects may be harmful under certain situations. For example, when the noble metal NPs are embedded deep in the semiconductor photocatalyst and have thus no direct contact with the solution, they will act as charge recombination centers and reduce the photocatalytic efficiency.

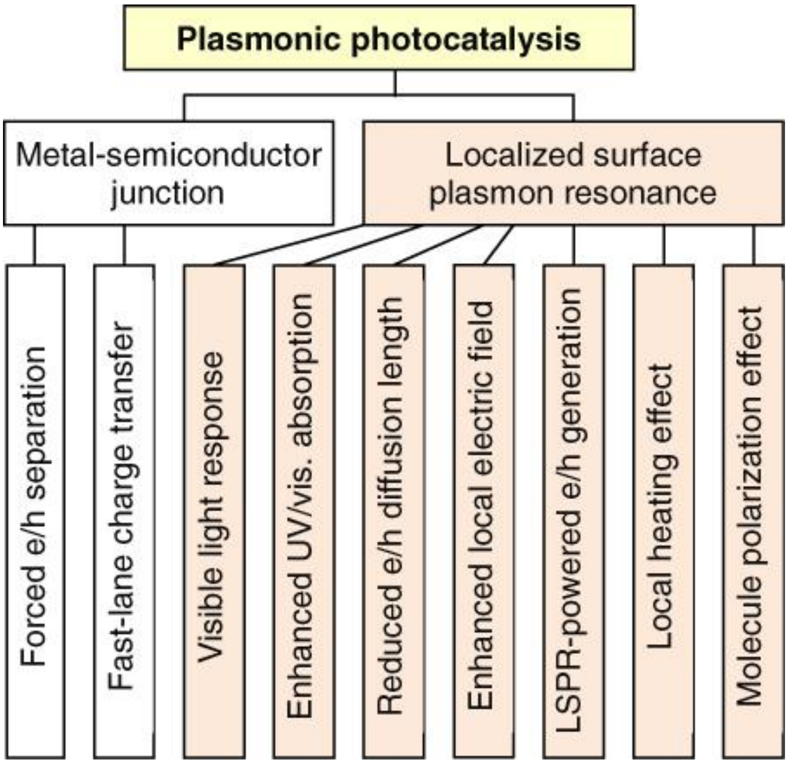

Figure 2.4 Major beneficial effects in plasmonic photocatalysis.[48]

2.3 Plasmonic photocatalysis containing Au NPs and TiO_2

Since the observation that the noble metal NPs can absorb visible light due to the surface plasmonic resonance (SPR), lots of researchers have focused on the synthesis of the plasmonic photocatalyst containing Au NPs and TiO_2 (denoted by Au/TiO_2 hereafter), which can extend the absorption wavelength of TiO_2 from UV light to visible light successfully.[89,90] The Au/TiO_2 owning the SPR phenomenon was first studied by Tatsuma's group. They demonstrated the charge separation at the plasmon-excited Au NPs added into TiO_2 and proved that Au/TiO_2 could lead to methanol and ethanol oxidation as well as oxygen reduction.[91] With the incorporation of plasmonic Au NPs into TiO_2, Liu et al. enhanced the photocatalysis of water splitting by a factor of 66 under the visible-light irradiation.[92] In this pioneering work of the electrode-based plasmonic photocatalyst for water splitting, Tatsuma and Liu revealed that the reduction and oxidation reactions occurred at two spatially separated electrodes. Besides, Silva et al. also studied the plasmonic photocatalytic activity based on Au/TiO_2 to generate H_2 or O_2 from water. By employing a monochromatic laser at 532 nm and a UV cutoff filter ($\lambda >$ 400 nm), they demonstrated that Au NPs serve as a gas evolution center as well as a light harvester in this plasmonic photocatalyst.[93] Additionally, Kewalska et al. fabricated the plasmonic photocatalyst Au/TiO_2 to degrade acetic acid and 2-propanol with high efficiency under light illumination.[57] In addition, Dawson and Kamat synthesized the Au/TiO_2 to enhance the thiocyanate oxidation using a chemical reduction method.[94]

All the above-mentioned Au-based plasmonic photocatalysts have reported an enhanced photocatalytic activity as compared to the bare supporting semiconductor TiO_2. The most probable reason for the observed enhancement of the photocatalytic activity is the SPR of Au NPs, which may accelerate the formation of the charge carriers within the semiconductor. Generally, the material and device geometries of other plasmon-enhanced photocatalysis systems are in a similar form with the nanocomposites that contain Au metal and TiO_2 semiconductor. The material combinations have strengthened the photocatalysis by improving the charge generation and separation.[80] To comprehend the functionality of plasmonic photocatalyst, the properties of both the plasmonic Au NPs and the supporting TiO_2 should be taken into consideration.

2.3.1 Structures and photoelectronical properties of TiO_2 materials

The crystalline structures of TiO_2 are mainly divided into three phases: anatase, rutile and bookite. The anatase phase has been proven to be the most stable phase with two low energy surfaces, (101) and (001), as shown in Figure 2.5(a) and (c), respectively. The (101) surface is the most prevalent face for anantase nanocrystals, and is corrugated with 5-coordinate Ti atoms and bridging oxygen in alternating row at the edges. The (001) surface is rather flat but can undergo a (1×4) reconstruction. The (100) surface is not a typical nanocrystal that can be observed during the hydrothermal growth of rod-like anatase. Its surface has 5-coordinate Ti atoms in double rows alternating with double rows of bridging oxygens, undergoing a (1×2) reconstruction as shown in Figure 2.5(b).[95,96]

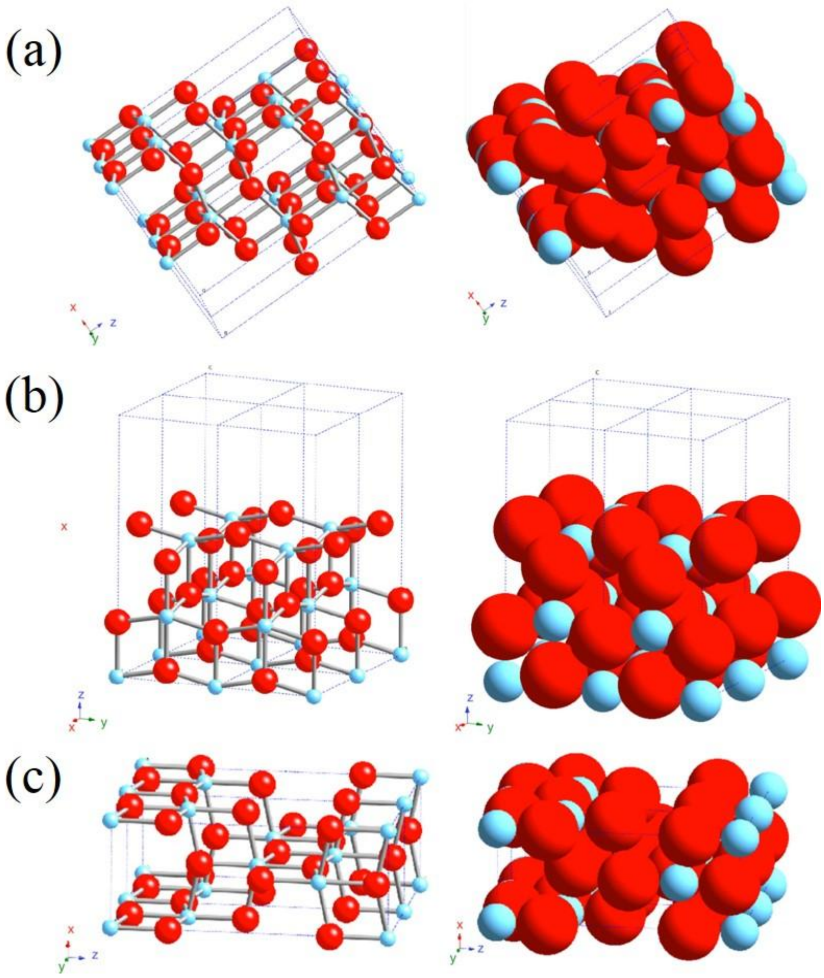

Figure 2.5 Schematic diagrams of three most prevalent anatase crystals with low-index faces: (a) (101); (b) (100); and (c) (001).[95]

Although the photoelectrochemistry field of semiconductors is introduced by researchers to a large extent, the potential for practical applications still seems very limited due to the susceptibility to photocorrosion. The work of Fujishima' group showed that TiO_2 is much less susceptible and is thus suitable for the applications such as solar energy conversion.

The photoelectrochemistry of TiO_2 is summarized in Figure 2.6. It indicates that the conductive band energy (E_{CB}) of rutile is essentially consistent with the reversible hydrogen potential ($E_{H+/H2}$) at all pH conditions. The E_{CB} level of anatase is more negative by 0.20V than the hydrogen production level, which implies sufficient ability for H_2 production. At lower pH values, the E_{CB} value of rutile is also coincident with the reversible potential for O_2 reduction to superoxide radical anion $HO_2\cdot$, which is then coupled to form H_2O_2 and O_2. But at a higher pH, E_{CB} continues to become more negative, while the potential for O_2 reduction to superoxide radical anion $O_2\cdot^-$ remains constant at about -0.284V. This implies that this process should become more favorable in alkaline pH region for rutile. For anatase, the E_{CB} level is sufficiently negative to reduce O_2 to $O_2\cdot^-$ over a wide pH range, which is coincident with its higher photocatalytic activity.

For both anatase and rutile, the valence band energies E_{VB} is positive enough to oxidize water into O_2 at all pH values. The E_{VB} for both materials lies at the same potential approximately, which is positive enough to produce free ·OH radicals (lower pH) or $O\cdot^-$ radicals (higher pH). However, it is only positive enough to oxidize 2-propanol to its radical cation (2-propanol$\cdot^+$) in the acidic pH region. The photoelectrochemical oxidation of organic compounds has been studied extensively. For example, Villareal et al. employed the polycrystalline anatase electrodes as a model system for photocatalysis, as a result, the direct hole-mediated oxidation and ·OH radical-mediated oxidation are distinguished successfully.[97] The result turns out that it is oxidized via an ·OH radical for methanol adsorbed less strongly, while it is oxidized directly for formic adsorbed more strongly.

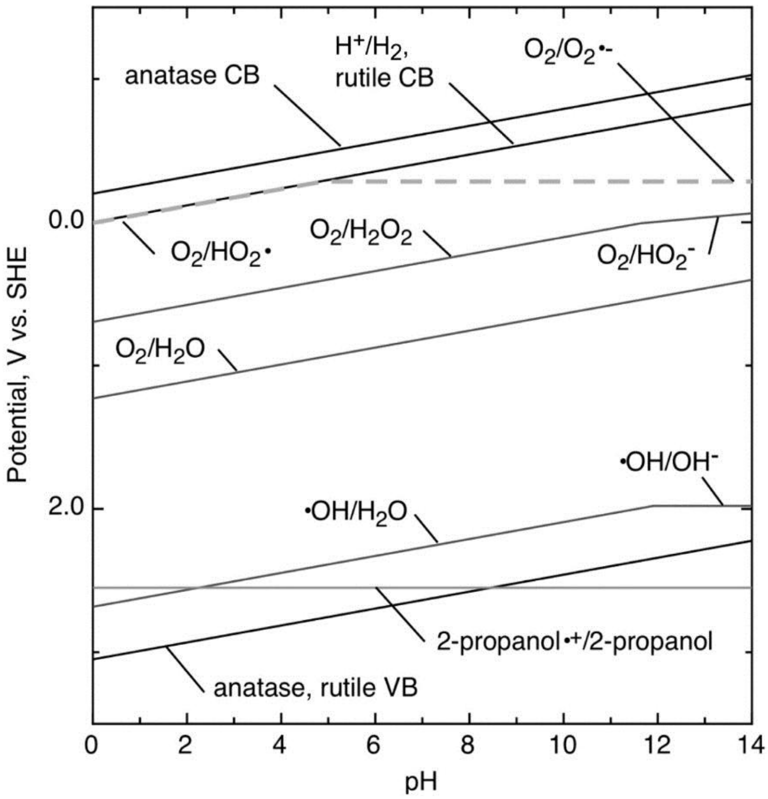

Figure 2.6 Energy bands of TiO_2 as a function of pH.[95]

2.3.2 Optical properties of Au NPs

The LSPR refers to the phenomenon that the conducting electrons of the noble-metal NPs experience a collective oscillation induced by the electromagnetic field of the incident light. If the frequency of the incident light is coincident with the resonance frequency of the noble-mental NPs, the LSPR will take place simultaneously with the correlative light absorption (also including light scattering).[80,86] Meanwhile, the oscillating charges increase the electrical field near the surface, and also benefit the LSPR of the Au NPs.

The LSPR features of noble-metal NPs (i.e. Ag, Au, Pt) contribute greatly to their strong ability of light absorption, which can be adjusted by changing their size, shape and/or surroundings. Moreover, noble-metal NPs can act as an electron trap as well as the active reaction sites. These factors give a novel path for effective visible-light-responsive photocatalysts. In other words, the combination of the noble-metal NPs and a suitable polar semiconductor forms a metal-semiconductor composite photocatalyst. In this way, the LSPR provides a light absorption by inducing electron excitation in a broad wavelength range including visible, infrared (IR) and near IR regions. The photo-generated electrons and holes are then separated efficiently in the interface of the metal NPs and semiconductor. The LSPR is a key feature to determine the property and performance of nanoscale optical and photonics devices.[98] For solar-to-hydrogen energy conversion applications, however, studies have been limited mostly to the gold and silver for the following reasons. First, they have tunable plasmon resonances at UV and visible-light frequencies. Secondly, they have relative large (often 10 times) optical cross sections than their geometric cross section. Thirdly, gold typically has high thermodynamical and/or kinetical stability under harsh conditions (pH, potential, et al.).[80,84]

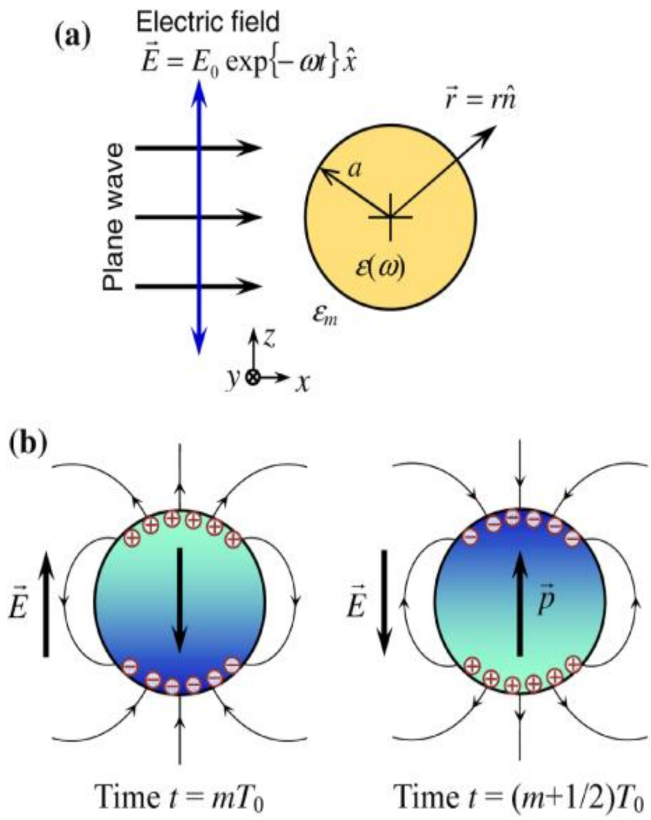

Figure 2.7 Schematic description of the optical response of a particle in the spherical shape. (a) Graph of a homogeneous nanosphere under the illumination of a plane incident light; (b) the homogeneous nanosphere is polarized by the external electric field and the oscillating dipole enhances the local electric field and radiates energy in turn. The scattering is ignored.[48]

The noble-metal NPs with various shapes, typically including spherical, triangular, nanoshell, prism-like, etc. each has its own plasmonic features.[99,100] The nanospere has the simplest shape, providing a strict analytical solution in an symmetric electromagnetic field. Moreover, many features of the nanosphere, for example, the enhanced local electric field and dipole behaviour, are maintained in the NPs with different shapes.

Theoretically, the interaction between the NPs and the incident light can be analyzed by solving the Maxell equations with proper boundary conditions. That is, a strict description of the electrodynamic response can deduced by the Mie theory. When the NPs has the size $a << \lambda$, the quasi-static approximation is applied, which is valid for NPs with the size up to about 100 nm. The phase change over the nanoparticle's volume is negligible, which simplifies the spatial distribution of the electric field. Figure 2.7 (a) shows an electrostatic field response to the incident light in a particle. Once the electric field distributions are determined, the harmonic time can be introduced as a dependent variable to the solution. When a homogeneous spherical nanoparticle is illuminated by a plane-wave light, it will be encompassed by a homogenous, non-absorbing, infinitely large nonmagnetic medium with a dielectric constant ε_{m} (see Figure 2.7 (a)). Conceptually, the external electric field displaces the conduction electrons of the nanosphere to form a negative charge center on one end and a positive charge center on the other end. Consequently, a dipole is formed as shown in Figure 2.7 (b). Its LSPR feature can be determined from the dipolar mode and is described by the following polarizabilityα,

$$\alpha = \frac{3\alpha_0 V(\varepsilon - \varepsilon_m)}{\varepsilon + 2\varepsilon_m}, \tag{2.12}$$

where α_0 is the vacuum permittivity, V is the volume of the nanoparticle, ε_m is the dielectric constant of the surrounding medium. Additionally, $\varepsilon(\omega) = \varepsilon_r(\omega) + i\varepsilon_i(\omega)$, depending on $\varepsilon_r(\omega)$ and $\varepsilon_i(\omega)$ as the real and imaginary parts, respectively. At the electromagnetic frequency ω, a strong resonance of SPR occurs for $\varepsilon_r(\omega) = 2\varepsilon_m$. For $\varepsilon_r(\omega)$, it depends on many factors such as the metal's character, the electric property of the surrounding medium, and the size and shape of the metal NPs, which also provide the approaches to tune the optical properties of the metal NPs.

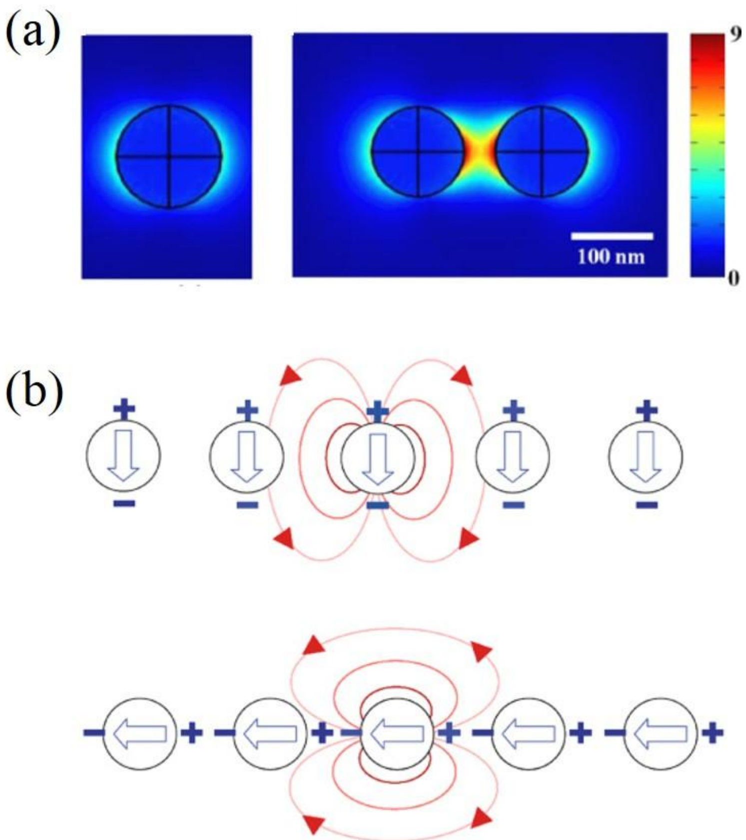

Figure 2.8 (a) Comparison of the electric field distributions between a single Au nanoparticle and nanoparticle dimer. (b) Schematic of the transverse and longitudinal resonant modes for near-field dipolar coupling of NPs.[48]

The above discussion focuses on the study of individual spherical NPs. For materials in practical plasmonic photocatalysis, the NPs may exist in a random distribution, therefore, the neighboring NPs may cause significant plasmonic coupling effect.[101,102] According to the magnitude of the interparticle distance *d*, the plasmonic coupling could be divided into two types—near-field dipolar coupling and far-field diffraction coupling. Since the latter is important just for 1D and 2D arrays of NPs, it could be ignored in this study.[103]

The electric field distributions of a single Au nanoparticle with diameter around 100 nm and an Au nanoparticle dimer spaced by ~30 nm are compared in Figure 2.8 (a). For the single nanoparticle, a surface region within 10 nm is distributed with the enhanced electric field, while for the dimer, the whole space between the two Au NPs is covered. Additionally, the enhancement factor $|\boldsymbol{E}|$ for the single nanoparticle and the dimer is about 4 and 9, respectively. Apparently, a larger electric field region and a higher enhancement factor will activate more photocatalysts and enhance the reactivity of plasmonic photocatalysis to a large extent. Therefore, a dimer is more advantageous for the plasmonic photocatalysis. Figure 2.8 (b) illustrates the mechanism of the near-field coupling with a chain of NPs. The polarization perpendicular to the chain axis will excite the transverse mode. The resonant oscillation increases the restoring dipole force of every particle since the charge distribution of the nearby particles tends to repel the dipole. Consequently, the resonant wavelength is blue-shifted as compared to that of a single nanoparticle. Inversely, the longitudinal mode will reduce the restoring force since the dipole is attracted by the surface charges of the neighboring particles. As a result, the longitudinal resonance shifts red. Based on these reasons, the absorption of the coupled NPs present split peaks. Moreover, due to the plasmonic coupling, the areas near the surface of single nanoparticle emerge enhanced electric field. From the view point of the photocatalysis, the feature of two absorption peaks further enhances the absorption and is beneficial to the photocatalysis,

2.3.3 Influence factors of Au NPs-based SPR phenome

The LSPR associated electric polarization can enhance the light absorption of the metal NPs as a result of the enhanced local electric field. When the Fermi level of the noble metal lies between the valence band maximum (VBM) and conduction band minimum (CBM) of a polar semiconductor, the deposition of the noble-metal NPs on the polar semiconductors forms a plasmonic photocatalyst. This hybrid is most likely charge-polarized and easy to trap light. Proper conditioning towards the structures of these noble-metal NPs can concentrate and fold light into the semiconductor layer, enhancing the absorption and exciting more electrons at the interface between metal NPs and the dielectric material. Au NPs can appear in different kinds of color, such as red, blue, or others, depending on their size, shape, and surroundings, which reflects the LSPR upon the illumination light with proper wavelengths.[48]

(a) Influence of the shape and size of NPs

Besides the spherical shape, the NPs in plasmonic photocatalysis can also exist in many other forms, including triangular, spheroid, nanorods, nanoshells and even irregular shapes, which own different absorption features. Many fabrication processes do not produce NPs with identical shape. Anisotropic metal NPs will provide an access to unique optical phenomena that are from those of spherical NPs. Some studies are reported to control the shape and size on purpose.

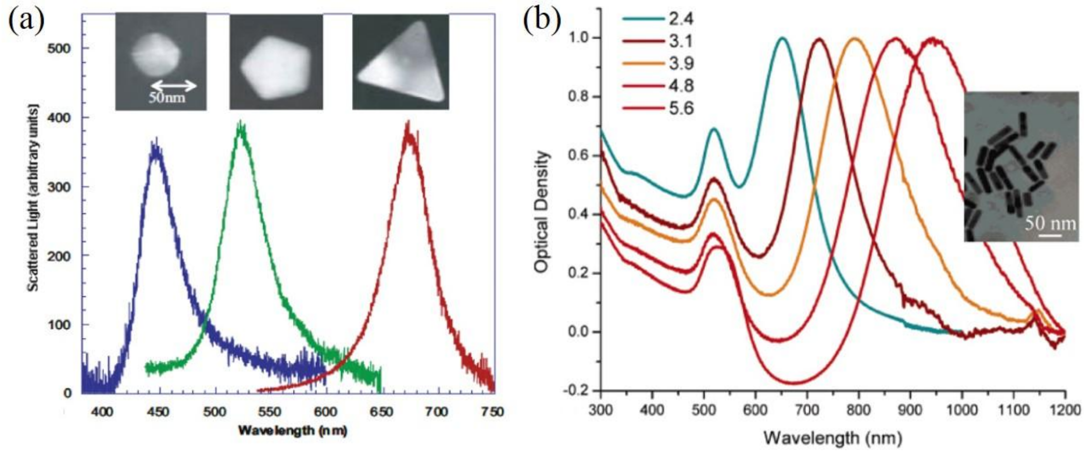

Figure 2.9 (a) Scattering spectra of single silver NPs with various shapes.[104] (b) Absorption spectra of Au nanorod with changed aspect ratios. Every curve appears two separate peaks corresponding to the transverse and longitudinal resonances.[105]

The scattering spectra of silver NPs with various shapes are investigated in Figure 2.9 (a), which illustrate the influence of the shape. When the shape of the NPs is changed from the spherical to pentagonal and then triangular, their corresponding resonant wavelength is shifted from 445 to 520 nm, and then 670 nm.[104] Besides, multiple resonance peaks appear in metal NPs with other shapes because of the multipolar resonance in different directions. For instance, one of the most striking features in the UV-vis-NIR absorption spectrum for the Au nanorods is the emergence of multiple plasmon bands. For the NPs in rod shape, the two resonances along both of the short axis and the long axis endow a higher LSPR wavelength than that of Au NPs in spherical shape. With the increase of the length-to-width ratio of the rod, the wavelength position of the long axis SPR shifts from the visible to the near-infrared region, increasing the oscillator strength progressively as shown in Figure 2.9 (b).[106] Moreover, the aspect ratio of the Au nanorods strongly influence the energy of the longitudinal plasmon. That is to say, the multiple plasmon of the nanorod with the different sizes exhibit different absorption features.

(b) Influence of the local environment

The LSPR status can also be tuned by the local environment. Since the noble-metal NPs are often fabricated on the surface of the photocatalyst, it is important to understand the influence of their interaction with the substrate on plasmon resonance properties. The noble-metal NPs (e.g. Au nanospheres) can be contact with the photocatalysts (e.g. TiO_2) in various situations. The shift of the resonant wavelength are diagramed in Figure 2.10 (a) by employing a silver nanosphere (radius 10 nm) embedded into a mica shell (10 nm thick) gradually. They could only have the surface contact, or the metal NPs could be surrounded by the photocatalyst completely or partially. Corresponding to the increased contact area, the peak of the resonant wavelength shifts from 350 to 430 nm.

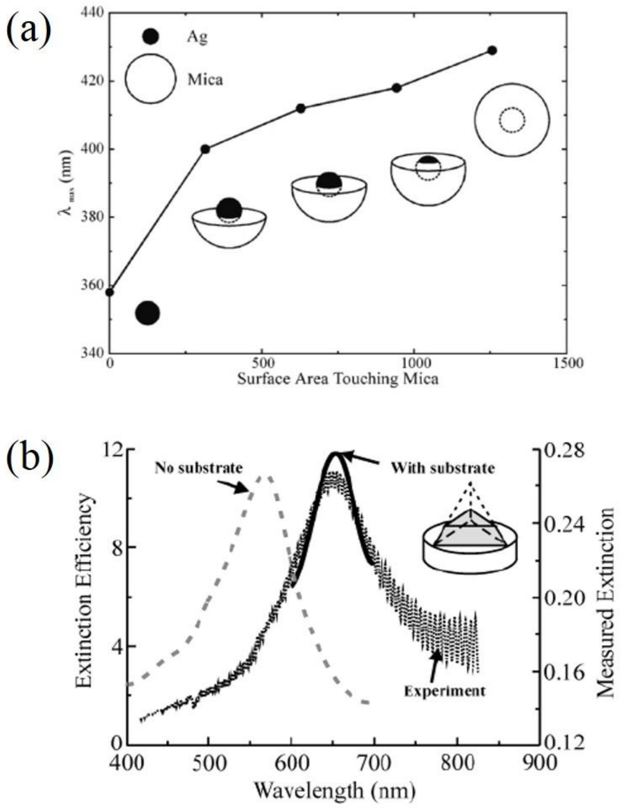

Figure 2.10 (a) the resonant wavelength shifts with the embedment state of the silver nanosphere (radius 10 nm) into the mica shell. (b) Comparison between the discrete dipole approximation (DDA) and experimental results for the effect on the extinction of a truncated tetrahedron.[88]

Figure 2.10 (b) demonstrates how the substrate influences the resonance wavelength of truncated tetrahedral particles by comparing the discrete dipole approximation (DDA) and experimental result. The DDA calculations include the results both with and without a mica slab attached to a truncated tetrahedron. The extinction peak with the presence of the substrate slab is shifted by about 120 nm to the red, in consistent with the measured value. The refraction index effect of the substrate on the plasmon wavelength of the truncated tetrahedral particles further indicates that the substrate-induced spectral shift is linear with the refractive index of the substrate slab. A similar phenomenon will occur when the Au NPs are embedded into TiO_2 thin films or particles since the LSPR of Au NPs varies with the embedded states, which is beneficial to plasmonic photocatalysis as well. Typically, various embedding states may exist simultaneously when the noble-metal NPs are mixed with the photocatalyst. Thus the absorption spectral range can be broadened significantly by tuning the surrounding condition, which will yield a better utilization of the broadband light source.[88]

2.3.4 Systematic naming of plasmonic photocatalysts

For the plasmonic photocatalysis, the noble metals usually exist in the shape of NPs; the semiconductor photocatalyst turns out to be a particle or thin film. The particle and the thin film possess their own advantages, the former reveals a large specific surface area and the latter has good electron transport ability, both are favorable for various photocatalytic applications. In this thesis, the noble metal is Au, which exist in forms of both NPs and film, while the semiconductor photocatalyst investigated is TiO_2 films fabricated by the atomic layer deposition (ALD) or the sol-gel method. Herein, the naming of plasmonic photocatalysts aims to reveal the substantial structure characters of photocatalysts and differentiate them simply and conveniently. A series of simple naming rules for these photocatalysts is feasible. Therefore, we propose the following rules in this thesis:

- The noble-metal NPs (Au) deposited on the surface of the semiconductor film (TiO_2) is denoted by **Au NPs/TiO_2**. Au may be embedded into TiO_2 partially but the majority part of its surface is exposed to the surroundings. The symbol '/' represents the surface contact between the Au NPs and TiO_2. It also corresponds to many other material systems in this form.
- The noble-metal NPs (Au) fully covered by semiconductor film(TiO_2) is denoted as **TiO_2-Au NPs**. The '-' represents a flat thin film surface. Therefore, Au NPs are surrounded by the TiO_2 and no exposure to the surroundings.
- The noble-metal film (Au) fully covered by semiconductor film (TiO_2) is denoted as **TiO_2-Au**. The '-' represents a flat thin film surface. Therefore, Au film is surrounded by the TiO_2 film and has no exposure to the surroundings.

These symbols are often used in Chapter 4 and 5, which help represent different materials and contact forms.

2.4 Understanding of the plasmonic enhanced photocatalysis

2.4.1 Plasmonic enhancements in the primary steps of photocatalysis

A typical photocatalysis process mainly consists of four steps as shown in Figure 2.11. Briefly, the incident photos are first absorbed and then induces a local electric field. Afterwards, active charge carriers are generated and then separated. During the whole photocatalysis steps, the LSPR contributes to their enhancements to different extents.[48]

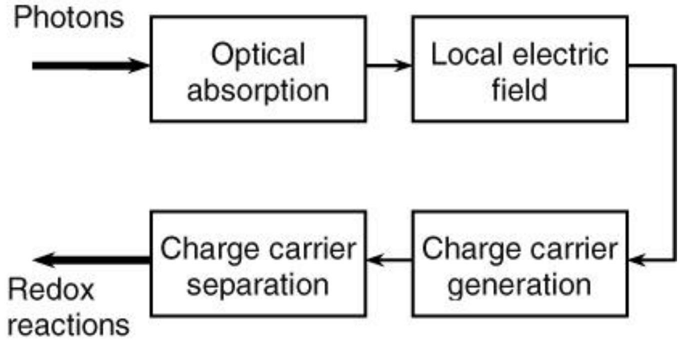

Figure 2.11 Plasmonic enhancements for the primary steps of photocatalysis.[48]

The optical absorption may be enhanced in two ways: the LSPR and multiple-scattering. For the former, the LSPR-enhanced photon absorption is very common. The principle and influence factors of the plasmon-induced optical absorption has been explained in section 2.3.3, respectively. For the latter, the increase of photon path length attributes to the metal NPs' scattering at the surface of the semiconductor, thus enhancing the optical absorption, as shown in Figure 2.12. Usually, the photons can penetrate into the semiconductor photocatalysts by a few nanometers to a few micrometers, but only a portion of photons is used efficiently. Thus, photons that are absorbed deep into the body of the semiconductor contribute little to the photoreaction since those photogenerated charge carriers have to go through such a long diffusion distance that they will probably recombine before reaching the surface. The scattering allows these plasmonic NPs acting as mirrors to increase the travel path of photons within the semiconductor photocatalysts and the adjacent surface of these plasmonic metal. As a result, more photons can be utilized to generate the electron-hole pairs. The size of the plasmonic metal is another significant factor that affects the absorption and scattering properties. Large metal NPs will scatter the unabsorbed photons near the surface of the semiconductor, which can increase the average photon path length. For noble-metal NPs in small size (typically< 60 nm), the absorption is dominant as compared to the scattering. However, for the NPs in large size (typically > 100 nm), the scattering comes into effect and creates a long path for the photons. The scattering also highly relies on the density of the metal NPs. Multiple scattering with too low loading is negligible, whereas metal NPs with high loading absorb majority of photons, leaving few to the multiple scattering.

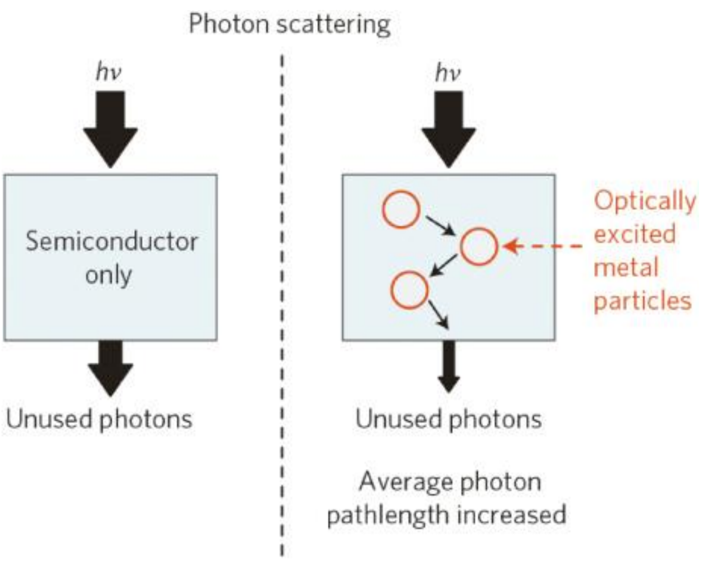

Figure 2.12 Scattering effect of the metal NPs leads to an absorption enhancement through increasing the average photon path length in the metal/semiconductor composite.

The absorbed photons permeate into the space-charge region between the semiconductor and the noble-metal NPs, which will arouse immediate enhanced local electric field for the single mental NP and/or coupled metal NPs. For both of the single metal NP and the coupled metal NPs, the enhanced electric field have been explained in section 2.3.2.

The local electric field with higher intensity will assist the generation and transfer of electrons and holes, which will be explained in detail in the following section 2.4.2 In addition, the Schottky junction reduces the recombination chance drastically and increases the lifetime of photo-excited charge carriers significantly. As a result, the charge carrier separation is enhanced. A prerequisite of this vital effect is the direct electrical contact of the metal NPs with the semiconductor. Without the direct electric contact, the metal in the sole or isolated form cannot contribute to the separation of the photo-excited electrons and holes in the photocatalytic systems. Besides, other factors must also be taken into consideration, especially the type of semiconductor (n- or p-type), the Femi level position of the semiconductor relative to the work function of the metal (or to the electrochemical potential level when it is exposed to the electrolyte).[48,92]

2.4.2 Mechanism of charge carrier generation in plasmonic photocatalysis

Compared to the traditional approaches such as doping, the integration of plasmonic materials can extend the absorption of semiconductors with large bandgap to a wider range more efficiently, since the traditional approaches may bring in many defects to decrease the separation efficiency of electrons and holes. Many Au-based plasmonic photocatalysts reveal enhanced photocatalytic activity relative to the bare supporting semiconductor photocatalyst, which probably results from the LSPR of Au NPs. There are two primary mechanisms have been identified to explain how the collective plasmon resonance is established in a metal nanoparticle within the nanocomposite electrode in this thesis: (1) plasmon-induced resonance energy transfer (PRET), an intense oscillating electric field around the metal; (2) hot-electron injection from the metal to the semiconductor.[107,108,109]

(a) Plasmon resonance energy transfer (PRET)

The PRET explains photocatalysis enhancement via the flow of electromagnetic energy around the metal NPs. It can be regarded as energy transfer from the plasmon to the absorber (usually semiconductors) through the electromagnetic field or the interaction between the dipoles. The electromagnetic field induced by the LSPR will be created in the neighboring of these plasmonic metals (regards as near-field), whose intensity is several orders of magnitude stronger than that of the triggering photons. Hence, the plasmonic metals can be regarded as an amplifier of the near-field electromagnetic resonance through the plasmon-resonance transfer.

The spatial distribution of plasmonically excited electrons and holes by PRET depends on the electric field intensity, just as in ordinary photoexcitation. The intensity of the localized electromagnetic field is influenced by the spatial distance from the semiconductor's surface to the center of the plasmonic metal nanoparticle, as well as the size of the plasmonic metal. When the resonating electrons establish an oscillating electric field E, the associated intensity is proportional to E^2 and decays from the nanoparticle as

$1/d^6$ at large distances (d is the distance from the center of the nanoparticle). At shorter distances, where the curved surface of the plasmonic nanoparticle can be approximately regards as a flat surface, the decay of the electric field intensity is $1/s^4$ (s is the distance from the surface of the nanoparticle). As a result, both the photons and plasmons are polarized in specific directions, which lead to significant variation in the electric field intensity. The Figure 2.13(a) illustrates the electric field intensity for an incident electromagnetic wave near a plasmonic metal nanoparticle in which a dipolar resonance is established. The arrows represent Poynting vectors, i.e., the energy flux of incident light, showing that the metal NPs absorb photons from an area much larger than their geometric cross section. When two plasmonic metal NPs move close to each other, the electromagnetic field intensity is enhanced dramatically due to the coupling of their localized electromagnetic field.

The rate of optical energy absorption by a semiconductor is proportional to the electric field intensity. The PRET effect is to enhance the electric field intensity in a small, well-defined location of semiconductor, thereby increasing the power absorbed in this region. For a semiconductor with a short minority carrier transport distance, localizing the dissipation of electromagnetic energy at the semiconductor-water interface provides a way to minimize the average distance that holes must travel to reach the electrolyte. For semiconductors that are limited by majority carrier transport, localizing light absorption near the semiconductor-substrate interface mitigates this limitation.

(b) Hot-electron transfer injection

For the PRET effect, the enhancement can be observed at wavelengths where the plasmon resonance and semiconductor resonance overlap. For hot electron transfer injection, it provides an alternative way to enhance the photocatalysis well below the semiconductor bandgap. This is a distinctive characteristic of hot-electron transfer. If a plasmon is neither emitted as a photon (scattered) nor undergoes the PRET, it will be absorbed by the metal NPs to excite hot electrons. The hot-electron inject effect is also known as the LSPR-sensitization effect, which can inject hot electrons directly to the conduction band (CB) of the nearby semiconductor, as shown in Figure 2.13. The hot-electron injection occurs only at the place where the plasmonic metal NPs are in direct contact with the semiconductor photocatalysts, since a Schottky barrier can be formed since the work function of the plasmonic material is often higher than that of an n-type semiconductor or lower than that of a p-type semiconductor.

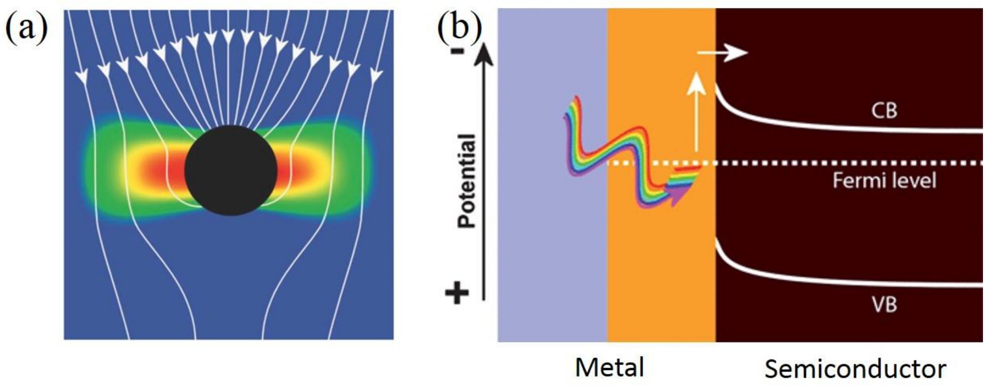

Figure 2.13 (a) The illustration of the energy flux (Poynting vectors) and the electric field intensity for an incident electromagnetic wave with an electric field in the plane of image; (b) hot electron injection from a metal into an n-type semiconductor.[108]

From the above discussion, it can be inferred that the amount of the excited hot electrons with energy higher than the Schottky barrier determines the injection efficiency of the hot-electron injection process. Both of the semiconductor photocatalysts and the plasmonic materials determine the energy barrier. The shape, size, the essence of the plasmonic metals, and the electron chemical properties of the vicinal photocatalysts influence the hot-electron injection process corporately. It is found that the holes generated by gold and copper are hotter than the electrons by 1-2 eV, whereas electrons and holes from silver and aluminum have equitably distributed energies. It demonstrates that the energy distributions of plasmonic hot carriers are sensitive to the electronic band structure of the metal. The electron chemical property of the semiconductor is another significant factors. Particularly, plasmonic metals would also function as electron traps, which experience a reverse process to the hot-electron injection. When the LSPR is negligible as compared to the electron-hole generation in the semiconductor, the electrons will transfer from the semiconductor to the plasmonic metals. For example, Au NPs on TiO_2 show lower dissociation activity than those on SiO_2, thus the hot-electrons are transferred into the TiO_2 matrix, resulting in a decreased amount of electrons for the H_2 dissociation. Many strategies have been introduced to enhance the hot-electron-injection effect, including the optimization of calcination conditions and the control of morphology. Adjusting the interface between the plasmonic metals and semiconductor photocatalysts could reinforce the hot-electron-injection process and reduce the possible recombination rate of charge carriers.

2.5 Visible-light absorbers for photothermal applications

In addition to the semiconductors with narrow bandgap, the above explanation has demonstrated that the shape and size of noble metal NPs offers the handle for tuning the light absorption without changing the particle volume. That is, the nanostructure geometries offer plasmon resonance tunability with high plasmon sensitivity. As mentioned in Section 2.3, the TiO_2 containing various Au NPs can enhance the absorption and photocatalytic activity under the visible-light illumination. Recently, there has been much progress in the development of plasmonic NPs for photothermal therapy applications due to its LSPR properties as well as their inherently low toxicities. When the conductive electrons are excited to induce surface plasmon oscillations, non-radiative relaxation occurs through electron-phonon and phonon-phonon interactions, generating efficiently localized heat that can be transferred to the surrounding environment. Since the absorption band of the noble metal NPs is tunable by altering the shape or size of NPs, designing photothermal absorbing agents in the NIR region is possible. A wide variety of Au nanostructures, including aggregates of colloidal particles, nanoshells, nanocages, nanorods and hollow nanospheres, have large surface plasmon absorption in the NIR region, which may be effective for photothermal therapy.[110,111] For example, the LSPR peak position of Au nanocages can be precisely tuned to any desired wavelength in the range of 600-1200 nm; hollow gold nanospheres combine small size, spherical shape, and strong, narrow and tunable SPR, and satisfy the requirement for photothermal ablation therapy.[112] Although the NPs are good candidates for photocatalysis and photothermal therapy due to the ability to control the absorption peak at the required wavelength accurately, but the relatively narrow absorption band, the low stability, the low duration and the complexity of procedures limit their practical use.

2.6 Rough Au film as broadband plasmonic absorber

Efficient absorption of visible light by nanostructured metal surfaces open new exciting perspectives within broadband plasmonic absorbers. So far, significant effort has been paid to optimize LSPR absorbers with broadband absorption within visible range, for instance by optimizing structural geometries and by using gain materials. Previously, Liu et al. fabricate a perfect plasmonic absorber with polarization-independent absorbance. This plasmonic device yields ~ 99% absorbance and remains highly absorption over a wide range of incident angles.[113] Similarly, Moreau and his colleagues create a metamaterial absorber by randomly adsorbing chemically synthesized silver nanocubes onto a nanoscale-thick polymer spacer layer on a gold film.[114] This film-coupled nanocubes provide an absorption spectrum that can be tailored by varying the geometry (the size of the cubes and/or the thickness of the spacer). Besides, Thomas et al. realized non-resonant light absorption via a well-defined geometry of ultra-sharp convex metal grooves.[115] The two-dimensional arrays of sharp convex grooves in gold ensure efficient (> 87%) broadband (450-850 nm) absorption of incident light, reaching an average level of 96%. Hedayati et al. design, fabricate and character a perfect plasmonic absorber in a stack of metal and nanocomposite, showing almost 100% absorbance spanning a broad range of frequencies from ultraviolet to the near-infrared, which proposes an outstanding candidate for broadband absorber.[116] Recently, Liu et al. theoretically propose and experimentally demonstrate a unique broadband plasmonic metamaterial absorber by utilizing a sub-10 nm meta-surface film structure to replace the precisely designed metamaterial crystal in the common metal-dielectric-metal absorbers. The average value of absorbance across the whole spectral range of 370-880 nm reaches 83%.[117]

However, up to date, all of the above mentioned methods that probably achieve broadband visible absorption, including perforated metallic films, grating structured systems and metamaterials turn out to be complex to fabricate, costly and/or with a relative narrow spectral range of absorption. The work in this thesis employs a rough Au film in conduct with a TiO_2 film to realize the broadband absorption for photocatalysis in the UV and visible ranges. This rough Au film as broadband plasmonic absorber is quite simple, cost-effective for large-scale fabrication, which makes it an excellent candidate for advanced high-efficiency absorber materials.

Table 2-1 The property comparison between the four approaches to adjust photoresponse, including the rough Au film connect with TiO_2 film (Rough Au film/TiO_2 film), Au NPs for photothermal, the Au NPs connect with TiO_2 film (Au NPs/TiO_2) and semiconductors with narrowband (Narrow−band semiconductors)

	Narrow-band semiconductors	**Au NPs/TiO_2**	**Au NPs for Photothermal**	**Rough Au film/TiO_2 film**
Absorption band	Vis, narrow	Vis, narrow	NIR, narrow	UV+Vis+NIR, broad
Energy transfer	Photo-generated carriers	Plasmonic electrons	Plasmonic thermal	Plasmonic electrons
Stability	Unstable	Stable	Unstable	Stable
Toxicity	Yes	No	No	No
Fabrication difficulty	Low	Moderate	High	Low

Moreover, compared to the traditional narrow-band semiconductor, the composite Au NPs/TiO_2, the Au NPs for photothermal, the new design and fabrication is superior to the previous approaches in many aspects, which is listed in the Table 2-1. Apparently, the novel structure of rough Au film/TiO_2 film endows a wide absorption range, from UV, to Vis and NIR region. Based on the energy transfer in the form of plasmonic electrons, it can also make more efficient utilization of the incident light. Additionally, the rough Au film/TiO_2 film structure is stable, non-toxicity and easy to be fabricated, all of which are preponderant for the photocatalysis.

2.7 Summary

In summary, plasmonic photocatalysis enables to utilize visible light to improve the efficiency of water purification and water splitting, exhibiting unique such as strong visible absorption, multi-scattering enhanced photon-semiconductor interaction, improved charge separation by Schottky barrier and many others. Although a number of studies have been reported for plasmonic photocatalysis, there are still many limitations such as low stability, narrow absorption band and so on. Therefore, it is necessary to develop new plasmonic photocatalysts to overcome the existing problems and to fulfil the great potential for real applications

CHAPTER 3

FABRICATION, CHARACTERIZATION AND CALCULATIONS

This chapter will present the fabrication method, the measurement setups and the simulation tools to be used in the next chapters. During my PhD study, two types of TiO_2 preparation methods, sol-gel deposition and atomic laser deposition (ALD), are involved and developed. Both the Au film and the Au NPs are obtained by the sputtering with sputtering deposition method. The simulation is conducted by using the finite-difference time-domain (FDTD) method. Their optical properties are characterized to give transmission spectrum, absorption spectrum and reflection spectrum. Their morphologies and structure properties are analyzed using the scanning electron microscopy (SEM), the atomic force microscopy (AFM) and the X-ray diffractometry (XRD), respectively. Their electrochemical properties are characterized using an electrochemical working station. The details of them are presented in this Chapter.

3.1 Fabrication of photocatalytic devices

3.1.1 Fabrication of TiO_2 film

The quality of the TiO_2 film is a significant factor for plasmonic photocatalysis, herein we have adopted two types of fabrication methods, sol-gel deposition and ALD deposition, to obtain TiO_2 films in the present study. The TiO_2 films of the sol-gel method is thicker than that of the ALD deposition.

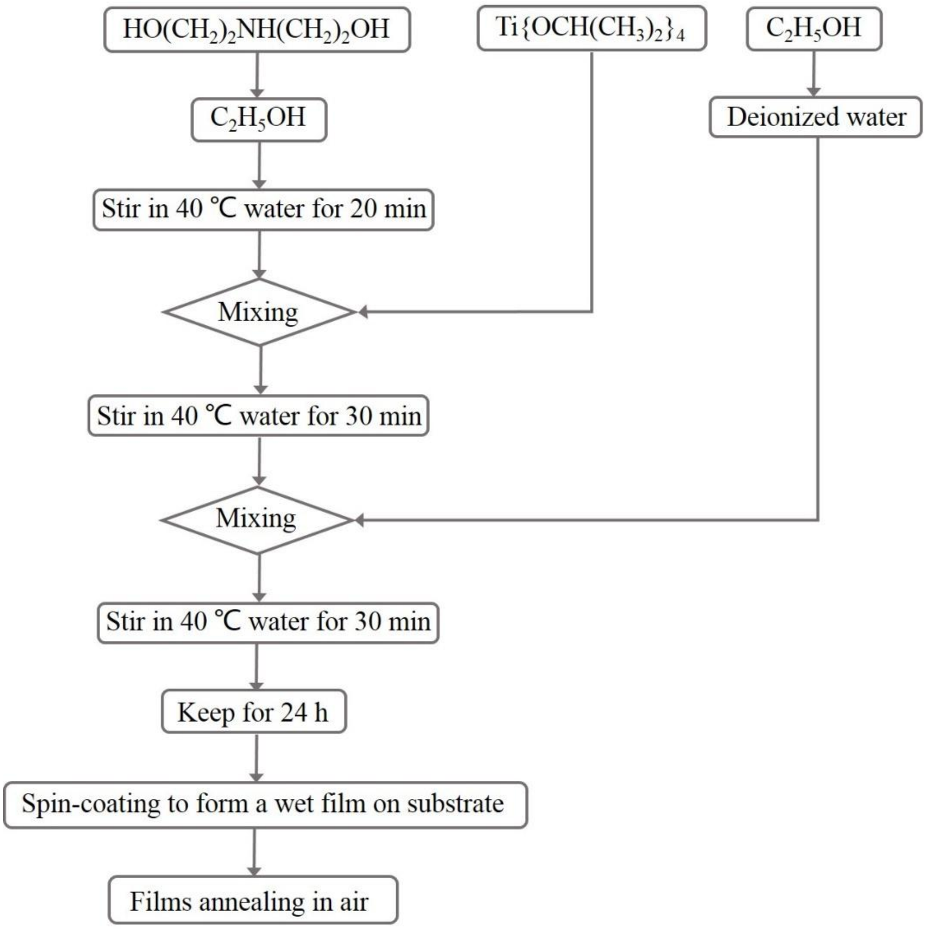

Figure 3.1 Scheme of the overall synthesis process developed to TiO_2 sol-gel thin films.

The preparation process of the sol-gel deposition method is depicted in Figure 3.1, which starts with the preparation of TiO_2 sol-gel. Titanium isopropoxide (TIP) $Ti[OCH(CH_3)_2]_4$ with purity 98% is introduced as the source of titanium and 2.5-ml diethanolamine $\{HO(CH_2)\}_2NH$ is dissolved in 70-ml ethanol (CH_3CH_2OH) with the purity of 99.7%. The mixture is sealed and stirred at 40 °C for 20 min with a magnetic stirrer. After adding the precursor of 9-ml TIP is added into the water-free mixture, the stirring process is continued for another 20 min. When a slightly yellow and transparent gel is formed, 20-ml water and 1-ml ethanol are added into the gel and stirred for another 20 min. The obtained solution is kept at ambient temperature for 24 h. After the sol-gel is ready, it is spin-coated onto the Au layer with a spinning speed of 2000 rpm for 30 s. The obtained TiO_2 layer is sintered at 500 ^oC in air for 1 h to get the anatase phase.

Figure 3.2 Digital image of the ALD system (Cambridge NanoTech, G2 Savannah).

The ALD is also carried out to prepare TiO_2 using a commercial system (Cambridge NanoTech, G2 Savannah) as shown in Figure 3.2. The ALD procedure involves an alternating exposure of Tetrakis dinethylamido titanium (TDMAT), $Ti(NMe_2)_4$ and deionized water vapor as the precursor carriers at a process temperature of 100 °C with N_2, and then the purge gas at a pressure of 90 sccm. Both the pulse time and the purge time for the precursors are 2 s. The deposition rate of TiO_2 is estimated to be 0.55 Å per cycle. The thickness of TiO_2 film is tuned by controlling the deposition time. After the ALD deposition, the TiO_2 films are annealed at 500 °C for 1 h. To study the influence of TiO_2 thickness, TiO_2 films with a series of thicknesses (i.e., 5, 10, 20, 30 and 50 nm) can be obtained by controlling the deposition time.

3.1.2 Fabrication of Au film and Au NPs

Deposition of rough Au film on the FTO glass is performed in a magnetron sputtering system that is equipped with three cathodes in a pure Ar atmosphere at 6×10^{-3} Pa. Before deposition, the FTO glass with a size of $10 \times 10 \times 2$ mm^3 is rinsed successively with acetone and methanol in an ultrasonic bath for 10 min, and then dried with a pure nitrogen flow. The separation distance between the target and the substrate is maintained at 10 cm throughout the deposition, while the substrate speed is set at 6 rpm. For the formation of rough Au films, a thin Cr film is first deposited on the FTO as an adhesion layer.

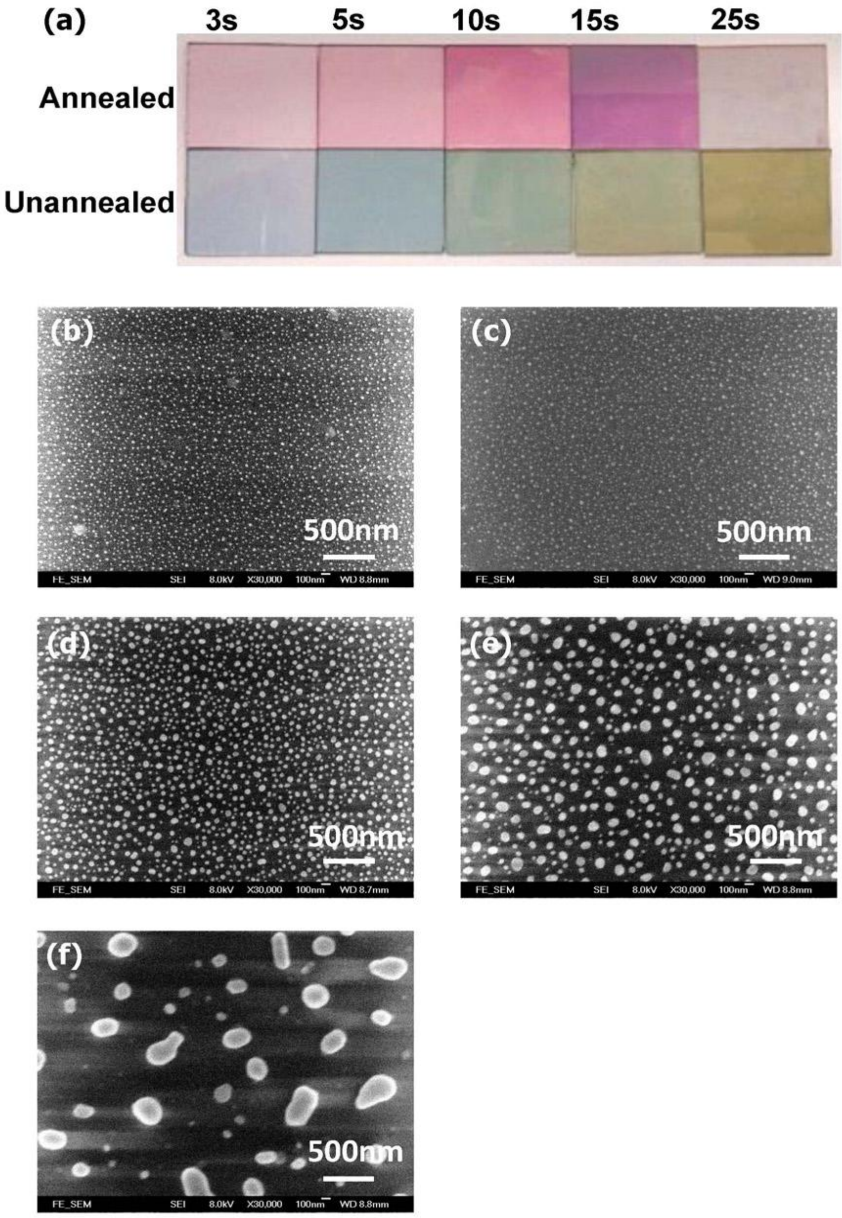

Figure 3.3 (a) Photographs of the Au films with the sputtering time of 3 s, 5 s, 10 s, 15 s and 25 s, before and after annealing at 500 ^{o}C; SEM images of the Au nanoparticles after annealing the Au films with the sputtering time of (b) 3 s; (c) 5 s; (d) 10 s; (e) 15s and (f) 25 s. Before annealing, the colors of the Au films are deep. After annealing, the films turn to lighter color and are mostly pink. For the sizes of Au nanoparticles, they increase with longer deposition time.

The Au NPs with random distribution are fabricated by using the sputtering and the thermal annealing. Herein, a thin Au layer is first deposited by magnetron sputtering. After being annealed at 500 °C for 1 h, the thin Au layer is transformed into Au NPs during the annealing-cooling process.[118] The obtained Au NPs are mostly spherical but with random sizes. The Au layers deposited with different sputtering times (and thus different thicknesses, in the range of 3 – 25 nm) result in the Au NPs of different sizes, as shown in Figure 3.3.

3.2 Characterization

3.2.1 Transmission, reflection and absorption spectra measurement

The optical reflection and transmission spectra of the films are all recorded over a wavelength range of 400 – 800 nm using a UV-Vis spectrophotometer (Shimadzu, UV-2550) as shown in Figure 3.4(a). Transmission spectrum gives the transmitted percentage of the incident light as a function of wavelength. Reflection measurements are performed with an integrating sphere that uses a $BaSO_4$ plate as the reference as shown in Figure 3.4(b). This means that both the direct reflected light and the diffuse scattering light are included in the reflection measurement. In this PhD research, all the absorption spectra of these samples are determined from $A = 1 - R - T$, where A, R and T are the normalized absorption, reflection and transmission, respectively.

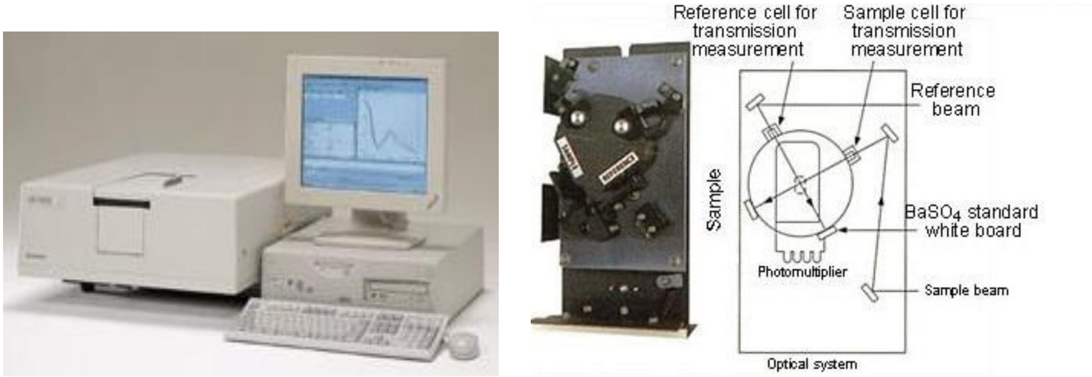

Figure 3.4 (a) Photograph of the UV-Vis spectrophotometer equipment and (b) the attachment ISR-240A integrating sphere.

3.2.2 X-ray diffraction (XRD) measurement

The XRD results of the samples are measured by a Rigaku automated multipurpose Smartlab X-ray diffractometer (Rigaku Corp., Tokyu, Japan) in order to determine the crystal structure. The digital image of the equipment is shown in Figure 3.5.

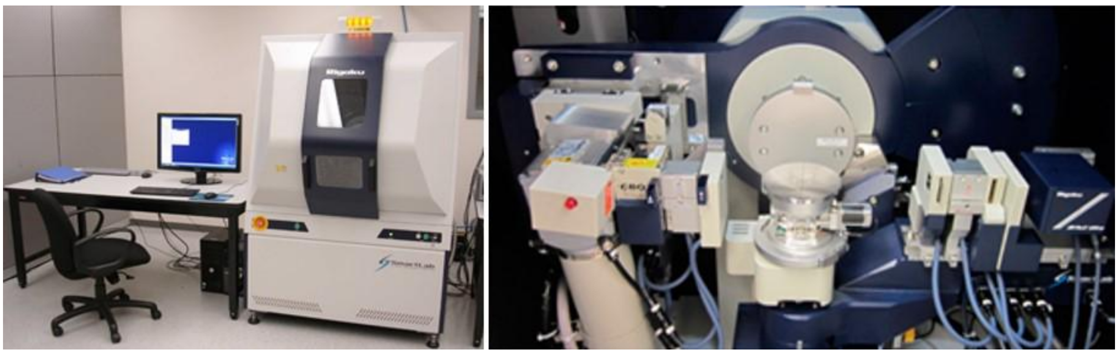

Figure 3.5 Digital image of the Smartlab X-ray diffractometer.

3.2.3 Scanning electron microscopy (SEM) measurement

The layer structures of the sample in this thesis are investigated with a JEOL Model JSM-6490 SEM equipped with an energy dispersive X-ray spectroscopy detector. Gold is coated on the TiO_2 sample surface in advance to produce clear images. The SEM technique uses a high-energy electron beam to generate various signals at the surface of solid specimens. These accelerated electrons carry significant amounts of kinetic energy, which is dissipated into a variety of signals via electron-sample interactions, including backscattered electrons (BSE), secondary electrons, photons (characteristic X-rays for elemental analysis and continuum X-rays), diffracted backscattered electrons (EBSD to determine crystal structures and orientations of minerals), visible light (cathodoluminescence, CL), and heat. The secondary electrons and the BSE are used most commonly to image samples. SEM analysis is considered to be “non-destructive”; that is, X-rays generated by electron interactions do not bring volume loss of the sample. Hence it is possible to analyze the same materials repeatedly.

3.2.4 Atomic force microscopy (AFM) measurement

The AFM provides a 3D image of the surface in a nanoscale, which is popular for the surface analysis of materials. It mainly has three measurement modes, including contact mode, tapping mode and non-contact mode. Among them, tapping mode is most common. During the tapping-mode scanning, the tip approaches the surface, taps on the sample surface slightly, and contacts the surface with the bottom of its swing. This mode can overcome many problems associated with friction, adhesion and so on. The AFM images of Au film presented in this thesis is carried out using a Bruker Nanoscope 8 atomic force microscope.

3.3 Photoelectrochemical methods for the visible-light photoactivity

When the photocatalytic material is immobilized onto an electrically conducting supporting substrate, it can be used as an electrode in a photoelectrochemical cell to measure its properties including the flat band potential, the bandgap energy, the kinetics of electron and hole transfers, et al. When the potential-current response is examined with potentiometric analysis, taking an n-type semiconductor TiO_2 for example, no significant anodic (positive) current is observed in the dark since there are no essential holes in the valence band. When incident light with energy equal to or greater than the bandgap energy, electrons are excited to the conduction band, leaving positive holes in the valence band. At potentials more positive than the flat band potential E_{fb}, an increased anodic current can be observed. The photocurrent (J_{ph}) is the difference between the current observed in the irradiation and in the dark, indicating the transfer rate of electrons and/or hole at the interface of the working electrode and the electrolyte. At the flat band potential, no net current is observed because of the electron-hole recombination. The situation of a p-type semiconductor under the irradiation is reversed, that is, an increased cathode current is observed at potentials more negative than E_{fb}. If the electrode is irradiated by a polychromatic source (e.g. xenon) along with a series of monochromators, the spectral photocurrent response can be measured. The incident photon to current conversion efficiency (IPCE) can be determined according to the following formula,

$$\mathrm{IPCE}(\%) = \frac{1240 \times I_{sc}}{\lambda \times P_{light}} \times 100 \tag{3.1}$$

where λ is the wavelength of the incident light, P_{light} is the illumination power density at the specific wavelength and I_{sc} is the measured density of short circuit photocurrent at the specific wavelength. For an n-type semiconductor, this is the quantum efficiency for holes transferring to the electrolyte. The maximum wavelength at which photocurrent can be observed is related to the bandgap energy of the material. Therefore, the visible light activity can be determined simply by using a desired emission light to excite the electrode while the current is monitored as a function of applied potential.[52]

The photocatalytic reaction and the IPCE action spectra are measured with an electrochemical workstation (CH Instruments, CHI 660E) in a standard three-electrode configuration. To obtain the IPCE action spectra, band-pass filters with a bandwidth less than 15 nm full-width at half-maximum (FWHM) are used. The photocatalytic films (such as the TiO_2-Au bilayer, the TiO_2-AuNP hybrid and the bare TiO_2 film) are used as the working electrode. A Pt wire electrode is used as the counter electrode and a saturated calomel electrode (SCE) as the reference electrode. Besides, KOH aqueous solution (1 M) is commonly used as the electrolyte. The working electrode is illuminated over an area of about 1 cm^2 under a simulated solar source (AM 1.5G, 300 mW/cm^2) with a UV-cutoff filter to obtain visible light with $\lambda \geq 400$ nm.

3.4 Theoretical calculations

The finite-difference time-domain (FDTD) method is the simplest full-wave techniques, both conceptually and practically, to solve problems in electromagnetics.[119,120] The FDTD method can fit into the category of resonance region techniques, in which the characteristic dimensions of the domain are on the order of a wavelength in size. When the size of the object is very small as compared to the wavelength, quasi-static approximations can provide more effective solutions. Generally, the FDTD method introduces finite differences as approximations to both the spatial and temporal derivatives that appear in Maxwell's equations (specifically Ampere's and Faraday's laws). The Taylor series expansions of the function $f(x)$ expanded about the point x_0 with an offset of ±δ/2, the central-difference approximation is given by

$$\left.\frac{df(x)}{dx}\right|_{x=x_0} \approx \frac{f\left(x_0+\frac{\delta}{2}\right)-f\left(x_0-\frac{\delta}{2}\right)}{\delta}, \tag{3.2}$$

which provides an approximation of the derivative of the function at x_0.[121] The change in the E-field in time (the time derivative) is dependent on the change in the H-field across space (the curl). The electric and magnetic fields are determined at every point in space within the computational domain. Figure 3.6 illustrates a standard cartesian Yee cell using FDTD, where E and H field vector components are distributed.

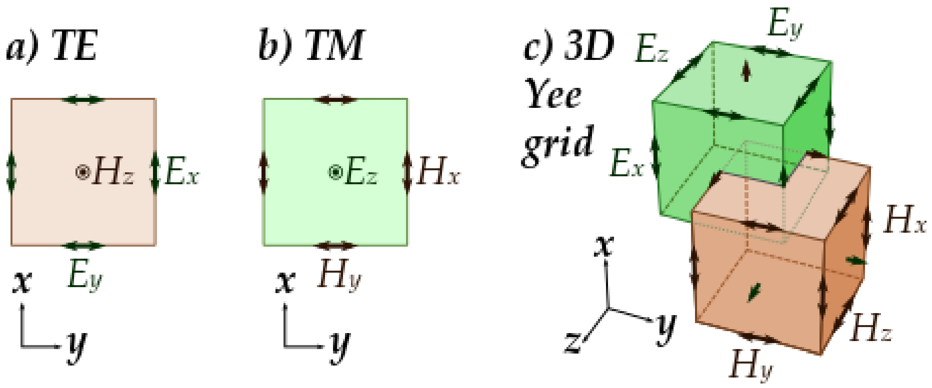

Figure 3.6 Illustration of a standard Cartesian Yee cell used FDTD, which electric and magnetic field vector components are distributed, from Wikipedia.

A commercial FDTD software (Lumerical FDTD Solutions) is implemented to conduct all the optical simulations. A 3D simulation model is built up according to the physical structure, the material, and the fabrication process of the actual samples.

3.5 Summary

This chapter describes the fabrication methods, the measurement setups and approaches and the simulation tools that will be used in the following two chapters, and provides the methodologies for the sample preparations, the performance characterizations and the numerical analyses in this Ph.D. study.

CHAPTER 4

PLASMONIC BROADBAND VISIBLE-LIGHT ABSORBERS BASED ON ROUGH AU FILMS

This chapter present a TiO_2-Au bilayer presents a TiO_2-Au bilayer that consists of a rough Au film under a TiO_2 film, which aims to enhance the photocurrent of TiO_2 over the whole visible region and may be the first attempt to use rough Au films to sensitize TiO_2. It is the first absorber that has developed in this PhD study. Experiments show that the bilayer structure gives the optimal optical and photoelectrochemical performance when the TiO_2 layer is 30 nm thick, measuring the absorption 80% – 90% over 400–800 nm and the photocurrent intensity of 15 $\mu A \cdot cm^{-2}$, much better than those of the TiO_2-AuNP hybrid (i.e., Au nanoparticle covered by the TiO_2 film) and the bare TiO_2 film. The superior properties of the TiO_2-Au bilayer can be attributed to the plasmonic resonance of the rough Au film as the hot electron generator and the photoactive TiO_2 film as the electron accepter. As the Au film is fully covered by the TiO_2 film, the TiO_2-Au bilayer avoids the photocorrosion and leakage of Au materials and is expected to be stable for long-term operation, making it an excellent photoelectrode for photocatalysis applications.

4.1 Introduction

TiO_2 has been extensively investigated as a photoelectrode for various applications, including photoelectrochemical water splitting,[122,108] pollutant degradation,[123,124] et al., thanks to its excellent chemical stability, photocorrosion resistance and low cost. As an n-type semiconductor with a wide band gap around 3.2 eV, it can only absorb UV light (cutoff wavelength ~ 388 nm), causing a low utilization efficiency of solar light that spans from UV to infrared region. Therefore, an ideal photoelectrode for the solar photocatalysis should have a broadband absorption in the wavelength range of 400 – 800 nm. For practical applications, the photoelectrode should be stable, low cost and easy to fabricate large area samples. In the past decade, plasmonic metal nanoparticles (NPs) have been widely used to sensitize the host semiconductor TiO_2 to visible light [48,125]. However, most studies rely on the metal NPs with uniform shape and size to obtain visible light response, whose absorption due to the localized surface plasmon resonance (LSPR) is often limited to a narrow spectral range.[126,127] Since the broad absorption band can be regarded as a combination of many absorption peaks, Au NPs with different sizes and/or shapes may be used, but it is not favorable due to the fabrication complexity. Additionally, multiple resonant peaks could also be obtained by use of the multipolar resonances in different directions,[128,129] but the processing techniques appear to be complicated.[130–132] To address this problem, broadband resonant nanostructures with simple fabrication are highly desired.

Here we present the design, fabrication, and characterization of a broadband plasmonic absorber for solar energy harvesting and photocatalysis application in the visible region. This absorber, the TiO_2-Au bilayer, consists of two simple layers, a rough Au film at the bottom as the plasmonic antenna to absorb optical energy to generate hot electrons and a TiO_2 film at the top as the photocatalyst to receive the hot electrons for the photoactivity below the bandgap. The sputtering technique is adopted to fabricate the rough Au film, which is equivalent to a collection of random Au nanostructures with different geometries and sizes. Consequentially, this TiO_2-Au bilayer supports the plasmon resonances and the accompanied plasmonic coupling effect, and enables the broadband absorption in the visible wavelength range from 400 to 800 nm, acting effectively as a broadband visible-light absorber. This kind of visible-light absorbers have been used in photothermal systems that rely on the heat but not the electron generation and transfer[129,133]. Their great potential for the photocurrent generation has been merely overlooked. The photoelectrochemical performance of the TiO_2-Au bilayer demonstrates apparent enhancement as compared to the TiO_2-AuNP hybrid (i.e., Au NPs covered by TiO_2 film) and the bare TiO_2 film, indicating superior ability of electron generation and transfer. We further examine the influence of the thickness of TiO_2 film on the properties of the TiO_2-Au bilayer, and find that the optimal thickness is 30 nm. The fabrication techniques of the TiO_2-Au bilayer are relatively simple and cost-effective. Additionally, in contrast to the previously reported AuNP-TiO_2 systems (i.e., Au NPs on top of the TiO_2 film)[134,135,136], the TiO_2-Au bilayer buries the Au film under TiO_2 film that protects the Au film from the photocorrosion and leakage during the photochemical reactions, making it promising for long-term operations.

4.2 Experimental section

4.2.1 Device fabrication

A 100 nm-thick Au film and Au NPs are deposited by the sputtering method as described in Section 3.1.2 , respectively. The Au film is about 150 nm. A thin Au layer is deposited onto TiO_2 film for about 10 s, and then transformed into Au NPs during the annealing-cooling process, as shown in Figure 3.3(a) and (d).[118] The obtained Au NPs are mostly spherical but with random sizes, resulting in the Au NPs of different sizes. Among various preparation methods of Au NPs, this physical sputtering method is simple, low cost, and easy to fabricate diverse composite films with uniformly distributed metal particles.[137,138]

The TiO_2 film is deposited onto three different substrates, including the Au film, the Au NPs and the FTO glass slide, respectively, using a commercial atomic laser deposition (ALD) reactor (Cambridge NanoTech, G2 Savannah). Correspondingly, three types of samples, the TiO_2-Au bilayer, the TiO_2-AuNP hybrid and the bare TiO_2 film, are obtained as shown in Figure 4.1. The fabrication procedures of the ALD process is elaborated in section 3.1.1. To study the influence of TiO_2 thickness, TiO_2 films with a series of thicknesses (i.e., 5, 10, 20, 30 and 50 nm) are deposited on the 30-nm-thick Au film to obtain five samples of the TiO_2-Au bilayer.

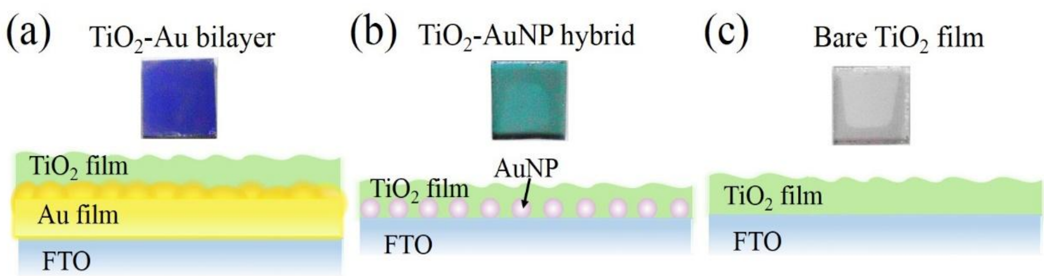

Figure 4.1 Photographs and schematic diagrams of the three samples, from left to right, (a) the TiO_2-Au bilayer, (b) the TiO_2-AuNP hybrid and (c) the bare TiO_2 film, each sample has the footprint of 1 cm × 1 cm.

4.2.2 Characterization of Bilayer Structures

The characterization methods are elaborated in section 3.2.2-3.2.4. The morphology and the particle size of the samples, including the Au film, the Au NPs and the TiO_2 film, are observed by SEM. The surface morphology and the height information of the Au film are also obtained by the AFM. The XRD pattern is recorded using a X-ray diffractometer. The TiO_2 films with different thicknesses on the Au film are recorded using the Cu K_α radiation and the scanning speed of 5°/min with the 2θ range from 10 to 80°.

4.2.3 Optical and photoelectrochemical measurements

Based on the optical spectral measurement methods in section 3.2.1., the optical reflection and transmission spectra of the TiO_2-Au bilayer, the TiO_2-AuNP hybrid and the bare TiO_2 film are recorded over a wavelength range of 400 – 800 nm using a UV-Vis spectrophotometer. The photocatalytic reaction and the IPCE action spectra are measured with an electrochemical workstation (CH Instruments, CHI 660E) in a standard three-electrode configuration as discussed in section 3.3.4. The TiO_2-Au bilayer, the TiO_2-AuNP hybrid and the bare TiO_2 film are used as the working electrode, respectively.

4.2.4 Simulation

Based on the discussions in section 3.4, a 3D simulation model is build up according to the physical structure, the material, and the fabrication process of the actual samples. The refractive indices of Au are simulated using the built-in data of FDTD Solution software. The category labeled as CRC is chosen, which provides the model by fitting the experimental data in CRC Handbook of Chemistry & Physics. The refractive indices of TiO_2 are simulated with the dispersion formula as $n^2 = 5.913 + 0.2441/(\lambda^2 - 0.0803)^2$. The wavelength is denoted as λ in the dispersion formula with the unit of micron.

4.3 Results and Discussion

4.3.1 Comparison of TiO_2-Au bilayer, TiO_2-AuNP hybrid and bare TiO_2 film.

Figure 4.1 shows the photos and the schematic diagrams of the proposed structures, including the TiO_2-Au bilayer, the TiO_2-AuNP hybrid and the bare TiO_2 film. For the bare Au film deposited on the FTO glass, it appears dark yellow. After this bare Au film is covered by the 30-nm TiO_2 film to form the TiO_2-Au bilayer, it turns to dark blue after the annealing treatment (see the Figure 4.1(a)). The characteristic color of Au NPs is pinkish, which turns into light blue after the coverage of the 30-nm-thick TiO_2 film to form the TiO_2-AuNP hybrid (see the Figure 4.1(b)). The bare TiO_2 film exhibits a light gray color (see the Figure 4.1(c)). It is noted that the edge parts of samples have slightly different colors from the central parts, because the central parts have TiO_2 deposited only on one side, whereas the edge parts are covered on both sides due to some process details. One-sided TiO_2 deposition is favorable for optical spectrum measurements as compared to two-sided TiO_2 deposition since the latter may result in a non-uniform film on the back side. In experiments, only the central parts with a diameter of 1 mm is used to investigate the photoelectrochemical properties.[139]

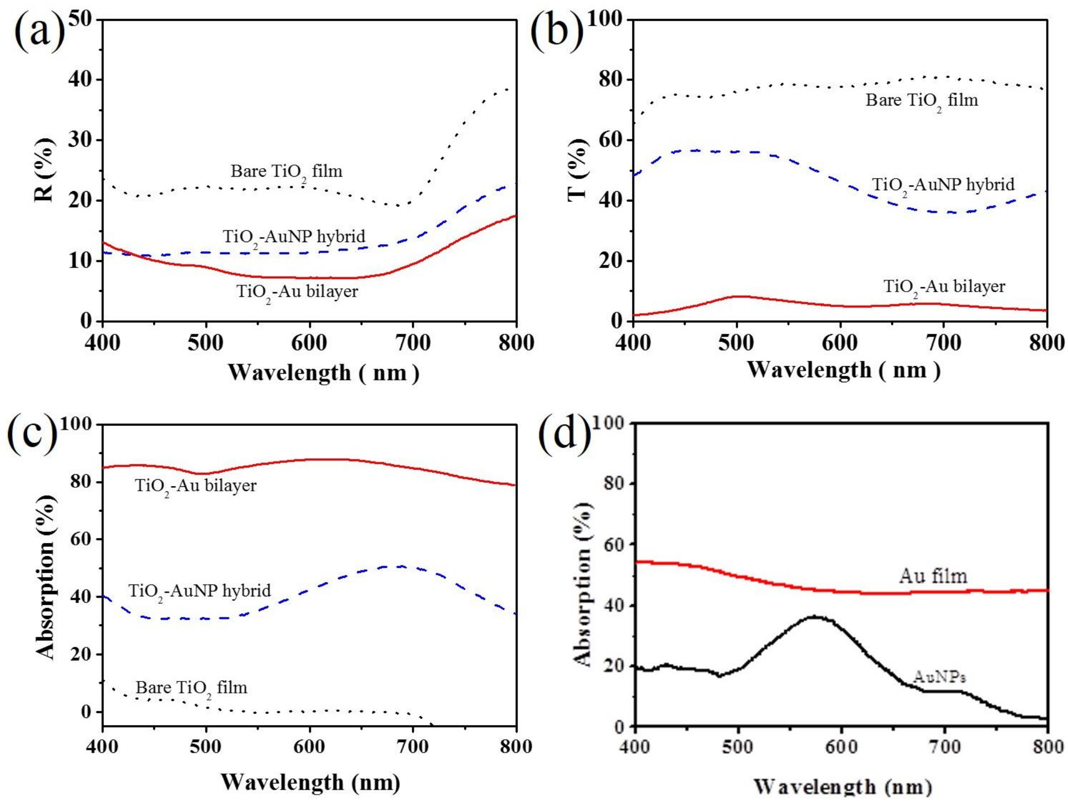

Figure 4.2 (a) Reflection spectra, (b) transmission spectra and (c) absorption spectra of the bare TiO_2 film (black dashed lines), the TiO_2-AuNP hybrid (blue dotted lines) and the TiO_2-Au bilayer (red solid lines), respectively; and (d) absorption spectra of the rough Au film itself and the bare Au NPs. It is noted that the ranges of *y* axis are different, i.e., 0 – 50% in (a), 0 – 100% in (b), 0 – 100% in (c), and 0 – 100% in (d). Here the reflection measurements are performed with an integrating sphere that uses a $BaSO_4$ plate as the reference. This means that both the direct reflected light and the diffuse scattering light are included in the reflection measurement.

A key step to improving the photocurrent is to increase the optical absorption in visible range. Figure 4.2 compares the absorption spectra of the TiO_2-Au bilayer, the TiO_2-AuNP hybrid and the bare TiO_2 film. Here the absorption A is calculated by the equation $A = 1 - R - T$, where R and T are the normalized reflection and transmission, respectively, as shown in Figure 4.2(a) and 4.2(b). The bare TiO_2 film shows high reflection and transmission over 400 – 800 nm, resulting in very weak absorption (see Figure 4.2(c)). The TiO_2-AuNP hybrid shows obvious enhancement of absorption, especially near 680 nm, which can be attributed to the LSPR effect of the Au NPs. In contrast, the TiO_2-Au bilayer exhibits much stronger absorption. Particularly, the absorption spectrum is flat over the whole range of 400 – 800 nm, with the minimum absorption of 80% and the maximum 90%. The absorption spectra of the bare Au film and the Au NPs are presented in Figure 4.2(d)). For the Au NPs, its absorption spectrum shows an apparent peak at around 580 nm. When the Au NPs are covered by the TiO_2 film, the absorption peak of the TiO_2-AuNP hybrid is shifted to a longer wavelength (at ~ 700 nm, see Figure 4.2(c)). For the rough Au film that consists of Au clusters with different shapes and sizes, the absorption peaks are overlapped to form a broad absorption spectrum.

The light-harvesting capability plays an important role in the enhanced photoelectrochemical activity under the visible light irradiation. The photoactivities of these three TiO_2-based samples are evaluated using the *I-t* technique. Figure 4.1 plots the curves of photocurrent density at the 0-V bias potential. The transient photocurrent responses of the three TiO_2-based samples are measured for several on-off cycles of irradiation. The rise and fall of the photocurrent respond well to the switching on and off of the visible-light irradiation (wavelength > 400 nm). The photocurrent drops to zero as soon as the irradiation is turned off, and recovers immediately when the irradiation is turned on again. It indicates that the current is completely due to the visible-light response of the photoelectrode, and the charge transport is very fast. As can be read from Figure 4.13(c), the TiO_2-Au bilayer produces the transient photocurrent density of 12.4 $\mu A\cdot cm^-$

^{2}, higher than the TiO_2-AuNP hybrid (3.2 μA·cm^{-2}) and the bare TiO_2 film (1.5 μA·cm^{-2}) by a factor of 3.8 and 8.2. This suggests that the TiO_2-Au bilayer has the best effect on charge generation, separation and transport[140]. In addition, the order of the photocurrent densities agrees with the absorption measurements in Figure 4.2(c), that is, TiO_2-Au bilayer > TiO_2-AuNP hybrid > bare TiO_2 film.

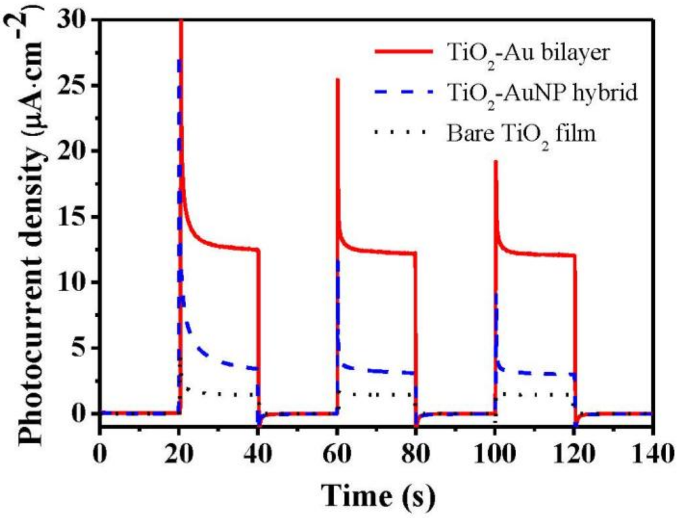

Figure 4.3 The absorption spectra and (b) *I-t* plots of the TiO_2-Au bilayer (red solid lines), the TiO_2-AuNP hybrid (blue dashed lines) and the bare TiO_2 film (black dotted lines), respectively. The TiO_2 films of the three samples are all 30 nm thick. The potential for the *I-t* measurement is 0 V vs SCE (saturated calomel electrode).

As a supplement, the *I-t* plots of the TiO_2-AuNP hybrid and the bare TiO_2 film are tested as plotted in Figure 4.4. Figure 4.4 (a) is the calibrated emission spectrum of the light source after the UV-cutoff filter (> 400 nm), the overall intensity is ~ 300 mW/cm^2 at the photoelectrode surface.[141] When the narrow-band optical filters are used to get monochromatic light for the measurement of action spectrum, the calibrated optical intensities of the light source at different wavelengths are plotted in Figure 4.4(b).

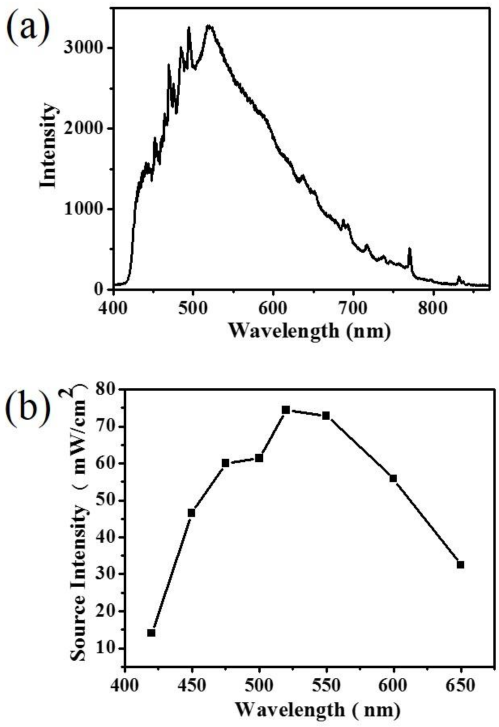

Figure 4.4 (a) Calibrated emission spectrum of the light source after the UV-cutoff filter (> 400 nm), the overall intensity is ~ 300 mW/cm^2 at the photoelectrode surface. (b) Calibrated optical intensities of the light source at different wavelengths when the narrow-band optical filters are used to get monochromatic light for the measurement of action spectrum.

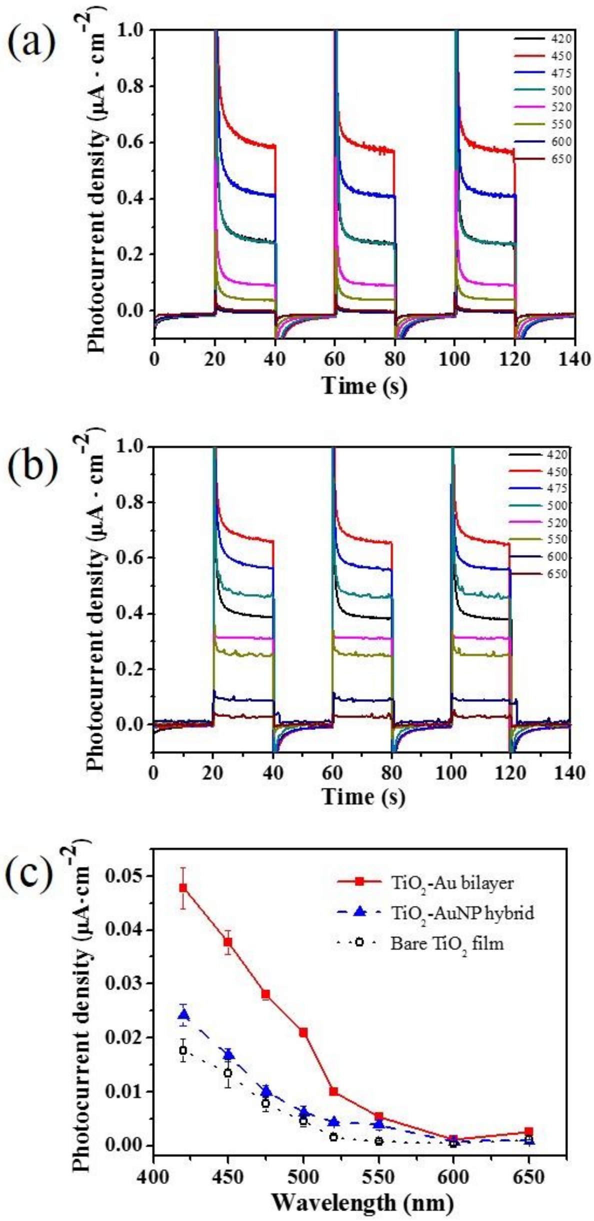

Figure 4.5 *I-t* plots of (a) the bare TiO_2 film and (b) the TiO_2-AuNP hybrid under monochromatic lights of 420, 450, 475, 500, 520, 550, 600 and 650 nm, respectively. (c) Action spectra (i.e., photocurrent versus light wavelength) of the TiO_2-Au bilayer (red solid line), the TiO_2-AuNP hybrid (blue dashed line) and the bare TiO_2 film (black dotted line). In these three samples, the TiO_2 layers are all 30 nm thick.

Under monochromatic lights at the wavelengths of 420, 450, 475, 500, 520, 550, 600 and 650 nm, respectively, *I-t* plots of the bare TiO_2 film and the TiO_2-AuNP hybrid are shown in Figure 4.5(a) and (b), respectively. The action spectra (i.e., photocurrent density versus light wavelength) are plotted in Figure 4.5(c) for the three samples for quantitative comparison. It is seen that the TiO_2-Au bilayer has the highest response under every monochromatic light illumination, showing significant enhancement by a factor of about 2 as compared to the TiO_2-AuNP hybrid and the bare TiO_2 film.

For the TiO_2-Au bilayer and the TiO_2-AuNP hybrid, their differences in the *I-t* plot and the action spectrum can be explained below. From the physical mechanisms, the enhancement of photocurrent in the TiO_2-Au bilayer and the TiO_2-AuNP hybrid should be attributed to the Au nanostructures and the formation of Schottky junctions at the interfaces of Au and TiO_2. The former enables the optical absorption to visible light, whereas the latter improves the separation of photo-generated electron-hole pairs and suppresses the recombination of photogenerated charge. But there are still some differences between the TiO_2-Au bilayer and the TiO_2-AuNP hybrid, lying mostly in the density of Au nanostructures. In the TiO_2-Au bilayer, the rough Au film can be regarded as an assembly of densely-packed random Au nanostructures (e.g., NPs, nanocavities) with different shapes and sizes (see detailed discussion below). The dense packing results in a large number of Au nanostructures, and the LSPR effect of every single Au nanostructure sums up to high absorption over a wide span of wavelength; moreover, the dense packing enables the plasmonic coupling of neighboring Au nanostructures and further enhances the optical absorption. In addition, the dense packing provides good electrical connections among the Au nanostructures for the transport and distribution of photogenerated charges. Furthermore, the rough Au film provides large interface area between the Au and TiO_2 for the Schottky junction and enables the efficient transfer of photo-excited electrons and holes between Au to TiO_2. In comparison, the TiO_2-AuNP hybrid has relatively low density of Au NPs, causing not that ideal absorption and charge transfer. As a result, the TiO_2-Au bilayer has stronger absorption than the TiO_2-AuNP hybrid and is expected to have larger photocurrent.

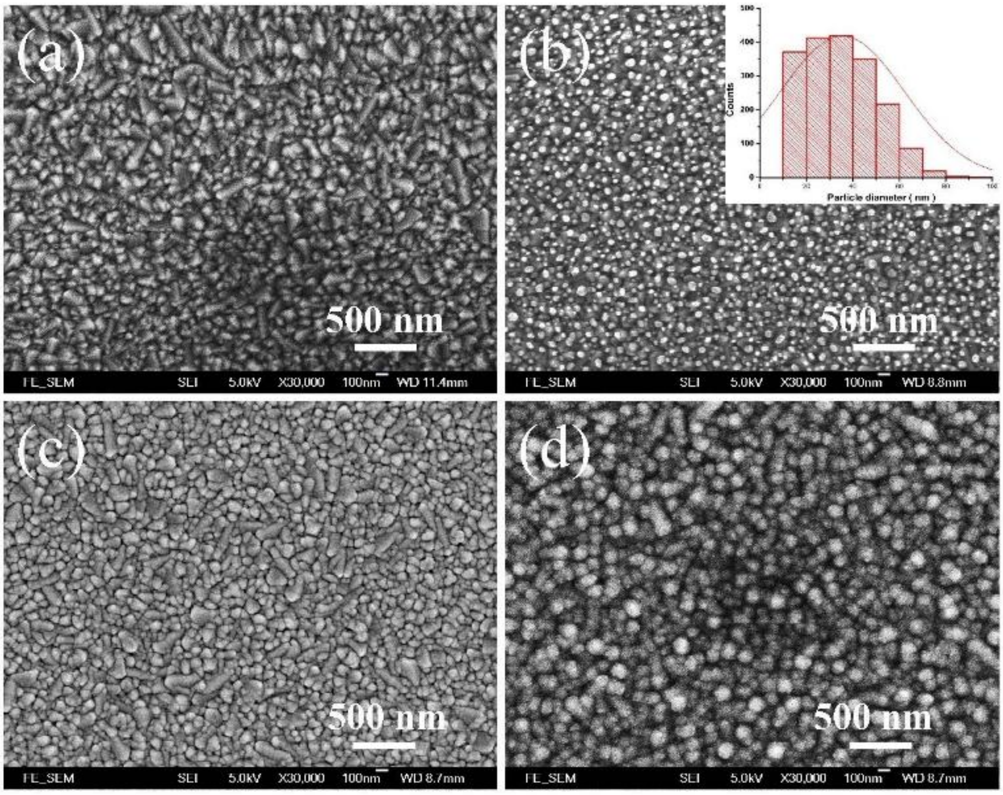

Figure 4.6 Scanning electron micrographs of the surface morphologies of different layers in the samples. (a) FTO glass; (b) Au NPs on FTO glass, deposited by the sputtering process; (c) rough Au film on FTO glass; (d) ALD-deposited TiO_2 film on the rough Au film. The inset in (b) is the histogram of the size of Au NPs.

Figure 4.6 displays the surface morphologies of the respective layers of the three types of TiO_2-based samples. The surface of FTO glass itself is already very rough as shown in Figure 4.6(a). For the Au NPs on the FTO glass, the deposited thin Au film with a thickness around 8 nm is transformed to discontinuous Au NPs after the annealing as shown in Figure 4.6(b).[142,143] When viewed from the top, the Au NPs exhibit nearly round shape and similar particle size. The histogram of the particle size distribution is obtained with the free software ImageJ as shown in the inset of Figure 4.6(b). The Au NPs have an average size of 35 nm with a standard deviation of approximately 11 nm. When the thickness of the deposited Au film is increased to 100 nm, the surface of Au film becomes rough and thus a pattern of densely packed metallic cluster grows up, which seems like a collection of many Au nanostructures with large variations of shape and size, as shown in Figure 4.6(c). The TiO_2 film deposited by the atomic layer deposition (ALD) process on the rough Au film has quite uniform grain size of TiO_2 nanoparticles as shown in Figure 4.6(d). These structural layers in a larger area are shown in Figure 4.7.

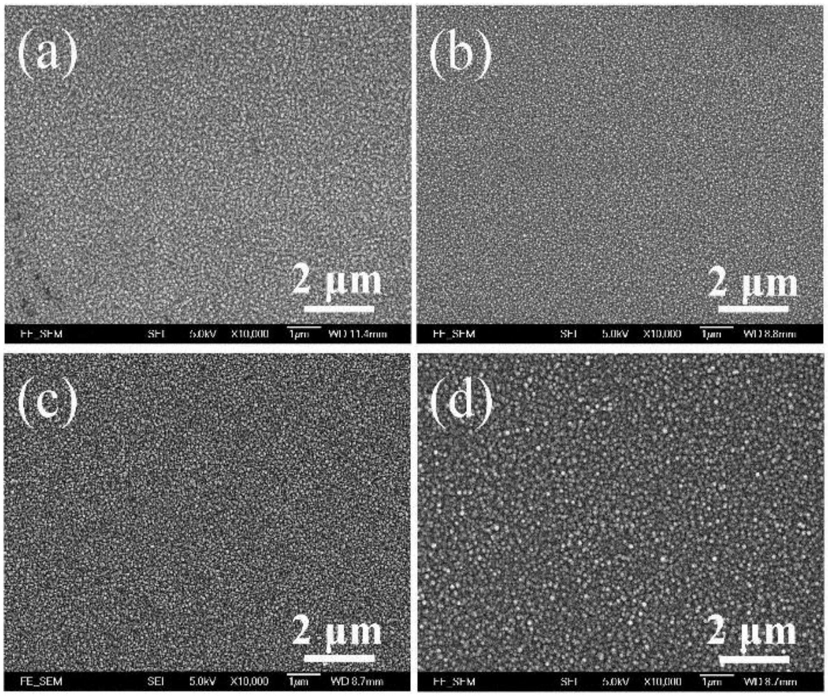

Figure 4.7 SEM surface morphologies of different layers in large area. (a) FTO glass; (b) Au NPs on the FTO glass, deposited by the sputtering process; (c) rough Au film on the FTO glass; (d) TiO_2 film deposited by the ALD method.

4.3.2 Influence of TiO_2 film thickness of TiO_2-Au bilayer

The thickness of the TiO_2 film plays an important role in the optical and photoelectrochemical properties of the TiO_2-Au bilayer. To examine this influence, a series of TiO_2 thin film are deposited onto the Au film by the ALD method, including 0, 5, 10, 20, 30 and 50 nm. The ALD is a precision growth technique that can passivate surface states to decrease the surface recombination velocity, which can synthesize thin film from only a few atomic layers to hundreds of nanometers[144,145]. Its layer-by-layer deposition allows highly conformal coating even on the dense and rough surfaces of nanostructures. Therefore, the as-deposited TiO_2 films with excellent step coverage have an amorphous structure. The thickness of TiO_2 film can be controlled by the deposition time according to the deposition condition. Moreover, the XRD patterns (Figure 4.8) of the TiO_2 films match the Joint Committee on Powder Diffraction Standards File (JCPDS no.21-1272), which confirms the anatase phase of TiO_2.[146] The XRD patterns of the bare TiO_2, the bare Au film and the FTO substrate are exhibited in Figure 4.9(c). It is well known that the anatase phase of TiO_2 has greater photocatalytic activity than the rutile phase due to the lower conduction band and higher hydrophilicity.[147]

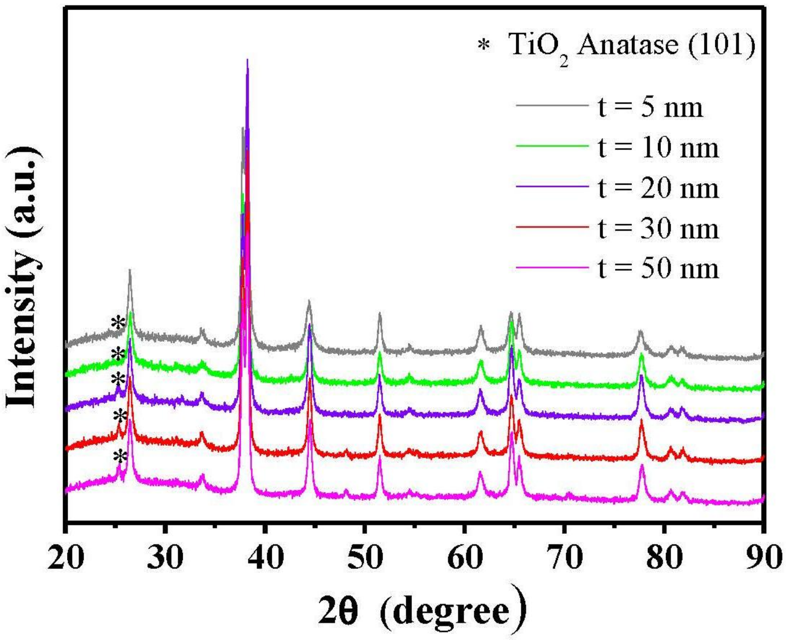

Figure 4.8 XRD plots of the TiO_2-Au bilayer samples with the TiO_2 film thicknesses of 5, 10, 20, 30 and 50 nm. For all the samples, the diffraction peak appears at $2\theta = 25.3°$, corresponding to the (101) orientation of anatase phase, while the other diffraction peaks are very weak. This indicates that the crystallographic phases of these TiO_2 films are all anatase-type. Moreover, the XRD intensity of these TiO_2 films goes up with the increase of the TiO_2 thickness.

Color photographs of the TiO_2-Au bilayer samples with various TiO_2 thicknesses are shown in Figure 4.9(a). The sample with the 0-nm TiO_2 film represents only the rough Au film, which looks bright yellow. The samples appear deepened yellow when the TiO_2 thickness is increased from 5 to 20 nm. The sample becomes dark blue when the TiO_2 thickness is 30 nm, and turns to jade for the 50-nm TiO_2. The AFM is also employed to characterize the surface morphology of the rough Au film (Figure 4.9(b)), which agrees well with the measured SEM image (Figure 4.6(c)). The mean roughness of the rough Au film is approximately 5 nm within the area of 2 μm × 2 μm and the root-mean-square (rms) roughness is 15 nm, indicating significant surface roughening. For the influence of the Au film thickness, it has little effect as long as the Au film is thick enough to block all the light and rough enough to enable strong, broadband absorption of visible light. Therefore, this study does not investigate the influence of Au film thickness, but simply maintains the Au film thickness at 100 nm, which is much thicker than the skin depth of Au film (about 13 nm). The surface of the 100-nm Au film after annealing is still very rough for plasmonic absorption.[148]

The reflection and transmission spectra of these TiO_2-Au bilayer samples are given in Figure 4.9(d) and (e). Figure 4.9(d) shows that the reflection first decreases with thicker TiO_2, reaches the minimum at 30 nm and then increases. From Figure 4.9(d), the transmission shares the similar trend, except that it has two peaks at around 500 nm and 700 nm, though the level of transmission is always < 10%. The absorption spectra of these TiO_2-Au bilayer samples with different TiO_2 thicknesses are also determined by $A = 1 - R - T$ as shown in Figure 4.9(f). It is seen that the absorption increases with the TiO_2 thickness from 0 to 30 nm, but starts to decrease when the thickness is over 30 nm.

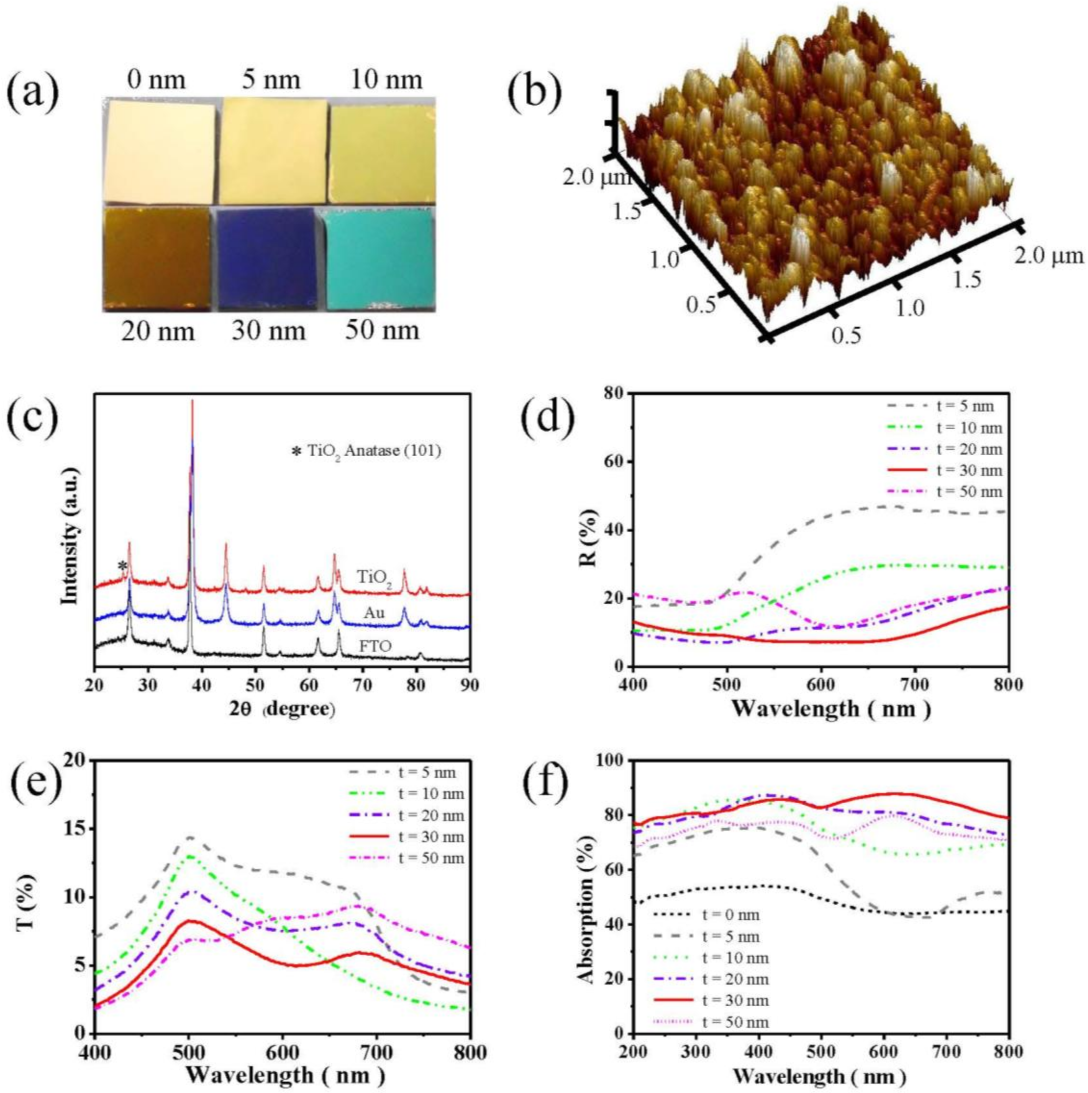

Figure 4.9 (a) Photographs and (f) absorption spectra of the TiO_2-Au bilayer samples with the TiO_2 thicknesses of 0, 5, 10, 20, 30 and 50 nm. The films are deposited by ALD at 100 °C and then annealed at 500 °C for 1 h; (b) atomic force micrograph of the surface morphology of the rough Au film on the FTO substrate; (c) the XRD patterns of the bare TiO_2, the bare Au film and the FTO substrate. (d) reflection spectra and (e) transmission spectra of the TiO_2-Au bilayers with the TiO_2 thicknesses of 5, 10, 20, 30 and 50 nm;

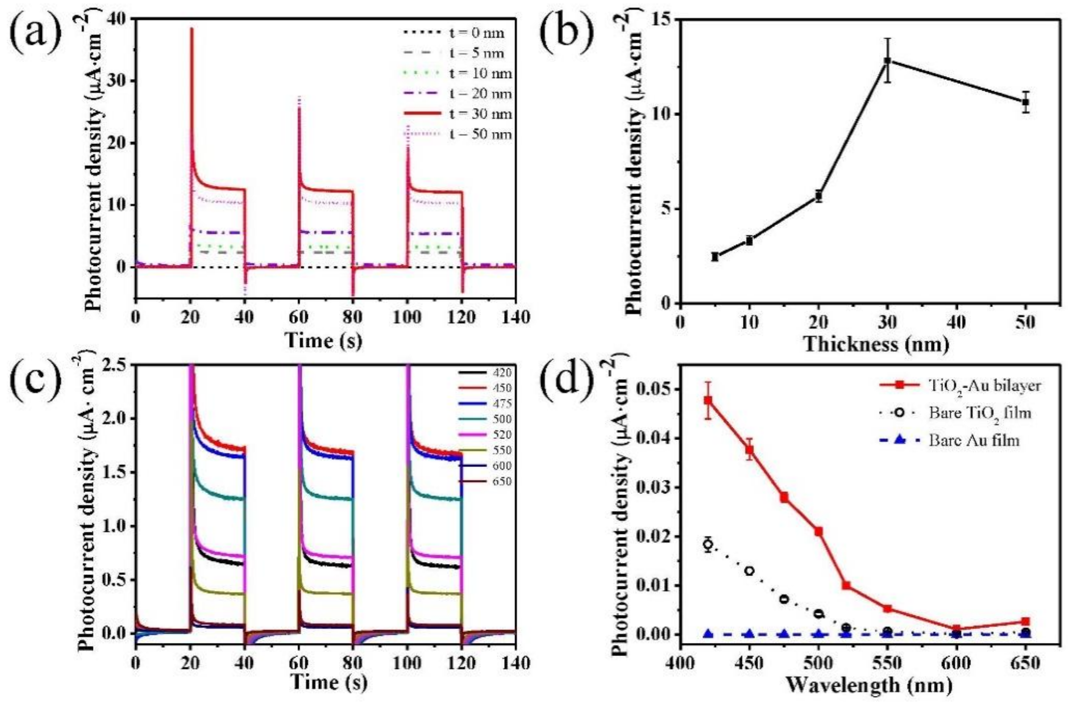

Figure 4.10 (a) *I-t* plots and (b) photocurrent intensities of the TiO_2-Au bilayer samples with different TiO_2 thicknesses of 0, 5, 10, 20, 30 and 50 nm.; (c) *I-t* plots under the irradiation of monochromatic light; and (d) action spectra (i.e., photocurrent versus light wavelength) of the TiO_2-Au bilayer with 30-nm-thick TiO_2 film (red line), the 30-nm-thick bare TiO_2 film (black line) and the bare Au film (blue line).

The results of *I-t* measurements are plotted in Figure 4.10(a) for the TiO_2-Au bilayer samples with different TiO_2 film thicknesses. It is seen that the photocurrents respond immediately and repeatedly to the turning on and off of light source. Figure 4.10(b) plots the measured photocurrent density as a function of the TiO_2 thickness, showing the maximum 12.4 $\mu A \cdot cm^{-2}$ at 30 nm. Therefore, the TiO_2-Au bilayer sample with the 30-nm-thick TiO_2 film has the highest photocurrent, this sample is named as the “optimal bilayer sample”. To further investigate the wavelength dependence, the optimal bilayer sample is illuminated with a broadband visible light source ($\lambda \geq 400$ nm) that delivers a total power of ~ 300 mW/cm^2 as mentioned in Section 4.3.1 . The *I-t* plots of the optimal bilayer sample are shown in Figure 4.10(c) for the wavelengths of 420, 450, 475, 500, 520, 550, 600 and 650 nm, respectively. For quantitative comparison, the action spectra (i.e., photocurrent density versus light wavelength) are plotted in Figure 4.10(d) for the optimal bilayer sample and its constituent layers – the 30-nm-thick bare TiO_2 film and the bare Au film. It is seen that the bare Au film has almost no response whereas the optimal bilayer sample has the highest result, showing significant enhancement as compared to the bare TiO_2 film. For the optimal bilayer sample, the photocurrent density drops quickly when the wavelength goes up to 600 nm and becomes very low afterward. The energy conversion efficiencies of the three samples can also be indicated by the incident photon to current efficiency (IPCE), which are extracted from the measured photocurrents and the incident spectrum. The IPCE of the optimal TiO_2-Au bilayer sample reveals a clear enhancement as compared to the bare TiO_2 film and the bare Au film, which is consistent with the action spectra plotted in Figure 4.10(d).

4.3.3 Simulation results of absorption spectra and electrical fields

Using the simulation methods as discussed in section 3.4 , the absorption spectral of the TiO_2-Au bilayer samples are calculated for different TiO_2 thickness. The results are plotted in .

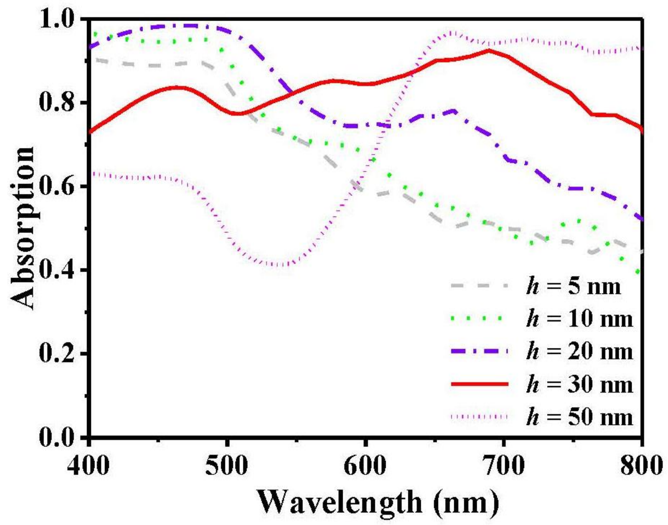

Figure 4.11 Simulated results of the absorption spectra of the TiO_2-Au bilayer samples. The thickness of TiO_2 film varies from 5, 10, 20, 30 to 50 nm.

Based on the physical structure and materials of the actual TiO_2-Au bilayer sample, the simulation model is built up as depicted in Figure 4.12(a), with the Au portion and the TiO_2 portion denoted by yellow and blue color, respectively. The model consists of three layers, from bottom to top, a flat Au film layer, an Au NPs layer and a TiO_2 layer. The FTO thin film is not included in the simulation since there is almost no transmission of light through the Au layer. As an approximation, the thickness of the flat Au film layer is 100 nm in the simulation. Considering the roughness of the Au film (see the AFM image in Figure 4.9(b)), the rough surface is represented by randomly-distributed particles.[149] In the simulation, the particles are randomly scattered on the surface in a space of 1 μm × 1 μm × 30 nm, with their diameters varying from 60 to 120 nm. The vertical positions of the particles are adjusted so that the highest particles are always attached to the upper boundary of the flat Au layer while the other particles may be partially embedded into the flat Au layer. The Au nanoparticles can be overlapped with each other, in which some larger domain can be formed occasionally to further account for the randomness of the distribution, the shape and the size. To mimic the TiO_2 film, the template method is adopted.[150] Each Au NPs is embraced by a shell layer of TiO_2, whose thickness is equal to the ALD deposition thickness approximately. For the bare area without the Au NPs covered, a flat TiO_2 film layer with the deposition thickness is also added above the flat Au layer. The meshing order of these Au NPs has higher priority than the TiO_2 layers to ensure the coverage by TiO_2 at only the outer boundaries. The transverse dimension of the model structure is 1 μm × 1 μm and the number of Au NPs is 320 in the simulation. With the random positioning, the number of Au NPs is essential for simulating the surface roughness of the Au film, and a relatively small number generally implies a larger surface roughness. In this way, the roughness of Au surface of the real TiO_2-Au bilayer can be well represented. The simulated absorption spectrum (Figure 4.11) is in good agreement with the experimental result (Figure 4.9(f)).

Regarding the boundary condition, Perfectly Matched Layer (PML) is used for both the top and bottom boundaries, while periodic condition is employed for the other side boundaries. The periodic condition is a good approximation as the model's transverse dimension is large as compared to the particle size to support the randomness of distribution. The 4th level auto non-uniform meshing is applied to balance the simulation accuracy and the computation load. The S parameter analysis group is implemented for the absorption analysis, in which a plane source is used and the far-field measurement is conducted. In the simulations, the average thickness of the TiO_2 layer is varied from 5 to 50 nm. The absorption spectrum of the absorber is recorded for each thickness, within the wavelength range of 400 – 800 nm.

The simulated absorption spectrum (black line) for the TiO_2-Au bilayer sample with the 30-nm TiO_2 film resembles approximately the measured spectrum (red line) as shown in Figure 4.12(b). As for the various values of TiO_2 thickness, including 5, 10, 20, 30, and 50 nm, the absorption spectra of the absorbers are presented in Figure 4.11, which coincide with the experimental results in Figure 4.9(f). The optimal absorption occurs at the thickness of 30 nm.

According to Figure 4.12(b), the maximum absorption is about 90% near 650 nm, and a shallow dip occurs near 500 nm. To further understand the optical property of the 30-nm TiO_2-Au bilayer, the electric field distributions are also simulated in some transverse cross-sections. The position Z of the cross-section is defined using the vertical displacement from the upper surface of the flat Au layer. The electric field distributions for cross-sections at Z = 0, 30, 60, and 90 nm are depicted in Figure 4.12(c)-(f), respectively. It can be seen that some hot spots occur near the sites of the particles, indicating the LSPR effect and the plasmonic coupling effect. These effects play a central role in the overall enhancement of absorption. For the broadband absorption, the shell layer and the flat layer of TiO_2 can be regarded as the effective index media for index matching. The TiO_2 layer also modifies the coupling between the Au NPs, which can be used to tailor the absorption in the visible light band.

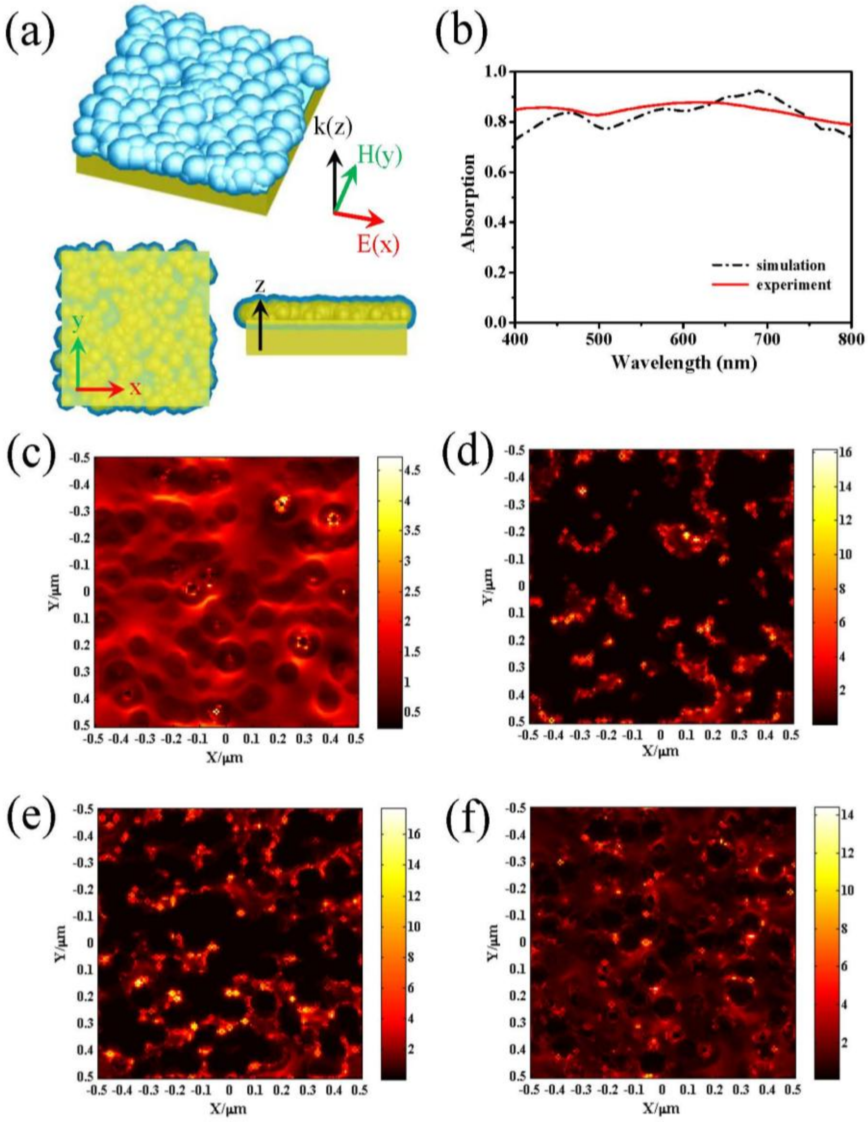

Figure 4.12 Simulation results. (a) Perspective view, top cross-sectional view (XY plane) and side cross-sectional view (XZ plane) of the model for the TiO_2-Au bilayer sample; (b) comparison of the measured absorption spectrum with the calculated one using the FDTD method for the TiO_2-Au bilayer sample whose TiO_2 film is 30-nm thick; The electric field distributions on the transverse cross-sections located at (c) Z = 0 nm, (d) Z = 30 nm, (e) Z = 60 nm and (f) Z = 90 nm, here Z = 0 is located at the upper surface of the flat Au layer.

4.3.4 Mechanism of photocurrent generation

For effective generation of photocurrent, the optical absorption is only the first step. As mentioned above, the enhancement of optical absorption is due to the LSPR effect and the plasmonic coupling of the random Au nanostructures in the rough Au film.[48,117,151,152] The next step to the photocurrent generation relies on the excitation, separation and transfer of charge carriers.

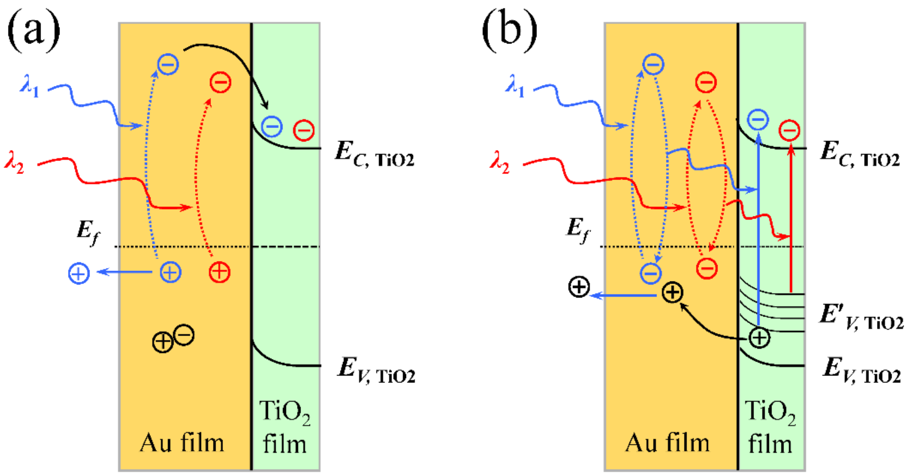

Figure 4.13 Mechanisms of the photocurrent generation in the TiO_2-Au bilayer. (a) Hot electron injection, for which the rough Au film absorbs photons of different wavelengths to generate hot electrons, whose potential levels of excited states are high enough to overcome the potential barrier to be injected into the TiO_2 layer. (b) Plasmonic resonance energy transfer, for which the plasmonic resonance of Au nanostructures generates intense electric fields in the TiO_2 layer and excites the electrons of TiO_2 to the conduction band. For the energy's point of view, the photon energy excites the Au electrons, which falls back and transfers the energy to the TiO_2 electrons via the intense electric field near the plasmonic hot spots.

Figure 4.13 depicts the two mechanisms of the photocurrent generation in the TiO_2-Au bilayer: *hot electron injection* (HEI) and *plasmonic resonance energy transfer* (PRET). Both mechanisms are widely used for the plasmonic enhancement of photocurrent in literature.[108,48,125,136,139.141] The HEI is illustrated in Figure 4.13(a), the light incident on the sample excites the plasmonic resonance of electrons in the Au nanostructures, part of these plasmons decays into hot electrons, which are then fed into the conduction band of TiO_2. This enables the creation of active electrons in the TiO_2 nanoparticles even in the absence of direct light absorption by TiO_2.[91,153] As the rough Au film of the TiO_2-Au bilayer enables the plasmons at different wavelengths, hot electrons of different energies may be excited and injected to the TiO_2 conduction band. In contrast, the PRET goes through a different way as shown in Figure 4.13(b). The plasmonically excited electrons in the Au film do not migrate into the TiO_2 film, instead they can transfer the energy to the valence-band electrons of TiO_2 film to excite them to the conduction band of TiO_2. This energy transfer process can be enabled by the intense electric field of plasmonic resonance. More specifically, the incident photons excite the collective oscillation of the electrons in Au nanostructures, and thus generate intense oscillating electric fields nearby the Au surface. The region with intense electric field is often called hot spot. The hot spots can penetrate into the TiO_2 film (typically by a distance of ~10 nm) and thus the oscillating electric fields can excite the TiO_2 electrons.

The HEI and the PRET have different requirements. The former needs the Au nanostructures to be directly in physical contact with the TiO_2 for hot electron transfer and also the photon energy to be high enough to overcome the potential barrier at the Au/TiO_2 interface, which has a barrier height of about ~1 eV. The latter requires the overlapping of the absorption spectra of the Au nanostructure and the TiO_2 film, and needs also the extension of the hot spot into the TiO_2 film. Fortunately, all of these conditions are satisfied in our TiO_2-Au bilayer. For example, the rough Au surface is directly covered by the TiO_2 film, and thus the direct electron transfer is enabled and the hot spots can cover part of the TiO_2 film near the rough Au surface; over the strong absorption band of 400 – 800 nm of the TiO_2-Au bilayer (see Figure 4.2(c)), the corresponding photons energy is in the range of 3.1 – 1.55 eV, sufficiently higher than the potential barrier ~ 1 eV; in addition, the TiO_2 film has certain absorption over 400 – 700 nm (see Figure 4.2(c)) due to the defects in the TiO_2 film whereas the rough Au film itself has flat absorption over 400 – 800 nm, enabling the overlapping of the absorption spectra. Based on these, we attribute to both the HEI and the PRET for the photocurrent enhancement.

For the influence of the TiO_2 film thickness on the photocurrent of the TiO_2-Au bilayer structure, the TiO_2 film serves three functions. First, the TiO_2 film is a dielectric layer and acts as the index matching layer and assists the optical coupling of the incident light into the rough Au film.[139] Thicker or thinner TiO_2 film would deteriorate the effects of index matching and optical coupling. As a result, there is an optimal TiO_2 thickness for optical coupling. Second, the ALD-deposited and thermally-annealed TiO_2 film has more defects and causes additional energy states inside the TiO_2 bandgap, enabling to absorb visible light. Since the defects and the associated energy states vary with the TiO_2 thickness, the absorption of visible light is changed. Third, the TiO_2 film of the TiO_2-Au bilayer provides an electron receptor and also an diffusion layer for the transport of the hot electrons to the TiO_2/solution interface for photochemical reactions.[154,155] Thin TiO_2 film causes low volume to receive electrons but enables fast transport of electrons due to the short diffusion length, whereas thick TiO_2 film benefits the electron reception but impairs the electron transport due to the long diffusion length. The combined effect of the optical coupling, the defect-induced visible absorption and the electron reception/transport results in the existence of an optimal thickness of TiO_2 film, which happens to be 30 nm in this work. This is the reason that the TiO_2-Au bilayer yields the highest photocurrent when the TiO_2 film is 30 nm thick, as shown in Figure 4.10(b). As a consequence, the optimal efficiency of photocurrent generation is achieved when the TiO_2–Au bilayer sample has the 30-nm-thick TiO_2 film.

4.4 Summary

In summary, we have examined the rough Au film to sensitize TiO_2 to visible light over 400 – 800 nm. Burying the rough Au film under the TiO_2 film forms the TiO_2-Au bilayer and induces the broadband optical absorption and the significant enhancement of photocurrent as compared to the other two types of control samples, the TiO_2-AuNP hybrid and the bare TiO_2 film. Such enhancement is ascribed to the LSPR and coupling effects of the random Au nanostructures in the rough Au film for the strong visible absorption and to also the Schottky junction in the Au/TiO_2 interface for the separation of photogenerated electrons and holes. Besides, the optimal thickness of TiO_2 film for the TiO_2-Au bilayer is found to be 30 nm. The superior optical and photoelectrochemical properties of the TiO_2-Au bilayer demonstrate its great potential as the photoelectrode for future environmental and energy technologies. Moreover, this new photoelectrode possesses the merits of high absorption efficiency, broadband absorption of visible light, low production cost and easy fabrication process, and brings new insight into the design and preparation of advanced visible-light responsive photocatalytic materials.

CHAPTER 5

PLASMONIC BROADBAND VISIBLE-LIGHT ABSORBERS BASED ON SANDWICHED AU NANOPARTICLES AND AU ROUGH FILMS

The previous Chapter has introduced the TiO_2-Au bilayer with superior absorption and photocatalysis properties by the ALD deposition method. In order to further improve the electron transfer between the absorber (TiO_2 surface) and electrolyte, as well as to reduce the complexity of TiO_2 fabrication, in this chapter we report an original work of plasmonic black absorber that sandwiches a 150-nm TiO_2 layer between a layer of random Au nanoparticles and a rough Au surface (200 nm thick) by the sol-gel method. The combined plasmonic effect of the Au nanoparticles and the Au rough surface enables a strong absorption (72% – 91%) over 400 – 900 nm and a significantly enhanced photocurrent (by 20 folds) as compared to the bare TiO_2 film. The strong absorption to visible and near infrared light, and the much enhanced photocurrent make the black absorber an ideal material for solar applications such as photocatalytic, photosynthetic, photovoltaic and photothermal systems.

5.1 Introduction

As an abundant and irreplaceable resource, solar energy has been intensively exploited for human activities. Photocatalysis utilizes semiconductors to transform photon energy into chemical energy by absorbing photons and generating electrons without harmful byproduct.[156,157,158] Although TiO_2 is the most promising photocatalyst thanks to its many merits such as superior photoactivity, high photostability, proven biosafety and abundant supply, it has its own Achilles' heel – the wide bandgap (~3.2 eV). This limits its absorption to only the UV light (< ~ 388 nm), making it absorb only about ~ 4% of solar energy. Many attempts have been made to enhance the response of TiO_2 to the visible light and even the near infrared light. Among them, doping of non-metallic elements such as nitrogen,[159,160] carbon,[161,162] and sulphur,[124,163] have attracted much attention, however, the doped TiO_2 photocatalysts are often not stable enough.

Recently, plasmonic photocatalysis has risen up as a very promising technology for high-performance photocatalysis.[164,165] It involves dispersal of noble metal nanoparticles (NPs) (commonly Au NPs and Ag NPs in the sizes of tens to hundreds of nanometers) into semiconductor photocatalysts by either dispensing on the surface or embedded in the semiconductors.[166,167,168] The localized surface plasmonic resonance (LSPR) effect of noble metal NPs enables it to absorb the visible light and transfer the energy to TiO_2 for photocatalysis.[169,170,171,172] Nevertheless, the LSPR effect has two fundamental limits. One is that the resonant effect limits its absorption bandwidth to a narrow wavelength range (typically ~ 50 nm or smaller for uniform nanospheres).[172] The other is that the absorption coefficient is usually low due to the strong scattering. To shift the LSPR resonance to the visible range, the size of NPs has to be large (~ 50 – 100 nm) and thus the scattering becomes prominent. For instance, the Au nanosphere with the diameter of

80 nm has the resonance wavelength at 550 nm, but its scattering coefficient is already 0.65 of the absorption coefficient.[173] And larger nanospheres shift the resonance peak to longer wavelength, but at the cost of larger scattering. Although the scattering may contribute to the photocurrent by increasing the photon-photocatalyst interaction length,[165] it is more desirable to have photons strongly absorbed by the NPs, especially when the photon energy is lower than the bandgap of photocatalyst materials (e.g., visible light to TiO_2). Therefore, a blackbody-like absorber would be ideal to make full use of the whole solar spectrum.[116,133,174,115,175] Recently, blackbody-like metallic layers in the form of diffraction grating have been reported for strong absorption over a wide wavelength.[176] Special efforts have been made to enhance the absorption to the infrared light as well.[177,178,179] However, those man-made regular nanostructures are often polarization dependent and involve complicated photolithographic processes.

This section reports a unique black absorber based on the plasmonic effect of random Au nanostructures, which exhibits strong absorption (> 70%) of non-coherent sunlight over 400 – 900 nm and overcomes the major problems of current LSPR-based photocatalysis technology. The absorber is composed of a TiO_2 layer sandwiched between a layer of Au nanoparticles (AuNPs) and a rough Au layer (in short, AuNP/TiO_2-Au film). For comparison, another three structures such as the bare TiO_2 film, the AuNPs on TiO_2 layer (named as AuNP/TiO_2 hereafter) and the TiO_2 layer on Au layer (named as TiO_2-Au film) are developed as well. Experiments will be conducted to prove that the black absorber has apparently superior photocatalytic performance than the other three structures, and simulations will be carried out to show the origin of strong absorption. It is worth noting that the fabrication involves only simple processes, such as sputtering and annealing, and requires no photopatterns, making it easy to fabricate large-area samples at low cost.

5.2 Experimental details

5.2.1 Device Design and Fabrication

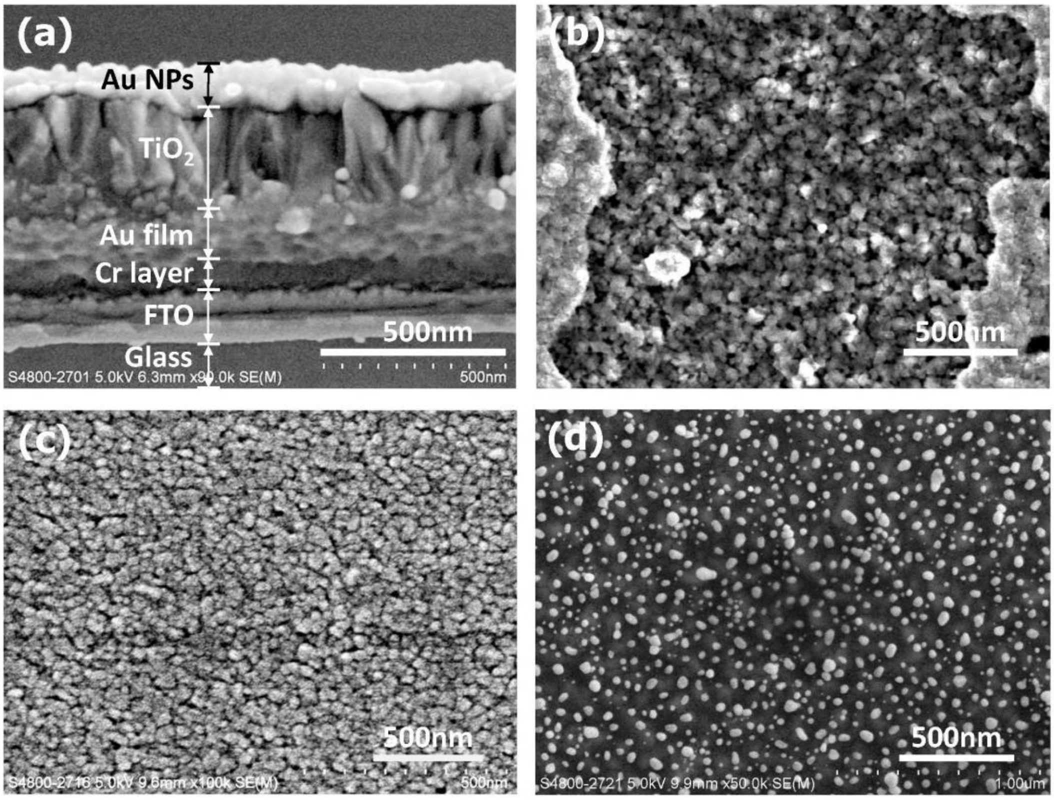

Figure 5.1 (a) Scanning electron micrograph of the cross-section of the absorber. The thicknesses of the Au layer and the TiO_2 layer are about 200 nm and 150 nm, respectively; and those of the FTO layer and the Cr layer are about 100 nm and 10 nm, respectively. (b) The Au nanoparticles on the top surface. (c) The TiO_2 film layer. (d) Top view of the Au layer exposed from an etched window of the TiO_2 layer, showing that the Au layer is very rough and consists of nanopores and nanoparticles.

The plasmonic black absorber and all the other films are fabricated on the substrate of fluorine-doped tin oxide (FTO) glass. First, a thin Cr layer (~ 10 nm thick) and a continuous Au layer (~ 200 nm thick) are deposited by magnetron sputtering on the FTO substrate. The working pressure of Ar and the sputtering power are 6 pa and 60 W, respectively. The layer thicknesses are controlled by the sputtering time. The Cr layer is to enhance the adhesion and the electrical conduction of the Au layer to the FTO substrate.

Then, the TiO_2 layer is deposited by the spin-coating method as elaborated in section 3.1.1 . Although the annealing temperature of 500 ^{o}C is pretty high and may cause the oxidation problem, previous studies and our experience show that stable Au films and Au nanoparticles can still be obtained safely.

Finally, sputtering and thermal annealing are utilized to fabricate the random distribution of AuNPs onto the surface of TiO_2 layer. The fabrication procedures are presented in section 3.1.2 . The SEM micrographs are shown in Figure 5.1. When the Au layer is deposited onto the TiO_2 layer for 10 s, the AuNPs after annealing have the size in the range of 40 – 80 nm, as shown in Figure 5.2.

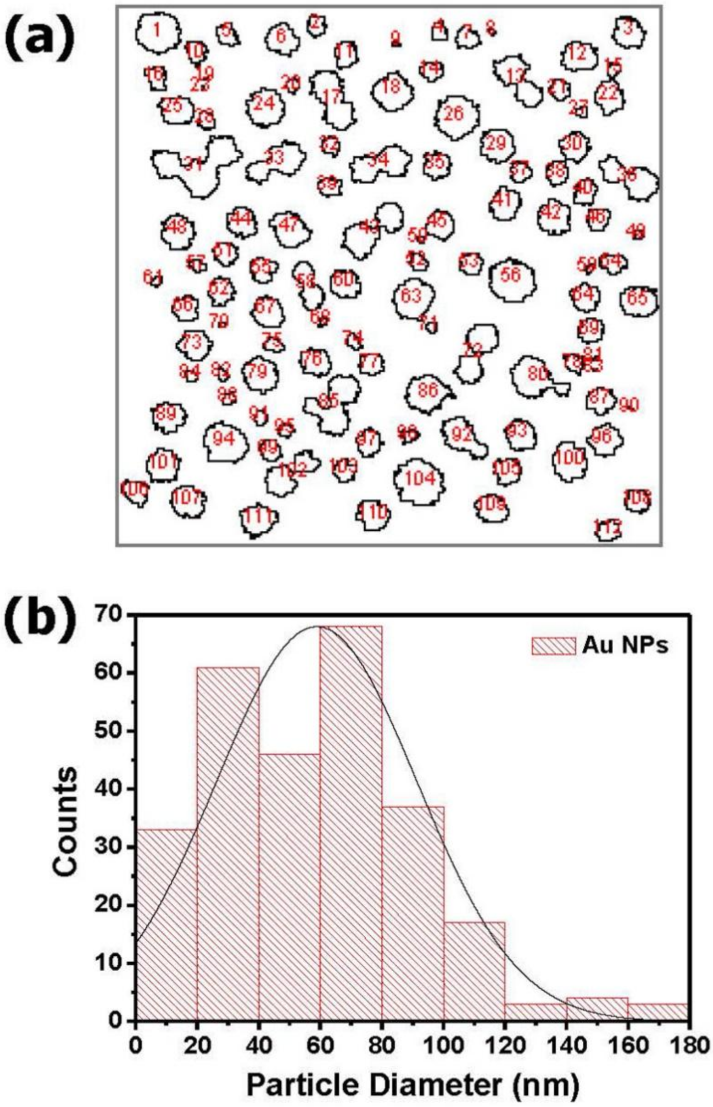

Figure 5.2 (a) Profile of Au nanoparticles in a small region of Figure 5.1(d). (b) Histogram of the size of Au nanoparticles in Figure 5.1(d), as analyzed by using the free software tool ImageJ.

5.2.2 Characterization

The surface morphology and the cross-section of the plasmonic blackbody-like structure are evaluated by the scanning electron microscope (Hitachi S-4800, Hitachi High-Technologies Corporation, Tokyo, Japan) with a cold field emission electron source and an in-lens secondary detector. Typically, the images are acquired with an acceleration voltage of 5 kV. UV-Vis spectrophotometer (Perkin Elmer Lambda 750) is employed to measure the absorption of the black absorber and the other samples of control experiments. The reflection spectra are performed with an integrating sphere that uses a $BaSO_4$ plate as the reference. This means that both the direct reflected light and the diffuse scattering light are included in the reflection measurement. The photocurrent is characterized using a three-terminal potentiostat (Figure 5.3 (b)). The black absorber, a Pt electrode and a saturated calomel electrode (SCE) are used as the working, the counter, and the reference electrode, respectively. The working electrode potential is set at 0 V versus SCE. Photocurrent is measured under the irradiation of a Xe lamp (100 mw/cm^2) fixed with a UV filter (cut-off wavelength 400 nm).

5.2.3 FDTD simulation

To model the complicated structure, the AuNP/TiO_2-Au film is simplified into five layers. More specifically, Layers A and B represent the continuous part and the rough surface of the Au layer, respectively; Layer C stands for the continuous part of the TiO_2 layer; Layer D represents the overlapping of the TiO_2 rough surface and the AuNPs; and Layer E represents the independent AuNPs on the surface of TiO_2. The 3D FDTD has been performed in a domain of 1 μm × 1 μm × 100 nm. For Layer A, the Au layer is 100 nm thick. For Layer B, it is represented by 3000 AuNPs with the size randomly distributed in 20 – 40 nm. For Layer C, the TiO_2 layer is 100 nm thick. For Layer D, it is represented by 800 random TiO_2 particles with the diameter in 40 – 60 nm. For Layer E, it contains 300 AuNPs with the size in 20 – 100 nm, following the histogram in Figure 5.2(b).

In the 3D FDTD simulation using Lumerical FDTD Solutions, the periodic boundary conditions are employed in both *x* and *y* directions, and the perfectly matched layer (PML) boundary condition is employed in the *z* direction. Although the distribution of random particles is not periodic, the periodicity of the unite cell in both the *x* and *y* directions are set as 1000 nm, which is far greater than the radius of the random particles to simulate the rough Au surface in the real structure. The FDTD lattice is completed with the auto non-uniform mesh type, the 6th level with the mesh type of high accuracy to ensure reliable results.

The absorption is calculated by the equation $A(\lambda) = 1 – R(\lambda) – T(\lambda)$, where $R(\lambda) = |S_{11}|^2$ is the reflection and $T(\lambda) = |S_{21}|^2$ is the transmission. Since the bottom Au layer (thickness 160 nm) is much thicker than its typical skin depth, there is almost no transmission in the whole wavelength range, i.e. $T(\lambda) = 0$. In this case, the formulation of absorption can be simplified into $A(\lambda) = 1 – R(\lambda)$. Frequency-domain field and power monitor are used to investigate the S-parameters of transmission (S_{21}) and reflection (S_{11}) of a single unite cell.

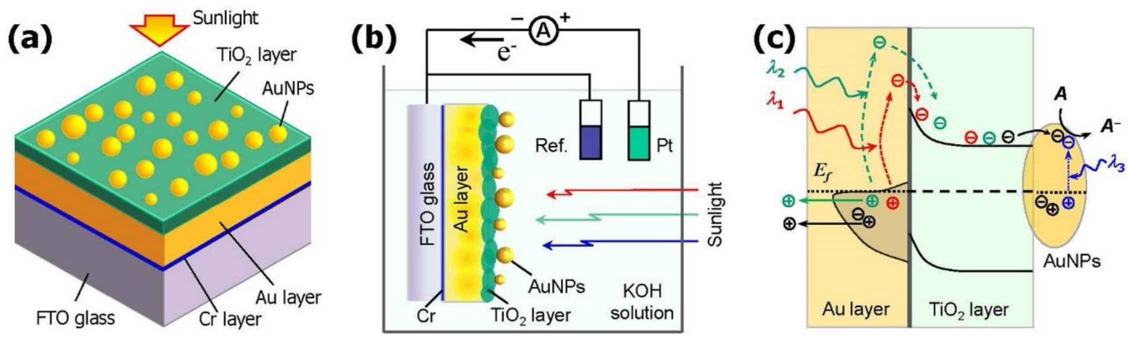

Figure 5.3 Plasmonic black absorber that is constructed by the AuNP/TiO2-Au film. (a) Layer structure. From bottom to top, it consists of a rough Au layer on the FTO glass substrate, a thin TiO_2 layer as the photocatalytic layer and a layer of Au nanoparticles on the top. (b) Three-terminal potentiostat setup for measuring the photocurrent of the perfect absorber. (c) Excitation and transfer of hot electrons in the absorber. The electrons flow from the Au layer toward the Au nanoparticles.

5.3 Experimental results

5.3.1 Layer structure

From top to bottom, the structure of black absorber consists of a layer of randomly distributed AuNPs as the plasmonic absorber, a TiO_2 thin layer as the photocatalyst and a layer of rough Au layer as another plasmonic absorber (see Figure 5.3 (a)). To lead out the photocurrent, the rough Au layer sits on a glass substrate coated with a transparent conducting FTO film. To enhance the adhesion between the FTO film and the rough Au layer, a thin chromium layer is coated. Figure 5.3 (b) shows the three-terminal potentiostat setup for the measurement of photocurrent in the KOH solution. The black absorber acts as the working electrode, a platinum plate as the counter-electrode and a saturated cell as the reference electrode. Figure 5.3 (c) exemplifies the working principle. The rough Au layer absorbs photons of various energies to generate hot electrons, which are fed into the TiO_2 layer.[180,181] The AuNPs serve mainly two functions, an electron trap and an LSPR absorber. As the electron trap, the AuNPs accumulates the hot electrons from the TiO_2 layer and also provides a fast lane for the transfer of electrons to the electrolyte.[182] As the LSPR absorber, the AuNPs assist the absorption of the photons of its own LSPR wavelength and contributes to the photocatalysis as well. In this manner, the Au rough layer and the AuNPs work together to absorb a broad range of visible and near-infrared light in the solar light.

5.3.2 Micrographs

Figure 5.4(a) shows the pseudo-color SEMs of the cross-section of the plasmonic black absorber (see Figure 5.1 for the corresponding grayscale picture). For the Au layer and the TiO_2 layer, large grains can be observed and their boundary is not straight and not clear. In fact, they have partial overlap along the boundary and form effectively a thin Au-TiO_2 composite layer, which ensures good physical contact for the transport of photo-excited electrons from the Au layer to the TiO_2 layer. It is interesting to see that most of the TiO_2 gains run continuously along the vertical direction, which is beneficial to the charge transfer across the TiO_2 layer. Thicknesses of the Au layer and the TiO_2 layer are about 200 nm and 150 nm, respectively. It is noted that the Au layer is thick enough to block all incidence light and thus the transmission becomes negligible. The AuNPs on the surface of TiO_2 layer are fabricated by the sputtering and annealing method. Particle sizes are controlled by the deposition thickness of Au and the annealing conditions.

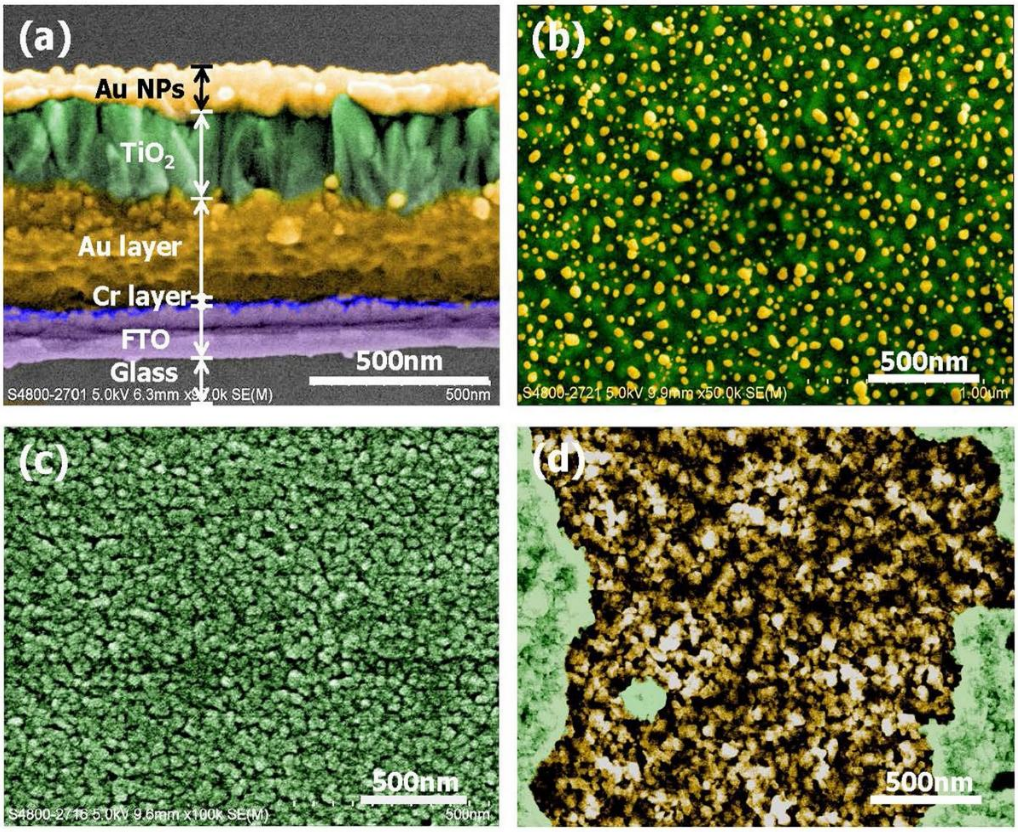

Figure 5.4 (a) Pseudo-color scanning electron micrograph of the cross-section of the absorber. The thicknesses of the Au layer and the TiO_2 layer are about 200 nm and 150 nm, respectively; and those of the FTO layer and the Cr layer are about 100 nm and 10 nm, respectively. (b) The Au nanoparticles on the top surface. (c) The TiO_2 film layer. (d) Top view of the Au layer exposed from an etched window of the TiO_2 layer, showing that the Au layer is very rough and consists of nanopores and nanoparticles.

From Figure 5.4(b), most of the AuNPs are well dispersed. The histogram shows the size of AuNPs mainly ranges from 40 to 100 nm, and is mostly at 70 nm (see Figure 5.2(b)). Figure 5.4(c) show the typical morphology of the interlayer TiO_2, which is uniform and continuous. A thin Au-TiO_2 composition layer forms at the boundary. Figure 5.4(d) shows the top-views of the Au layer (by etching a window in the TiO_2 layer).

The Au layer is very rough, with dense nano-cavities (or nanopores) and Au nanostructures of varying geometries. The average roughness is 11.0 nm (see Figure 5.5). Such a rough surface of the Au layer is the key to the broad absorption due to the plasmonic effects of the nano-cavities and the Au nanostructures and their coupling effect. [116,133,174,118,183]

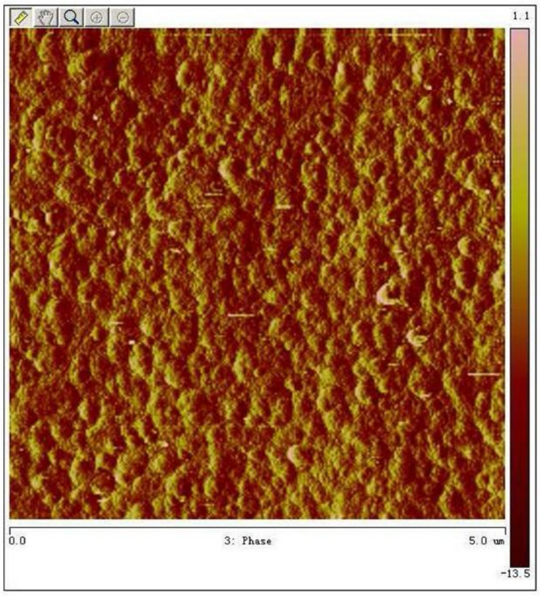

Figure 5.5 AFM surface profile of the rough Au layer under the TiO_2 layer. The area is 5 μm × 5 μm. The root mean squared (RMS) roughness is 11.0 nm.

5.3.3 Characterization

Figure 5.6 plots the absorption spectrum of the black absorber (i.e., AuNP/TiO_2-Au film) as compared with those of the bare TiO_2 film, the AuNP/TiO_2 film and the TiO_2-Au film. The insets of Figure 5.6 show the corresponding photos under the UV cut-off solar light (λ > 400 nm). The bare TiO_2 film looks pale white under sunlight and has very low absorption. For the TiO_2 layer that are loaded only with AuNPs (i.e., the AuNP/TiO_2 film), it shows a color of light pink (see the inset of Figure 5.6). The spectrum has an absorption peak at around 560 nm but the absorption coefficient is still low (< 15%). The absorption peak can be ascribed to the LSPR excitation effect of the AuNPs. For the TiO_2-Au film, its photo becomes dark brown, and the absorption coefficient is significantly increased (> 50%) over the whole range of 400 – 900 nm. This is an evidence of high absorption of the rough Au layer, though there is a valley of absorption near 600 nm. It is particularly interesting to see that the absorption rises up when the wavelength is > 600 nm. This is opposite to most of the photocatalysts that use uniform noble metal NPs, whose absorption often drops significantly for the long wavelength part of visible light and the near-infrared region.[84] This feature can be regarded as a spectral signature of the black absorbers.[115] For the AuNP/TiO_2-Au film of our research focus, the absorption coefficient is further enhanced to > 72% over 400 – 900 nm. Particularly, a peak absorption of 91% appears at ~ 600 nm, thanks to the LSPR absorption of AuNPs.[184,185] It is worth highlighting that the photo of the sample shows a deep dark color (see the inset of Figure 5.6), well proving its likeness to "blackbody". For the colors of different samples, the pale white color of the bare TiO_2 film is attributed to its low and quite flat absorption in 450 – 750 nm; the pink appearance of the AuNP/TiO_2 film is rendered by its relatively higher absorption in short wavelength region in 400 – 550 nm; the brown color of the TiO_2-Au film is owning to the drop of absorption in 500 – 650 nm; and the dark color of the AuNP/TiO_2-Au film is a result of the very high absorption over the whole range of 400 – 900 nm.

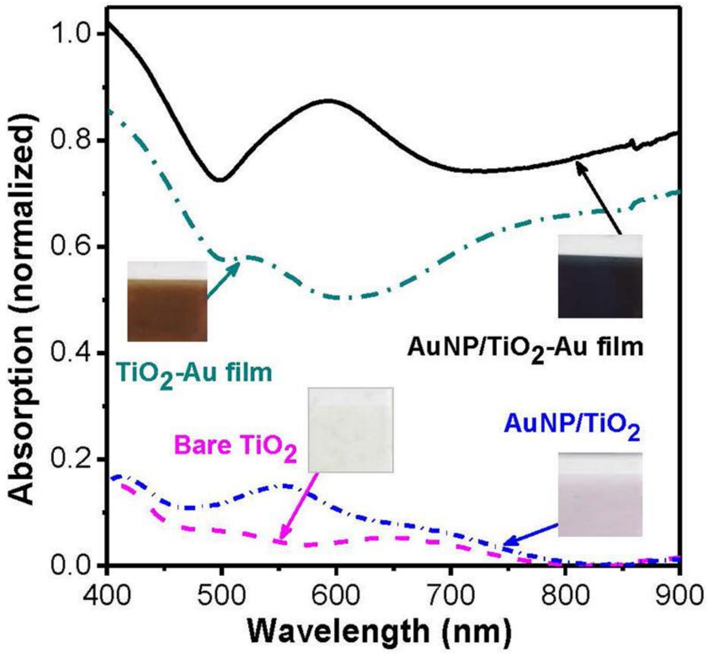

Figure 5.6 The measured absorption spectra of different film samples. The insets show the photos of the films. The bare TiO_2 film presents very low absorption, the AuNP/TiO_2 film has also low absorption but a plasmonic absorption peak at ~560 nm, the TiO_2-Au film shows a much enhanced absorption, where the AuNP/TiO_2-Au film exhibits strong absorption (> 72%) over the whole range of 400 – 900 nm and the maximum absorption of 91% at ~600 nm.

5.3.4 Photoelectrochemical properties

To study the photo-induced charge separation, the photoelectrochemical (PEC) properties of the bare TiO_2 film, the AuNP/TiO_2 film, the AuNP/TiO_2-Au film and the TiO_2-Au film are tested under the on-off illumination of a broadband visible source (400 – 900 nm, ~50 mW/cm^2) using the setup as shown in Figure 5.7 (b). The linear sweep voltammograms (LSV) are performed both in dark and under visible-light illumination (see Figure 5.7(a)), which reveals an apparent response to light on/off switching at different bias potentials. The chopped *I-t* curves are measured and recorded at a constant potential of 0 V (see Figure 5.7(b)), which is in good agreement with the *I-V* curves at 0 V bias voltage. Clearly, the bare TiO_2 produced little photocurrent density, < 0.7 μA cm^{-2}, which is just above the background dark current. As expected, a significant photocurrent density enhancement is observed on the AuNP/TiO_2-Au film (i.e., the black absorber), with a photocurrent density of ~15 μA·cm^{-2} (take the values at 90 s). The enhancement factor is ~ 20 as compared to the bare TiO_2 film. The TiO_2-Au film enhances the photocurrent density to ~ 5 μA·cm^{-2} in the absence of AuNPs loading, yielding an enhancement factor of ~ 8 with respect to that of the bare TiO_2. On the other hand, the addition of AuNPs onto the TiO_2 layer has just doubled the photocurrent in the absence of Au layer. Generally, the magnitude of photocurrent follows the AuNP/TiO_2-Au film > the TiO_2-Au film > the AuNP/TiO_2 film > the bare TiO_2 film, which is in good agreement with the order of absorption spectra in Figure 5.6. The large photocurrent of the AuNP/TiO_2-Au film as compared to that of the TiO_2-Au film is attribute to the fast-lane transfer and the LSPR absorption of the AuNPs as explained above. For the AuNP/TiO_2 film, its photocurrent is very small as compared to the AuNP/TiO_2-Au film, owing to the low absorption ability as seen in Figure 5.6. Regarding to the influence of the layer thicknesses in the AuNP/TiO_2-Au film, it is found that the current combination (i.e., 200 nm thick for the Au layer and 150 nm for the TiO_2 layer) yields the best absorption spectrum and the highest photocurrent; a thicker or thinner Au layer would reduce the level of absorption coefficient and the flatness of the absorption spectrum; similarly, a thinner TiO_2 layer causes a reduction of absorption but a thicker TiO_2 layer lowers the photocurrent slightly, possibly due to the larger grain size and the longer transport distance of electron from the Au layer to the electrolyte. For the origins of photocurrents in the AuNP/TiO_2-Au film and the TiO_2-Au film, the contribution of hot electrons can be inferred from the corresponding chopped I-V curves in Figure 5.7(a) and the I-t plots in Figure 5.7(b): their values are positive in the circuit connection of Figure 5.7 (c), showing that the electrons flow from the rough Au layer to the TiO_2 layer and then to the electrolyte; the photon energy (3.1 – 1.4 eV for the wavelength 400 – 900 nm) is lower than the TiO_2 bandgap (~ 3.2 eV) and thus the photo-generated electrons have to result from the plasmonic resonance of Au nanostructures of the rough Au films. The contribution of hot electrons to photocurrent has been extensively used in the TiO_2 films sensitized by the AuNPs,[180,181] it is reasonable to apply the similar mechanism to the rough Au films of this work.

The incident photons to current conversion efficiency (IPCE) expresses the number of electrons per unit number of incident photons at a given irradiation wavelength. Figure 5.7(c) displays the photocurrent vs. wavelength curves, which are measured by using the bandpass filters (bandwidth 20 nm, central wavelengths at 425, 450, 475, 500, 520, 550, 600 and 650 nm, respectively). For all the four TiO_2-based samples, the photocurrent peaks appear at 450 nm. Figure 5.7(d) plots the IPCE vs. wavelength curves that are calculated from the PEC data in Figure 5.7(c) according to the formula

$$\mathrm{IPCE}(\%) = \frac{1240 \times I_{sc}}{\lambda \times P_{light}} \times 100 , \qquad (5.1)$$

where λ is the wavelength of the incident light, P_{light} is the illumination power density at the specific wavelength and I_{sc} is the measured short circuit photocurrent density at the specific wavelength. It is seen that the IPCE value drops quickly in 424 – 475 nm and then becomes flat at longer wavelengths. Nevertheless, the use of Au NPs or Au film leads to an increase of IPCE over the wide visible range, and the AuNP/TiO_2-Au film presents the highest IPCE, which is consistent with the absorption spectra. At wavelengths shorter than 550 nm, the AuNP/TiO_2-Au film presents much higher IPCE values compared to the AuNP/TiO_2 film photoelectrode, indicating that the high IPCE is mainly attributed to the presence of the rough Au film rather than Au NPs.

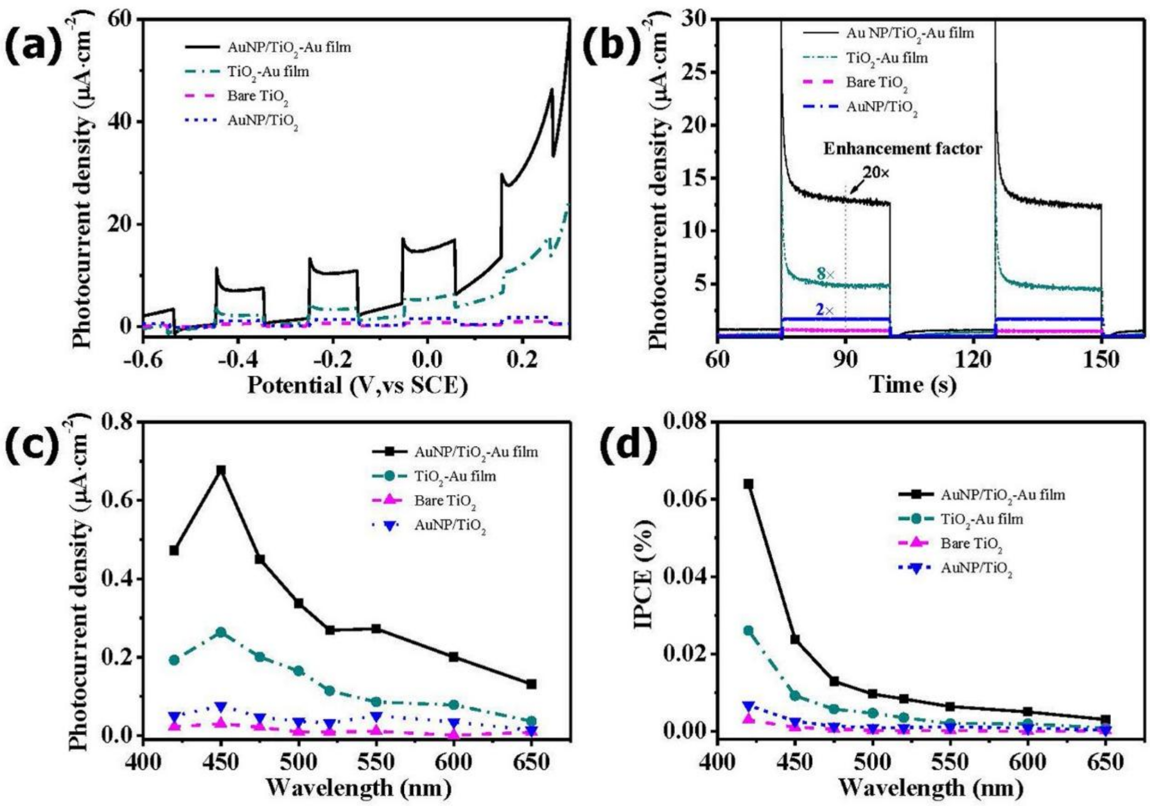

Figure 5.7 Comparisons of the photoelectrochemical properties of the four film samples. (a) Chopped *I-V* curves and (b) *I-t* plots under the irradiation of the UV cut-off solar light (with only λ > 400 nm). The photoelectrodes are measured versus the saturated calomel

electrode (SCE) in the 1-M KOH solution. (c) Photocurrent action spectra and (d) the deduced IPCE spectra. In (b) – (d), the bias potential is kept at 0 V.

5.3.5 Numerical simulation

Finite-difference time-domain (FDTD) simulations are carried out to calculate the absorption spectra of the AuNP/TiO_2-Au film using a commercial software package, Lumerical FDTD Solutions.[186,187] Here, we investigate the electromagnetic response of the AuNP/TiO_2-Au film under visible light and then compare it with the measured spectrum. The perspective view of the structure and the cross-sectional view in the *xz* plane (y = 0) are showed in Figure 5.8(a) and 5.8(b), respectively. In the simulation, the physical structures, from bottom to top, are represented by five layers: *Layer A*, a continuous Au layer at the bottom (200 nm thick); *Layer B*, a layer of random Au particles (represented by 3,000 AuNPs with the size randomly distributed in 20 – 40 nm); *Layer C*, a TiO_2 layer (150 nm thick); *Layer D*, a TiO_2-Au particle composite (800 random TiO_2 particles in 40 – 60 nm); and *Layer E*, another layer of Au nanoparticles (300 AuNPs in 20 – 100 nm). These layers are chosen to resemble the real structures of the AuNP/TiO_2-Au film (see Figure 5.4(a)) as much as possible but using only simple structures like films and nanospheres. More details of simulation are described in Section 5.2.3.

Figure 5.8(c) plots the simulated absorption spectrum of the AuNP/TiO_2-Au film. It resembles closely the shape of measured spectrum over the whole range of 400 – 900 nm. Particularly, the positions of the absorption peak and two valleys given by the simulation align well with those by the experiment. Nevertheless, the simulation shows higher absorption coefficient at the peak than the experiment, which is probably ascribed to the imperfections of using the five simple layers to represent the real structure.

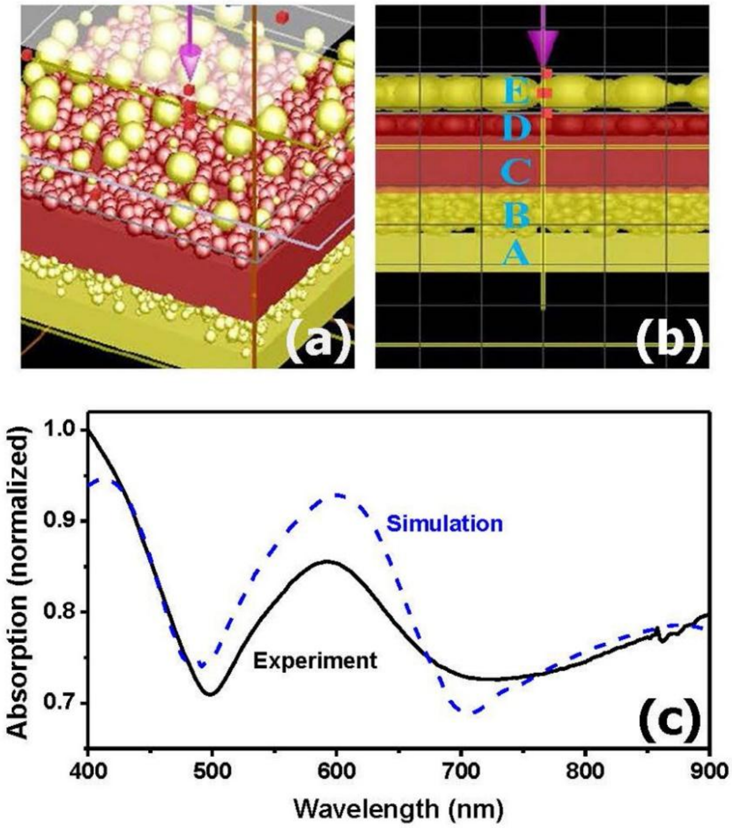

Figure 5.8 FDTD simulation. (a) Perspective view of the representative structure of black absorber for simulation. (b) Cross-sectional view in the *xz* plane. (c) Simulated absorption spectrum (blue dashed line) matches approximately the experimentally measured spectrum (black line).

The field enhancement is further confirmed by the 3D FDTD software. From the simulation curve in Figure 5.8(c), the absorption reaches the minimum at 500 nm (77%) and 700 nm (70%), and the maximum at 410 nm (97%) and 600 nm (95%). Therefore, the wavelengths of 410, 500, 600, 700, 800 and 900 nm are chosen as the working wavelengths to simulate the electric field intensity distribution in the *xz* plane. As shown in Figure 5.9(a), the electric field intensity is enhanced in two random Au particle layers, Layer B and E, though Layer E has a greater enhancement. In Figure 5.9(b) and 5.9(d) that have λ = 500 nm and 700 nm, the electric fields in Layer E are reduced, showing a low contribution from the AuNPs. This corresponds to the absorption valleys at 500 nm and 700 nm in Figure 5.8(c). In Figure 5.9(c) that has λ = 600 nm, the electric field in Layer E becomes apparent again, indicating a strong absorption of the AuNPs due to the LSPR effect. This corresponds to the absorption peak at 600 nm in Figure 5.8(c). In Figure 5.9(e) and 5.9(f), only Layer B shows strong electric field. Based on Figure 5.9(a)-(f), it can be observed that the rough Au layer (Layer B) always has intense electric field and becomes dominant when the wavelength is apart from the plasmonic resonant wavelength of AuNPs (λ = 600 nm). This proves that the rough Au surface always has strong plasmonic absorption over 400 – 900 nm and the AuNPs mainly contribute to the LSPR absorption at 600 nm. In the other word, the blackbody-like absorption is a combination of the plasmonic absorptions of the rough Au layer and the AuNPs.

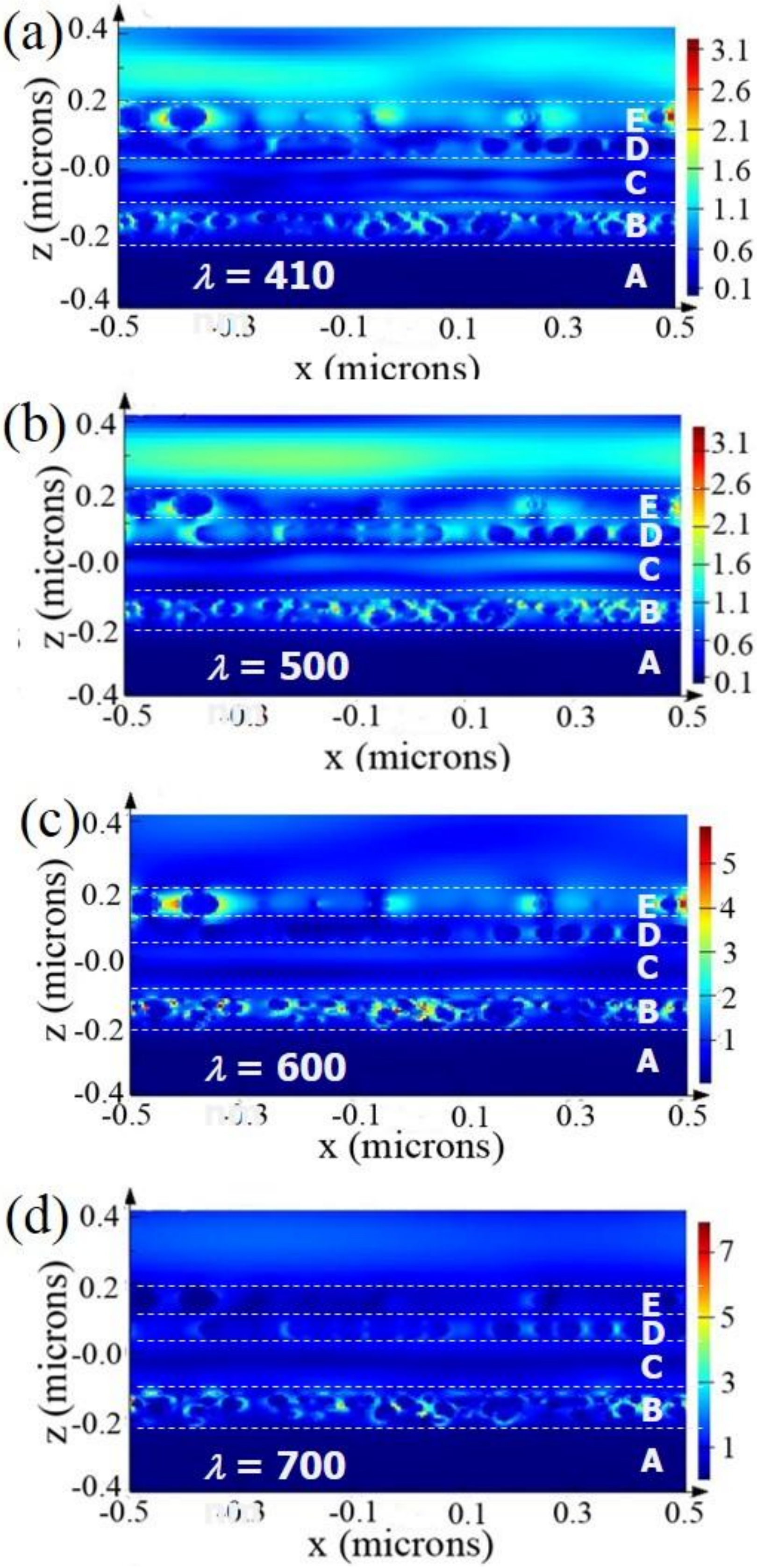
(a)
z (microns)
x (microns)
λ = 410
A
B
C
D
E
(b)
λ = 500
(c)
λ = 600
(d)
λ = 700

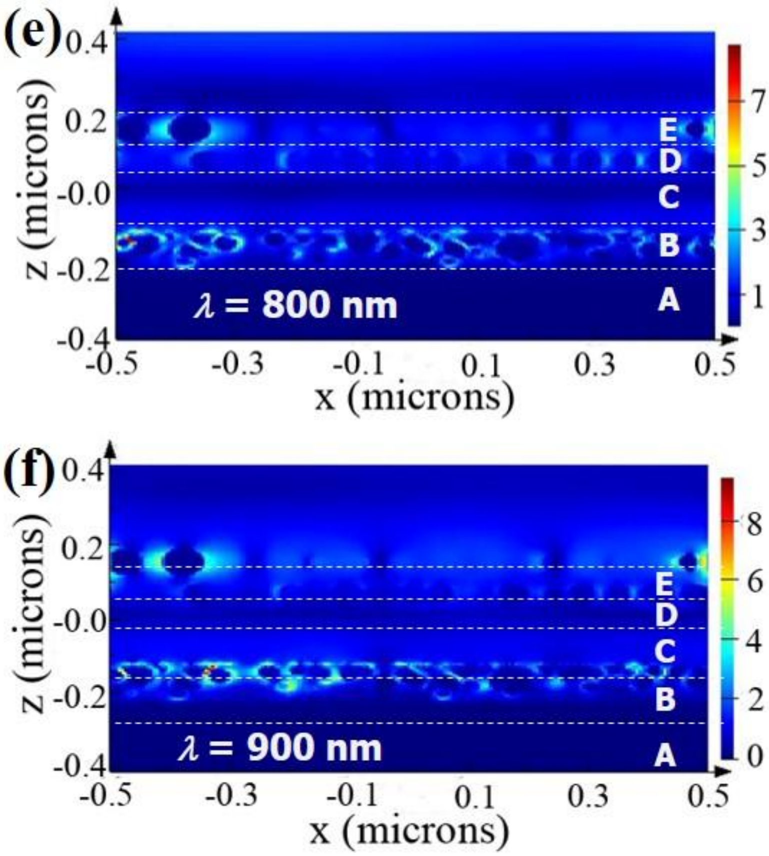

Figure 5.9 Distributions of electric field intensity for the perfect structure in the *xz* plane at six selected wavelengths: (a) 410 nm, (b) 500 nm, (c) 600 nm, (d) 700 nm, (e) 800 nm, and (f) 900 nm. The rough Au layer (i.e., Layer B) has always strong plasmonic resonance at different wavelengths and becomes the dominant absorber when the wavelength is longer than the plasmonic resonance wavelength 600 nm.

5.4 Summary

In summary, an original study on the plasmonic black absorber is demonstrated using the sandwiched structure that comprises a layer of AuNPs, a TiO_2 layer and a rough Au layer. It obtains an excellent absorption over the range of 400 – 900 nm due to the combined plasmonic absorptions of the rough Au layer and the AuNPs as verified by the FDTD simulation. By transferring hot electrons to the TiO_2 layer, the black absorber is able to enhance the photocurrent by 20 folds as compared to the bare TiO_2 under the UV cut-off solar light (> 400 nm). Such an absorber is simple, easy to fabricate and superior to other plasmonic materials. Its broadband strong absorption of the visible and near infrared light is particularly favorable for the photocatalysis using sunlight and would find potential applications in water splitting, environmental remediation and photosynthesis.

CHAPTER 6

CONCLUSIONS AND FUTURE WORK

6.1 Conclusions

The ability to construct plasmonic absorbers that are optically thick but physically very thin could revolutionize high-efficiency photocatalysis device designs. This becomes possible through light trapping in noble metal NPs, or by light coupling into surface plasmon polaritons and photonic modes which propagate in the plane of the semiconductor layer. In this way, extremely thin absorber layers (tens to hundreds of nanometers thick) may absorber the whole visible light. In addition, the utilization of thin absorber layers also avoids some problems of materials scarcity for compound semiconductors.

In this thesis, we have realized the broadband plasmonic absorbers for enhanced photocurrent in visible light range. The great advantages of the broadband plasmonic photocatalysis may encourage the studies of photocatalytic processes based on plasmon such as degradation of methyl blue and heavy metal ions, water splitting and air purification. As mentioned above, the plasmon resonance energy strongly depends on the particle size and the thickness of TiO_2, therefore, the photocatalytic properties of semiconductors can be adjusted and improved by the design of nanoparticles with favorable size or TiO_2 film thickness.

In our first design, a series of TiO_2-Au film hybrids with different TiO_2 thicknesses are fabricated by the ALD method. The design and fabrication can be seen in Chapter 4. Firstly, the structure of TiO_2-Au film hybrids reveals superior absorption and photocatalytic activity as compared to the bare TiO_2 film and the Au film, which result from the LSPR and coupling effects of the random Au nanostructures in the rough Au film for the strong visible absorption and also from the Schottky junction in the Au/TiO_2 interface for the separation of photogenerated electrons and holes. The influence of the TiO_2 thickness is further investigated by controlling the deposition time. The optimal thickness of TiO_2 film for the TiO_2-Au bilayer turns out to be 30 nm. Thicker or thinner TiO_2 film would deteriorate the effects of index matching and optical coupling. However, this device has the problems of complex fabrication and is not suitable for large-scale fabrication. In addition, the TiO_2 film is contacted directly with the electrolyte, which may not be profitable for electron transport.

To optimize the structure of absorber, anther novel structure of Au NPs/TiO_2-Au film nanostructure is introduced by the sol-gel method so as to realize broadband plasmonic absorption. The plasmonic effect of neighboring Au NPs and Au film are utilized, as well as the reflection property of Au film. As a result, TiO_2 itself is modified to spread light absorption to the visible region by doping it with the plasmonic noble metal NPs and films to boost the localized electric field intensity. The developed new plasmonic absorber presents an excellent absorption over the whole visible spectrum. Its fabrication technique is cost-effective and suitable for large-area films. In addition, the small thickness of the whole film and its potential to obtain broadband absorption make it an excellent candidate for the solar absorber and/or anti-reflector coatings.

6.2 Future work

The present thesis focuses on two structures with strong absorption and enhanced photocurrent, TiO_2-Au bilayer using ALD method and Au NPs/TiO_2-Au film nanostructures using sol-gel method. It involves the fabrication of microstructures and the investigation of photocatalysis mechanism. Fortunately, both of these two structures exhibit visible-light absorption around 80% and generate enhanced photocurrent to about 15 $\mu A \cdot cm^{-2}$. A severe problem is the noble metals are still expensive and rare for large-scale applications. Besides, photo-corrosion could cause a gradual release of the noble metal into the solution, which is undesirable in water purification.

However, the separation rate of the photo-excited electrons and holes is still lower than their generated rate, which leaves an ample room to increase the photocurrent. For the fabricated structure in both Chapter 4 and 5, there are obvious transient photocurrent when the light on and off. The sharp increase and decrease of the photocurrent indicate recombination of abundant electron and hole carriers. New designs could be introduced to overcome these disadvantage by adding a hole collector layer (such as NiO_2) to the TiO_2 layer or electron sacrificial agent to the electrolyte, both of which may bring a better electron-hole separation.

On the other hand, compared to the TiO_2 nanoparticles, TiO_2 in other shapes such as nanotube or nanoballs can provide more reaction sites due to the larger specific surface area, which is benefit for highly efficient photocatalysis. Therefore, the substitution of TiO_2 film with TiO_2 nanotubes or nanoballs in TiO_2-Au bilayer and Au NPs/TiO_2-Au film nanostructures may provide preferable structure for photocatalysis.

Besides, the enhancement of the photocatalytic efficiency has not been investigated thoroughly in the present work. Actually, some studies have already tried for water splitting, CO_2 reduction, degradation of methyl orange, but most are on the infant stage. There are still a lot more to explore. The mentioned TiO_2-Au bilayer and Au NPs/TiO_2-Au film nanostructures deserve further develop in many photocatalysis fields.

Beyond this, new plasmonic photocatalyst materials with better performance and lower cost are still at the top of the ‘wanted’ list. In the long run, the material cost will be a limiting factor even if the noble metal-based plasmonic photocatalysis achieves high efficiency and good stability under sunlight irradiation. Other metals that are relatively cheap and abundant such as Al and Cu may be useful. Plasmonic resonance of these metals has been experimentally observed in the UV and visible regions but their uses for photocatalysis are yet to be demonstrated, which may be an uncharted field for plasmonic photocatalysis.

The proposed nanostructures based on rough Au film in this thesis exhibit excellent absorption and enhanced photocurrent response, which indicates high potential to be the optical photocatalysts under visible range. However, the photocatalysis efficiency and relative high cost limit its practical applications. Therefore, it is necessary to develop its applications for efficient photocatalysis and cut down the cost for large-scale industrial production.

REFERENCE

(1) Postel, S. L.; Daily, G. C.; Ehrlich, P. R. Human Appropriation of Renewable Fresh Water. *Science*. 1996, 785–788.

(2) Hillie, T.; Hlophe, M. Nanotechnology and the Challenge of Clean Water. *Nature Nanotechnology* **2007**, *2* (11), 663–664.

(3) Sayigh, A. Renewable Energy - the Way Forward. *Applied Energy* **1999**, *64*, 15–30.

(4) Pimentel, D.; Herz, M.; Glickstein, M.; Zimmerman, M.; Allen, R.; Becker, K.; Evans, J.; Hussan, B.; Sarsfeld, R.; Grosfeld, A.; et al. Renewable Energy : Current and Potential Issues. *BioScience* **2002**, *52* (12), 1111–1120.

(5) Shannon, M. a; Bohn, P. W.; Elimelech, M.; Georgiadis, J. G.; Mariñas, B. J.; Mayes, A. M. Science and Technology for Water Purification in the Coming Decades. *Nature* **2008**, *452* (7185), 301–310.

(6) Carson, R. T.; Mitchell, R. C. The Value of Clean Water: The Public's Willingness to Pay for Boatable, Fishable, and Swimmable Quality Water. *Water Resources Research* **1993**, *29* (7), 2445–2454.

(7) Turner, J. A.; Turner, J. A. A Realizable Renewable Energy Future. *Science* ***1999***, *687* (285), 687-689.

(8) Bang, H.; Ellinger, A. E.; Hadjimarcou, J.; Traichal, P. a. Consumer Concern,

Knowledge, Belief, and Attitude toward Renewable Energy: An Application of the Reasoned Action Theory. *Psychology & Marketing* **2000**, *17* (6), 449–468.

(9) Crabtree, G. W.; Dresselhaus, M. S.; Buchanan, M. V. If the Fuel Cell Is to Become the Modern Steam Engine , Basic. *Physics Today* **2004**,12 (57), 39–45.

(10) Navarro, R. M.; Pena, M. A.; Fierro, J. L. G. Hydrogen Production Reactions from Carbon Feedstocks: Fossils Fuels and Biomass. *Chemical Reviews* **2007**, *107* (10), 3952–3991.

(11) Muradov, N. Z.; Veziroğlu, T. N. “Green” Path from Fossil-Based to Hydrogen Economy: An Overview of Carbon-Neutral Technologies. *International Journal of Hydrogen Energy* **2008**, *33* (23), 6804–6839.

(12) Ni, M.; Leung, M. K. H.; Leung, D. Y. C.; Sumathy, K. A Review and Recent Developments in Photocatalytic Water-Splitting Using TiO2 for Hydrogen Production. *Renewable and Sustainable Energy Reviews* **2007**, *11* (3), 401–425.

(13) Yang, H.; Wei, Z.; Chengzhi, L. Optimal Design and Techno-Economic Analysis of a Hybrid Solar-Wind Power Generation System. *Applied Energy* **2009**, *86* (2), 163–169.

(14) Ollis, D. F. Photocatalytic Purification and Remediation of Contaminated Air and Water. *Comptes Rendus de l’Académie des Sciences - Series IIC - Chemistry* **2000**, *3* (6), 405–411.

(15) Hoffmann, M. R.; Hoffmann, M. R.; Martin, S. T.; Martin, S. T.; Choi, W.; Choi,

W.; Bahnemannt, D. W.; Bahnemannt, D. W. Environmental Applications of Semiconductor Photocatalysis. *Chemical Reviews* **1995**, *95* (1), 69–96.

(16) Miichi, T.; Hayashi, N.; Ihara, S.; Satoh, S.; Yamabe, C. Generation of Radicals Using Discharge inside Bubbles in Water for Water Treatment. *Ozone: Science & Engineering* **2002**, *24* (6), 471–477.

(17) Bahnemann, D. Photocatalytic Water Treatment: Solar Energy Applications. *Solar Energy* **2004**, *77* (5), 445–459.

(18) Bolton, J. R. Solar Photoproduction of Hydrogen: A Review. *Solar Energy* **1996**, *57* (1), 37–50.

(19) van de Krol, R.; Liang, Y.; Schoonman, J.; Krol, R. Van De; Liang, Y.; Schoonman, J. Solar Hydrogen Production with Nanostructured Metal Oxides. *Journal of Materials Chemistry* **2008**, *18* (20), 2311.

(20) Fujishima, a; Honda, K. Electrochemical Photolysis of Water at a Semiconductor Electrode. *Nature* **1972**, *238* (5358), 37–38.

(21) Legrini, O.; Oliveros, E.; Braun, A. M. Photochemical Processes for Water Treatment. *Chemical Reviews* **1993**, *93* (2), 671–698.

(22) Chen, X.; Shen, S.; Guo, L.; Mao, S. S. Semiconductor-Based Photocatalytic Hydrogen Generation. *Chemical Reviews* **2010**, *110* (11), 6503–6570.

(23) Bard, A. J.; Fox, M. A. Artificial Photosynthesis: Solar Splitting of Water to Hydrogen and Oxygen Water Splitting. *Accouts of Chemical Research* **1995**,

28(3), 141–145.

(24) Maeda, K.; Teramura, K.; Lu, D.; Takata, T.; Saito, N.; Inoue, Y.; Domen, K. Photocatalyst Releasing Hydrogen from Water. *Nature* **2006**, *440* (7082), 295–295.

(25) Kudo, A.; Miseki, Y. Heterogeneous Photocatalyst Materials for Water Splitting. *Chemical Society reviews* **2009**, *38* (1), 253–278.

(26) Nakata, K.; Fujishima, A. TiO_2 Photocatalysis: Design and Applications. *Journal of Photochemistry and Photobiology C: Photochemistry Reviews* **2012**, *13* (3), 169–189.

(27) Fox, M. A.; Dulay, M. T. Heterogeneous Photocatalysis. *Chemical Reviews* **1993**, *93* (1), 341–357.

(28) Mills, A.; Davies, R. H.; Worsley, D. Water Purification by Semiconductor Photocatalysis. *Chemical Society Reviews* **1993**, *22* (6), 417.

(29) Henderson, M. A. A Surface Science Perspective on TiO_2 Photocatalysis. *Surface Science Reports* **2011**, *66* (6-7), 185–297.

(30) Sakthivel, S.; Neppolian, B.; Shankar, M. V; Arabindoo, B.; Palanichamy, M.; Murugesan, V. Solar photocatalytic degradation of azo dye: comparison of photocatalytic efficiency of ZnO and TiO_2. **2003**, *77* (3), 65–82.

(31) Yu, J.; Yu, X. Hydrothermal Synthesis and Photocatalytic Activity of Zinc Oxide Hollow Spheres. *Environmental science & technology* **2008**, *42* (13), 4902–4907.

(32) Kumar, S. G.; Devi, L. G. Review on Modified TiO_2 Photocatalysis under UV/visible Light: Selected Results and Related Mechanisms on Interfacial Charge Carrier Transfer Dynamics. *Journal of Physical Chemistry A* **2011**, *115* (46), 13211–13241.

(33) Liu, Z. W.; Hou, W. B.; Pavaskar, P.; Aykol, M.; Cronin, S. B. Plasmon Resonant Enhancement of Photocatalytic Water Splitting Under Visible Illumination. *Nano Letters* **2011**, *11* (3), 1111–1116.

(34) Li, D.; Haneda, H.; Labhsetwar, N. K.; Hishita, S.; Ohashi, N. Visible-Light-Driven Photocatalysis on Fluorine-Doped TiO 2 Powders by the Creation of Surface Oxygen Vacancies. *Chemical Physics Letters* **2005**, *401* (4-6), 579–584.

(35) Yoon, T. P.; Ischay, M. a; Du, J. Visible Light Photocatalysis as a Greener Approach to Photochemical Synthesis. *Nature chemistry* **2010**, *2* (7), 527–532.

(36) Anpo, M.; Takeuchi, M. The Design and Development of Highly Reactive Titanium Oxide Photocatalysts Operating under Visible Light Irradiation. *Journal of Catalysis* **2003**, *216* (1-2), 505–516.

(37) Dutta, S.; Parsons, S. A.; Bhattacharjee, C.; Bandhyopadhyay, S.; Datta, S. Development of an Artificial Neural Network Model for Adsorption and Photocatalysis of Reactive Dye on TiO_2 Surface. *Expert Systems with Applications* **2010**, *37* (12), 8634–8638.

(38) Vinodgopal, K.; Kamat, P. V. Electrochemically Assisted Photocatalysis Using

Nanocrystalline Semiconductor Thin Films. *Solar Energy Materials and Solar Cells* **1995**, *38* (1-4), 401–410.

(39) Farré, M. J.; Franch, M. I.; Malato, S.; Ayllón, J. A.; Peral, J.; Doménech, X. Degradation of Some Biorecalcitrant Pesticides by Homogeneous and Heterogeneous Photocatalytic Ozonation. *Chemosphere* **2005**, *58* (8), 1127–1133.

(40) Ciesia, P.; Kocot, P.; Mytych, P.; Stasicka, Z. Homogeneous Photocatalysis by Transition Metal Complexes in the Environment. *Journal of Molecular Catalysis A: Chemical* **2004**, *224* (1-2), 17–33.

(41) Herrmann, J.-M.; Guillard, C.; Pichat, P. Heterogeneous Photocatalysis : An Emerging Technology for Water Treatment. *Catalysis Today* **1993**, *17* (1-2), 7–20.

(42) Frank, S. N.; Bard, A. J. Heterogeneous Photocatalytic Oxidation of Cyanide Ion in Aqueous Solutions at TiO2 Powder. *Journal of the American Chemical Society* **1977**, *99* (1), 303–304.

(43) Fujishima, A.; Zhang, X. Titanium Dioxide Photocatalysis: Present Situation and Future Approaches. *Comptes Rendus Chimie* **2006**, *9* (5-6), 750–760.

(44) Chong, M. N.; Jin, B.; Chow, C. W. K.; Saint, C. Recent Developments in Photocatalytic Water Treatment Technology: A Review. *Water Research* **2010**, *44* (10), 2997–3027.

(45) Bao, N.; Shen, L.; Takata, T.; Domen, K. Self-Templated Synthesis of Nanoporous CdS Nanostructures for Highly Efficient Photocatalytic Hydrogen Production under Visible Light. *Chemistry of Materials* **2008**, 20(1), 110–117.

(46) Hoffman, A.; Mills, G. Q-Sized Cadmium Sulfide: Synthesis, Characterization, and Efficiency of Photoinitiation of Polymerization of Several Vinylic Monomers. *The Journal of Physical Chemical* **1992**, *5552* (26), 5546–5552.

(47) Li, Q.; Guo, B.; Yu, J.; Ran, J.; Zhang, B.; Yan, H.; Gong, J. R. Highly Efficient Visible-Light-Driven Photocatalytic Hydrogen Production of CdS-Cluster-Decorated Graphene Nanosheets. *Journal of the American Chemical Society* **2011**, *133* (28), 10878–10884.

(48) Zhang, X.; Chen, Y. L.; Liu, R.-S.; Tsai, D. P. Plasmonic Photocatalysis. *Reports on progress in physics. Physical Society* **2013**, *76*, 046401.

(49) Serpone, N. Is the Band Gap of Pristine TiO2 Narrowed by Anion- and Cation-Doping of Titanium Dioxide in Second-Generation Photocatalysts? *Journal of Physical Chemistry B* **2006**, *110* (48), 24287–24293.

(50) Vinodgopal, K.; Kamat, P. V. Enhanced Rates of Photocatalytic Degradation of an Azo Dye Using SnO_2/TiO_2 Coupled Semiconductor Thin Films. *Environmental Science and Technology* **1995**, *29* (3), 841–845.

(51) Zhang, M.; Chen, C.; Ma, W.; Zhao, J. Visible-Light-Induced Aerobic Oxidation of Alcohols in a Coupled Photocatalytic System of Dye-Sensitized TiO2 and

TEMPO. *Angewandte Chemie - International Edition* **2008**, *47* (50), 9730–9733.

(52) Pelaez, M.; Nolan, N. T.; Pillai, S. C.; Seery, M. K.; Falaras, P.; Kontos, A. G.; Dunlop, P. S. M.; Hamilton, J. W. J.; Byrne, J. A.; O'Shea, K.; et al. A Review on the Visible Light Active Titanium Dioxide Photocatalysts for Environmental Applications. *Applied Catalysis B: Environmental* **2012**, *125*, 331–349.

(53) Abe, R.; Sayama, K.; Arakawa, H. Efficient Hydrogen Evolution from Aqueous Mixture of I- and Acetonitrile Using a Merocyanine Dye-Sensitized Pt/TiO_2 Photocatalyst under Visible Light Irradiation. *Chemical Physics Letters* **2002**, *362*, 441–444.

(54) Zaleska, A. Doped-TiO_2 : A Review. *Recent Patents on Engineering 2008*, *2*(3), 157–164.

(55) Li, D.; Haneda, H.; Hishita, S.; Ohashi, N. Visible-Light-Driven N−F−Codoped TiO_2 Photocatalysts. 2. Optical Characterization, Photocatalysis, and Potential Application to Air Purification. *Chemistry of Materials* **2005**, *17* (10), 2596–2602.

(56) Park, J. H.; Kim, S.; Bard, A. J. Novel Carbon-Doped TiO_2 Nanotube Arrays with High Aspect Ratios for Efficient Solar Water Splitting. *Nano Letters* **2006**, *6* (1), 24–28.

(57) Kowalska, E.; Mahaney, O. O. P.; Abe, R.; Ohtani, B. Visible-Light-Induced Photocatalysis through Surface Plasmon Excitation of Gold on Titania Surfaces.

Physical Chemistry Chemical Physics : PCCP **2010**, *12* (10), 2344–2355.

(58) Marcì, G.; Augugliaro, V.; López-Muñoz, M. J.; Martín, C.; Palmisano, L.; Rives, V.; Schiavello, M.; Tilley, R. J. D.; Venezia, A. M. Preparation Characterization and Photocatalytic Activity of Polycrystalline ZnO/TiO_2 Systems. 1. Surface and Bulk Characterization. *The Journal of Physical Chemistry B* **2001**, *105* (5), 1026–1032.

(59) Choi, W.; Termin, A.; Hoffmann, M. R. The Role of Metal Ion Dopants in Quantum-Sized TiO2: Correlation between Photoreactivity and Charge Carrier Recombination Dynamics. *Journal of Physical Chemistry* **1994**, *98* (51), 13669–13679.

(60) Ohno, T.; Tanigawa, F.; Fujihara, K.; Izumi, S.; Matsumura, M. Photocatalytic Oxidation of Water by Visible Light Using Ruthenium-Doped Titanium Dioxide Powder. *Journal of Photochemistry and Photobiology A: Chemistry* **1999**, *127* (1–3), 107–110.

(61) Klosek, S.; Raftery, D. Visible Light Driven V-Doped TiO Photocatalyst and Its Photooxidation of ethanol2. *J. Phys. Chem. B* **2001**, *105*, 2815–2819.

(62) Yang, Y.; Li, X. J.; Chen, J. T.; Wang, L. Y. Effect of Doping Mode on the Photocatalytic Activities of Mo/TiO_2. *Journal of Photochemistry and Photobiology A: Chemistry* **2004**, *163* (3), 517–522.

(63) Zhang, Y.; Zhang, J.; Zhu, Z.; Yan, N.; Liu, Q. Preparation and Properties of

Sliver and Nitrogen Co-Doped TiO_2 Photocatalyst. *Materials Research Bulletin* **2013**, *48* (11), 4872–4876.

(64) Sun, L.; Zhao, X.; Cheng, X.; Sun, H.; Li, P.; Fan, W. Synergistic Effects in La / N Codoped TiO_2 Anatase (101) Surface Correlated with Enhanced Visible-Light Photocatalytic Activity. Langmuir **2012**, 28(13). 5882-91.

(65) Anandan, S.; Ikuma, Y.; Murugesan, V. Highly Active Rare-Earth-Metal La-Doped Photocatalysts: Fabrication, Characterization, and Their Photocatalytic Activity. *International Journal of Photoenergy* **2012**, *2012*.

(66) Ma, Y.; Xing, M.; Zhang, J.; Tian, B.; Chen, F. Synthesis of Well Ordered Mesoporous Yb, N Co-Doped TiO 2 with Superior Visible Photocatalytic Activity. *Microporous and Mesoporous Materials* **2012**, *156*, 145–152.

(67) Spadavecchia, F.; Ceotto, M.; Presti, L. Lo; Aieta, C.; Biraghi, I.; Meroni, D.; Ardizzone, S.; Cappelletti, G. Second Generation Nitrogen Doped Titania Nanoparticles: A Comprehensive Electronic and Microstructural Picture. *Chinese Journal of Chemistry* **2014**, *32* (12), 1195–1213.

(68) Ma, Y.; Zhang, J.; Tian, B.; Chen, F.; Wang, L. Synthesis and Characterization of Thermally Stable Sm,N Co-Doped TiO2 with Highly Visible Light Activity. *Journal of Hazardous Materials* **2010**, *182* (1-3), 386–393.

(69) Zhao, Y.; Liu, J.; Shi, L.; Yuan, S.; Fang, J.; Wang, Z.; Zhang, M. Solvothermal Preparation of Sn^{4+} Doped Anatase TiO_2 Nanocrystals from Peroxo-Metal-

Complex and Their Photocatalytic Activity. *Applied Catalysis B: Environmental* **2011**, *103* (3-4), 436–443.

(70) Yuan, S.; Sheng, Q.; Zhang, J.; Chen, F.; Anpo, M.; Zhang, Q. Synthesis of La3+ Doped Mesoporous Titania with Highly Crystallized Walls. *Microporous and Mesoporous Materials* **2005**, *79* (1-3), 93–99.

(71) Liu, H.; Wu, Y.; Zhang, J. A New Approach toward Carbon Modified Vanadium Doped Titanium Dioxide Photocatalysts. *ACS Applied Materials & Interfaces* **2011**, *3*(5), 1757–1764.

(72) Zuo, F.; Wang, L.; Wu, T.; Zhang, Z.; Borchardt, D.; Feng, P. Self-Doped Ti3+ Enhanced Photocatalyst for Hydrogen Production under Visible Light. *Journal of the American Chemical Society* **2010**, *132* (34), 11856–11857.

(73) Stepanov, A. L. Applications of Ion Implantation for Modification of TiO 2: A Review. *Reviews on Advanced Materials Science* **2012**, *30* (2), 150–165.

(74) Xing, M.; Fang, W.; Nasir, M.; Ma, Y.; Zhang, J.; Anpo, M. Self-Doped Ti3+-Enhanced TiO2 Nanoparticles with a High-Performance Photocatalysis. *Journal of Catalysis* **2013**, *297*, 236–243.

(75) Anpo, M.; Ichihashi, Y.; Takeuchi, M.; Yamashita, H. Design of Unique Titanium Oxide Photocatalysts by an Advanced Metal Ion-Implantation Method and Photocatalytic Reactions under Visible Light Irradiation. *Research on Chemical Intermediates* **1998**, *24* (2), 143–149.

(76) Ghicov, A.; Macak, J. M.; Tsuchiya, H.; Kunze, J.; Haeublein, V.; Frey, L.; Schmuki, P. Ion Implantation and Annealing for an Efficient N-Doping of TiO2 Nanotubes. *Nano Letters* **2006**, *6* (5), 1080–1082.

(77) Herrmann, J. M.; Disdier, J.; Pichat, P. Effect of Chromium Doping on the Electrical and Catalytic Properties of Powder Titania under UV and Visible Illumination. *Chemical Physics Letters* **1984**, *108* (6), 618–622.

(78) Karvinen, S.; Hirva, P.; Pakkanen, T. A. Ab Initio Quantum Chemical Studies of Cluster Models for Doped Anatase and Rutile TiO_2. *Journal of Molecular Structure: THEOCHEM* **2003**, *626*, 271–277.

(79) Sumita, T.; Yamaki, T.; Yamamoto, S.; Miyashita, A. Ion Beam Modification of Photo-Induced Charge Separation in TiO_2 Films. *Nuclear Instruments and Methods in Physics Research, Section B: Beam Interactions with Materials and Atoms* **2003**, *206*(5), 245–248.

(80) Wang, P.; Huang, B.; Dai, Y.; Whangbo, M.-H. Plasmonic Photocatalysts: Harvesting Visible Light with Noble Metal Nanoparticles. *Physical Chemistry Chemical Physics* **2012**, *14* (28), 9813.

(81) Macyk, W.; Burgeth, G.; Kisch, H. Photoelectrochemical Properties of Platinum(iv) Chloride Surface Modified TiO_2 Dedicated to Professor Jean Kossanyi on the Occasion of His 70th Birthday. *Photochem. Photobiol. Sci.* **2003**, *2* (3), 322–328.

(82) Burgeth, G.; Kisch, H. Photocatalytic and Photoelectrochemical Properties of titania–chloroplatinate(IV). *Coordination Chemistry Reviews* **2002**, *230* (1-2), 41–47.

(83) Lee, J.; Mubeen, S.; Ji, X.; Stucky, G. D.; Moskovits, M. Plasmonic Photoanodes for Solar Water Splitting with Visible Light. *Nano Letters* **2012**, *12* (9), 5014–5019.

(84) Linic, S.; Christopher, P.; Ingram, D. B. Plasmonic-Metal Nanostructures for Efficient Conversion of Solar to Chemical Energy. *Nature Materials* **2011**, *10* (12), 911–921.

(85) Kowalska, E.; Remita, H.; Colbeau-Justin, C.; Hupka, J.; Belloni, J. Modification of Titanium Dioxide with Platinum Ions and Clusters: Application in Photocatalysis. *Journal of Physical Chemistry C* **2008**, *112* (4), 1124–1131.

(86) Primo, A.; Corma, A.; García, H. Titania Supported Gold Nanoparticles as Photocatalyst. *Physical Chemistry Chemical Physics : PCCP* **2011**, *13*, 886–910.

(87) Hashimoto, K.; Irie, H.; Fujishima, A. A Historical Overview and Future Prospects. *AAPPS Bulletin* **2007**, *17* (6), 12–28.

(88) Kelly, K. L.; Kelly, K. L.; Coronado, E.; Zhao, L.; Coronado, E.; Schatz, G. C.; Zhao, L. L.; Schatz, G. C. The Optical Properties of Metal Nanoparticles: The Influence of Size, Shape, and Dielectric Environment. *Journal of Physical Chemistry B* **2003**, *107* (3), 668–677.

(89) Li, H.; Bian, Z.; Zhu, J.; Huo, Y.; Li, H.; Lu, Y. Mesoporous Au/TiO_2 Nanocomposites with Enhanced Photocatalytic Activity. *Journal of the American Chemical Society* **2007**, *129* (15), 4538–4539.

(90) Murdoch, M.; Waterhouse, G. I. N.; Nadeem, M. A.; Metson, J. B.; Keane, M. A.; Howe, R. F.; Llorca, J.; Idriss, H. The Effect of Gold Loading and Particle Size on Photocatalytic Hydrogen Production from Ethanol over Au/TiO_2 Nanoparticles. *Nature chemistry* **2011**, *3* (6), 489–492.

(91) Tian, Y.; Tatsuma, T. Mechanisms and Applications of Plasmon-Induced Charge Separation at TiO 2Films Loaded with Gold Nanoparticles. *J. Am. Chem. Soc.* **2005**, *127* (16), 7632–7637.

(92) Liu, Z. W.; Hou, W. B.; Pavaskar, P.; Aykol, M.; Cronin, S. B. Plasmon Resonant Enhancement of Photocatalytic Water Splitting Under Visible Illumination. *Nano Letters* **2011**, *11* (3), 1111–1116.

(93) Gomes Silva, C.; Juárez, R.; Marino, T.; Molinari, R.; García, H. Influence of Excitation Wavelength (UV or Visible Light) on the Photocatalytic Activity of Titania Containing Gold Nanoparticles for the Generation of Hydrogen or Oxygen from Water. *Journal of the American Chemical Society* **2011**, *133* (3), 595–602.

(94) Dawson, A.; Kamat, P. V. Complexation of Gold Nanoparticles with Radiolytically Generated Thiocyanate Radicals ((SCN)2•-). *Journal of*

Physical Chemistry B **2000**, *104* (50), 11842–11846.

(95) Fujishima, a; Zhang, X.; Tryk, D. TiO2 Photocatalysis and Related Surface Phenomena. *Surface Science Reports* **2008**, *63* (12), 515–582.

(96) Pang, C. L.; Lindsay, R.; Thornton, G. Structure of Clean and Adsorbate-Covered Single-Crystal Rutile TiO 2 Surfaces. *Chemical Reviews* **2013**, *113* (6), 3887–3948.

(97) Lana Villarreal, T.; Gómez, R.; Neumann-Spallart, M.; Alonso-Vante, N.; Salvador, P. Semiconductor Photooxidation of Pollutants Dissolved in Water: A Kinetic Model for Distinguishing between Direct and Indirect Interfacial Hole Transfer. I. Photoelectrochemical Experiments with Polycrystalline Anatase Electrodes under Current Doubling and. *Journal of Physical Chemistry B* **2004**, *108* (39), 15172–15181.

(98) Wang, P.; Huang, B.; Dai, Y.; Whangbo, M.-H. Plasmonic Photocatalysts: Harvesting Visible Light with Noble Metal Nanoparticles. *Phys. Chem. Chem. Phys.* **2012**, *14* (28), 9813–9825.

(99) Lee, K.; El-sayed, M. a. Gold and Silver Nanoparticles in Sensing and Imaging : Sensitivity of Plasmon Response to Size , Shape , and Metal Composition Gold and Silver Nanoparticles in Sensing and Imaging : Sensitivity of Plasmon Response to Size , Shape , and Metal Composition. *Journal of Physical Chemistry B* **2006**, 19220–19225.

(100) Xia, Y.; Halas, N. J. Shape-Controlled Synthesis and Surface Plasmonic Properties of Metallic Nanostructures. *MRS Bulletin* **2011**, *30* (05), 338–348.

(101) Haynes, C. L.; Haynes, C. L.; McFarland, a. D.; Zhao, L.; McFarland, A. D.; Zhao, L.; Van Duyne, R. P.; Van Duyne, R. P.; Schatz, G. C.; Schatz, G. C.; et al. Nanoparticle Optics: The Importance of Radiative Dipole Coupling in Two-Dimensional Nanoparticle Arrays. *Journal of Physical Chemistry B* **2003**, *107* (30), 7337–7342.

(102) Hicks, E. M.; Zou, S.; Schatz, G. C.; Spears, K. G.; Van Duyne, R. P.; Gunnarsson, L.; Rindzevicius, T.; Kasemo, B.; Käll, M. Controlling Plasmon Line Shapes through Diffractive Coupling in Linear Arrays of Cylindrical Nanoparticles Fabricated by Electron Beam Lithography. *Nano Letters* **2005**, *5* (6), 1065–1070.

(103) Chung, T.; Lee, S. Y.; Song, E. Y.; Chun, H.; Lee, B. Plasmonic Nanostructures for Nano-Scale Bio-Sensing. *Sensors* **2011**, *11* (11), 10907–10929.

(104) Mock, J. J.; Barbic, M.; Smith, D. R.; Schultz, D. a.; Schultz, S. Shape Effects in Plasmon Resonance of Individual Colloidal Silver Nanoparticles. *Journal of Chemical Physics* **2002**, *116* (15), 6755–6759.

(105) Mock, J. J.; Barbic, M.; Smith, D. R.; Schultz, D. A.; Schultz, S. Shape Effects in Plasmon Resonance of Individual Colloidal Silver Nanoparticles. *Journal of Chemical Physics* **2002**, *116* (15), 6755–6759.

(106) Huang, X.; El-Sayed, I. H.; Qian, W.; El-Sayed, M. a. Cancer Cell Imaging and Photothermal Therapy in the near-Infrared Region by Using Gold Nanorods. *Journal of the American Chemical Society* **2006**, *128* (6), 2115–2120.

(107) Zhang, P.; Wang, T.; Gong, J. Mechanistic Understanding of the Plasmonic Enhancement for Solar Water Splitting. *Advanced Materials* **2015**, *27* (36), 5328–5342.

(108) Warren, S. C.; Thimsen, E. Plasmonic Solar Water Splitting. *Energy & Environmental Science* **2012**, *5* (1), 5133–5146.

(109) Amrollahi, R.; Hamdy, M. S.; Mul, G. Understanding Promotion of Photocatalytic Activity of TiO_2 by Au Nanoparticles. *Journal of Catalysis* **2014**, *319*, 194–199.

(110) Zhang, J. Z. Biomedical Applications of Shape-Controlled Plasmonic Nanostructures: A Case Study of Hollow Gold Nanospheres for Photothermal Ablation Therapy of Cancer. *Journal of Physical Chemistry Letters* **2010**, *1* (4), 686–695.

(111) Cheng, L.-C.; Huang, J.-H.; Chen, H. M.; Lai, T.-C.; Yang, K.-Y.; Liu, R.-S.; Hsiao, M.; Chen, C.-H.; Her, L.-J.; Tsai, D. P. Seedless, Silver-Induced Synthesis of Star-Shaped Gold/silver Bimetallic Nanoparticles as High Efficiency Photothermal Therapy Reagent. *J. Mater. Chem.* **2012**, *22* (5), 2244.

(112) Chen, J.; Glaus, C.; Laforest, R.; Zhang, Q.; Yang, M.; Gidding, M.; Welch, M.

J.; Xia, Y. Gold Nanocages as Photothermal Transducers for Cancer Treatment. *Small* **2010**, *6* (7), 811–817.

(113) Liu, N.; Mesch, M.; Weiss, T.; Hentschel, M.; Giessen, H. Infrared Perfect Absorber and Its Application as Plasmonic Sensor. *Nano Letters* **2010**, *10*, 2342–2348.

(114) Moreau, A.; Ciracì, C.; Mock, J. J.; Hill, R. T.; Wang, Q.; Wiley, B. J.; Chilkoti, A.; Smith, D. R. Controlled-Reflectance Surfaces with Film-Coupled Colloidal Nanoantennas. *Nature* **2012**, *492*, 86–89.

(115) Søndergaard, T.; Novikov, S. M.; Holmgaard, T.; Eriksen, R. L.; Beermann, J.; Han, Z.; Pedersen, K.; Bozhevolnyi, S. I. Plasmonic Black Gold by Adiabatic Nanofocusing and Absorption of Light in Ultra-Sharp Convex Grooves. *Nature Communications* **2012**, *3*, 969.

(116) Hedayati, M. K.; Javaherirahim, M.; Mozooni, B.; Abdelaziz, R.; Tavassolizadeh, A.; Chakravadhanula, V. S. K.; Zaporojtchenko, V.; Strunkus, T.; Faupel, F.; Elbahri, M. Design of a Perfect Black Absorber at Visible Frequencies Using Plasmonic Metamaterials. *Advanced Materials* **2011**, *23* (45), 5410–5414.

(117) Liu, Z.; Liu, X.; Huang, S.; Pan, P.; Chen, J.; Liu, G.; Gu, G. Automatically Acquired Broadband Plasmonic-Metamaterial Black Absorber during the Metallic Film-Formation. *ACS Appl. Mater. Interfaces* **2015**, 7(8), 4962-4968.

(118) Nazirzadeh, M. A.; Atar, F. B.; Turgut, B. B.; Okyay, A. K. Random Sized Plasmonic Nanoantennas on Silicon for Low-Cost Broad-Band near-Infrared Photodetection. *Scientific Reports* **2014**, *4*, 7103.

(119) Dhawan, A.; Norton, S. J.; Gerhold, M. D.; Vo-Dinh, T. Comparison of FDTD Numerical Computations and Analytical Multipole Expansion Method for Plasmonics-Active Nanosphere Dimers. *Optics express* **2009**, *17* (12), 9688–9703.

(120) Vial, A.; Laroche, T.; Dridi, M.; Le Cunff, L. A New Model of Dispersion for Metals Leading to a More Accurate Modeling of Plasmonic Structures Using the FDTD Method. *Applied Physics A: Materials Science and Processing* **2011**, *103* (3), 849–853.

(121) Stephen D. G.; Introduction to the Finite-Difference Time-Domain Method for electromagnetics. *Synthesis Lectures on Computational Electromagnetics* 2011, *6*(1), 1-250.

(122) Khan, S. U. M.; Al-Shahry, M.; Ingler, W. B. Efficient Photochemical Water Splitting by a Chemically Modified N-TiO2. *Science* **2002**, *297* (5590), 2243–2245.

(123) Fujishima, A.; Rao, T. N.; Tryk, D. a. Titanium Dioxide Photocatalysis. *Journal of Photochemistry and Photobiology C: Photochemistry Reviews* **2000**, *1* (1), 1–21.

(124) Umebayashi, T.; Yamaki, T.; Tanaka, S.; Asai, K. Visible Light-Induced Degradation of Methylene Blue on S-Doped TiO2. *Chemistry Letters* **2003**, *32* (4), 330–331.

(125) Furube, A.; Du, L.; Hara, K.; Katoh, R.; Tachiya, M. Ultrafast Plasmon-Induced Electron Transfer from Gold Nanodots into TiO2 Nanoparticles. *Journal of the American Chemical Society* **2007**, *129* (48), 14852–14853.

(126) Mock, J. J.; Barbic, M.; Smith, D. R.; Schultz, D. a.; Schultz, S. Shape Effects in Plasmon Resonance of Individual Colloidal Silver Nanoparticles. *The Journal of Chemical Physics* **2002**, *116* (15), 6755.

(127) Huang, X.; El-sayed, I. H.; Qian, W.; El-sayed, M. A. Cancer Cell Imaging and Photothermal Therapy in the near-Infrared Region by Using Gold Nanorods. *Journal of the American Chemical Society* **2006**, 3, 2115–2120.

(128) Heo, C.-J.; Kim, S.-H.; Jang, S. G.; Lee, S. Y.; Yang, S.-M. Gold "Nanograils" with Tunable Dipolar Multiple Plasmon Resonances. *Advanced Materials* **2009**, *21* (17), 1726–1731.

(129) Kochuveedu, S.; Kim, D.; Kim, D. Surface-Plasmon-Induced Visible Light Photocatalytic Activity of TiO2 Nanospheres Decorated by Au Nanoparticles with Controlled Configuration. *The Journal of Physical Chemistry C* **2012**, 2500–2506.

(130) Gole, J. L.; Stout, J. D.; Burda, C.; Lou, Y.; Chen, X. Highly Efficient Formation

of Visible Light Tunable $TiO_{2-X}N_X$ Photocatalysts and Their Transformation at the Nanoscale. *The Journal of Physical Chemistry B* **2004**, *108* (4), 1230–1240.

(131) Geometry, C. N.; Hsu, C.; Lien, D.; Lu, S.; Chen, C.; Kang, C.; Chueh, Y. Employing Carbon Nanotube / TiO_2. *ACS nano* **2012**, *6* (8), 6687–6692.

(132) Naldoni, A.; Allieta, M.; Santangelo, S.; Marelli, M.; Fabbri, F.; Cappelli, S.; Bianchi, C. L.; Psaro, R.; Dal Santo, V. Effect of Nature and Location of Defects on Bandgap Narrowing in Black TiO_2 Nanoparticles. *Journal of the American Chemical Society* **2012**, *134* (18), 7600–7603.

(133) Kravets, V. G.; Neubeck, S.; Grigorenko, a. N.; Kravets, a. F. Plasmonic Blackbody: Strong Absorption of Light by Metal Nanoparticles Embedded in a Dielectric Matrix. *Physical Review B - Condensed Matter and Materials Physics* **2010**, *81* (16), 1–9.

(134) Buso, D.; Pacifico, J.; Martucci, A.; Mulvaney, P. Gold-Nanoparticle-Doped TiO2 Semiconductor Thin Films: Optical Characterization. *Advanced Functional Materials* **2007**, *17* (3), 347–354.

(135) Connelly, K.; Wahab, a. K.; Idriss, H. Photoreaction of Au/TiO_2 for Hydrogen Production from Renewables: A Review on the Synergistic Effect between Anatase and Rutile Phases of TiO2. *Mater. Renew. and Sustain. Energy* **2012**, *1* (1), 3.

(136) Wu, X.; Centeno, A.; Zhang, X.; Darvill, D.; Ryan, M. P.; Riley, D. J.; Alford, N.

M.; Xie, F. Broadband Plasmon Photocurrent Generation from Au Nanoparticles/ Mesoporous TiO2 Nanotube Electrodes. *Solar Energy Materials and Solar Cells* **2015**, *138*, 80–85.

(137) Lee, K.-C.; Lin, S.-J.; Lin, C.-H.; Tsai, C.-S.; Lu, Y.-J. Size Effect of Ag Nanoparticles on Surface Plasmon Resonance. *Surface and Coatings Technology* **2008**, *202* (22-23), 5339–5342.

(138) Nazirzadeh, M. A.; Atar, F. B.; Turgut, B. B.; Okyay, A. K. Random Sized Plasmonic Nanoantennas on Silicon for Low-Cost Broad-Band near-Infrared Photodetection. *Scientific Reports* **2014**, *4*, 7103.

(139) Shi, X.; Ueno, K.; Oshikiri, T.; Misawa, H. Improvement of Plasmon-Enhanced Photocurrent Generation by Interference of TiO2 Thin Film. *Journal of Physical Chemistry C* **2013**, *117*, 24733–24739.

(140) Hou, Y.; Li, X.; Zhao, Q.; Quan, X.; Chen, G. TiO_2 nanotube/Ag–AgBr Three-Component Nanojunction for Efficient Photoconversion. *Journal of Materials Chemistry* **2011**, *21* (44), 18067.

(141) Ingram, D. B.; Linic, S. Photoelectrodes : Evidence for Selective Plasmon-Induced Formation. **2011**, 5202–5205.

(142) White, J. R. 2.1. Preparation of Films. **1974**, *22*, 23–35.

(143) Gupta, G.; Tanaka, D.; Ito, Y.; Shibata, D.; Shimojo, M.; Furuya, K.; Mitsui, K.; Kajikawa, K. Absorption Spectroscopy of Gold Nanoisland Films: Optical and

Structural Characterization. *Nanotechnology* **2009**, *20* (2), 025703.

(144) Cheng, H.-E.; Chen, C.-C. Morphological and Photoelectrochemical Properties of ALD TiO2 Films. *Journal of The Electrochemical Society* **2008**, *155* (9), D604.

(145) King, D. M.; Du, X.; Cavanagh, A. S.; Weimer, A. W. Quantum Confinement in Amorphous TiO_2 Films Studied via Atomic Layer Deposition. *Nanotechnology* **2008**, *19* (44), 445401.

(146) Chen, Z.; Fang, L.; Dong, W.; Zheng, F.; Shen, M.; Wang, J. Inverse Opal Structured Ag/TiO_2 Plasmonic Photocatalyst Prepared by Pulsed Current Deposition and Its Enhanced Visible Light Photocatalytic Activity. *Journal of Materials Chemistry A* **2014**, *2* (3), 824.

(147) Liu, L.; Zhao, H.; Andino, J. M.; Li, Y. Photocatalytic CO2 Reduction with H2O on TiO_2 Nanocrystals: Comparison of Anatase, Rutile, and Brookite Polymorphs and Exploration of Surface Chemistry. *ACS Catalysis* **2012**, *2* (8), 1817–1828.

(148) Temnov, V. V.; Armelles, G.; Woggon, U.; Guzatov, D.; Cebollada, A.; Garcia-Martin, A.; Garcia-Martin, J.-M.; Thomay, T.; Leitenstorfer, A.; Bratschitsch, R. Active Magneto-Plasmonics in Hybrid Metal–ferromagnet Structures. *Nature Photonics* **2010**, *4* (2), 107–111.

(149) Cao, S.; Wang, T.; Zhao, J.; Tan, F.; Zhang, X.; Yu, W. Hierarchic Random Nanosphere Model for Broadband Solar Energy Absorbers. *Optical Materials*

Express **2015**, *5* (12), 2777.

(150) Chan, S.-H.; Lin, W.-T.; Cho, W.-H.; Kuo, C.-C.; Lee, C.-C.; Chen, S.-H. Controllable Photonic Mirror Fabricated by the Atomic Layer Deposition on the Nanosphere Template. *Applied optics* **2014**, *53* (4), A237–A241.

(151) Zhang, N.; Liu, K.; Liu, Z.; Song, H.; Zeng, X.; Ji, D.; Cheney, A.; Jiang, S.; Gan, Q. Ultrabroadband Metasurface for Efficient Light Trapping and Localization: A Universal Surface-Enhanced Raman Spectroscopy Substrate for “All” Excitation Wavelengths. *Advanced Materials Interfaces* **2015**, 2, 1500142.

(152) Wang, H. U. I.; Brandl, D. W. Plasmonic Nanostructures : Artificial Molecules Nanoshell Plasmons : The Sphere-Cavity. *Accounts of Chemical Research* **2007**, *40* (1), 53–62.

(153) Liu, E.; Fan, J.; Hu, X.; Hu, Y.; Li, H.; Tang, C.; Sun, L.; Wan, J. A Facile Strategy to Fabricate Plasmonic Au/TiO2 Nano-Grass Films with Overlapping Visible Light-Harvesting Structures for H2 Production from Water. *Journal of Materials Science* **2014**, *50* (5), 2298–2305.

(154) Mora-Seró, I.; Bisquert, J.; Dittrich, T.; Belaidi, a.; Susha, a. S.; Rogach, a. L. Photosensitization of TiO2 Layers with CdSe Quantum Dots: Correlation between Light Absorption and Photoinjection. *Journal of Physical Chemistry C* **2007**, *111* (40), 14889–14892.

(155) Baglio, V.; Girolamo, M.; Antonucci, V.; Aricò, a S. Influence of TiO_2 Film

Thickness on the Electrochemical Behaviour of Dye-Sensitized Solar Cells. *International Journal of Electrochemcal. Science* **2011**, *6*, 3375–3384.

(156) Hou, W.; Cronin, S. B. A Review of Surface Plasmon Resonance-Enhanced Photocatalysis. *Advanced Functional Materials* **2013**, *23* (13), 1612–1619.

(157) Primo, A.; Corma, A.; García, H. Titania Supported Gold Nanoparticles as Photocatalyst. *Physical chemistry chemical physics : PCCP* **2011**, *13* (3), 886–910.

(158) Zhang, X.; Chen, Y. L.; Liu, R.-S.; Tsai, D. P. Plasmonic Photocatalysis. *Reports on progress in physics. Physical Society* **2013**, *76* (4), 046401.

(159) Asahi, R.; Morikawa, T.; Ohwaki, T.; Aoki, K.; Taga, Y. Visible-Light Photocatalysis in Nitrogen-Doped Titanium Oxides. Science **2001**, *293* (7), 269–272.

(160) Irie, H.; Watanabe, Y.; Hashimoto, K. Nitrogen-Concentration Dependence on Photocatalytic Activity of $TiO_{2-X}N_X$ Powders. *The Journal of Physical Chemistry B* **2003**, *107* (23), 5483–5486.

(161) Irie, H.; Watanabe, Y.; Hashimoto, K. Carbon-Doped Anatase TiO2 Powders as a Visible-Light Sensitive Photocatalyst. *Chemistry Letters* **2003**, *32* (8), 772–773.

(162) Woan, K.; Pyrgiotakis, G.; Sigmund, W. Photocatalytic Carbon-Nanotube-TiO 2 Composites. *Advanced Materials* **2009**, *21* (21), 2233–2239.

(163) Tachikawa, T.; Tojo, S.; Kawai, K.; Endo, M.; Fujitsuka, M.; Ohno, T.;

Nishijima, K.; Miyamoto, Z.; Majima, T. Photocatalytic Oxidation Reactivity of Holes in the Sulfur- and Carbon-Doped TiO_2 Powders Studied by Time-Resolved Diffuse Reflectance Spectroscopy. *Journal of Physical Chemistry B* **2004**, *108* (50), 19299–19306.

(164) Aubry, A.; Lei, D. Y.; Fernández-Domínguez, A. I.; Sonnefraud, Y.; Maier, S. A.; Pendry, J. B. Plasmonic Light-Harvesting Devices over the Whole Visible Spectrum. *Nano Letters* **2010**, *10* (7), 2574–2579.

(165) Linic, S.; Christopher, P.; Ingram, D. B. Plasmonic-Metal Nanostructures for Efficient Conversion of Solar to Chemical Energy. *Nature Materials* **2011**, *10* (12), 911–921.

(166) Pu, Y. C.; Wang, G.; Chang, K. Der; Ling, Y.; Lin, Y. K.; Fitzmorris, B. C.; Liu, C. M.; Lu, X.; Tong, Y.; Zhang, J. Z.; et al. Au Nanostructure-Decorated TiO_2 Nanowires Exhibiting Photoactivity across Entire UV-Visible Region for Photoelectrochemical Water Splitting. *Nano Letters* **2013**, *13* (8), 3817–3823.

(167) Awazu, K.; Fujimaki, M.; Rockstuhl, C.; Tominaga, J.; Murakami, H.; Ohki, Y.; Yoshida, N.; Watanabe, T. A Plasmonic Photocatalyst Consisting of Silver Nanoparticles Embedded in Titanium Dioxide. *Journal of the American Chemical Society* **2008**, *130* (5), 1676–1680.

(168) Mubeen, S.; Hernandez-Sosa, G.; Moses, D.; Lee, J.; Moskovits, M. Plasmonic Photosensitization of a Wide Band Gap Semiconductor: Converting Plasmons to

Charge Carriers. *Nano Letters* **2011**, *11* (12), 5548–5552.

(169) Nishijima, Y.; Ueno, K.; Yokota, Y.; Murakoshi, K.; Misawa, H. Plasmon-Assisted Photocurrent Generation from Visible to near-Infrared Wavelength Using a Au-nanorods/TiO_2 Electrode. *Journal of Physical Chemistry Letters* **2010**, *1* (13), 2031–2036.

(170) Lei, D. Y.; Fernández-Domínguez, A. I.; Sonnefraud, Y.; Appavoo, K.; Haglund, R. F.; Pendry, J. B.; Maier, S. a. Revealing Plasmonic Gap Modes in Particle-on-Film Systems Using Dark-Field Spectroscopy. *ACS Nano* **2012**, *6* (2), 1380–1386.

(171) Ji, A.; Sharma, R. P.; Kumari, A.; Pathak, N. K. Numerical Simulation of Solar Cell Plasmonics for Small and Large Metal Nano Clusters Using Discrete Dipole Approximation. *Plasmonics* **2013**, *9* (2), 291–297.

(172) Hu, M.; Chen, J.; Li, Z.-Y.; Au, L.; Hartland, G. V; Li, X.; Marquez, M.; Xia, Y. Gold Nanostructures: Engineering Their Plasmonic Properties for Biomedical Applications. *Chemical Society reviews* **2006**, *35* (11), 1084–1094.

(173) Awazu, K.; Fujimaki, M.; Rockstuhl, C.; Tominaga, J.; Murakami, H.; Ohki, Y.; Yoshida, N.; Watanabe, T. A Plasmonic Photocatalyst Consisting of Sliver Nanoparticles Embedded in Titanium Dioxide. *Journal of Americal Chemical Society*. **2008**, *130* (5), 1676–1680.

(174) Lin, Y. H.; Händel, B.; Huang, H. J.; Chen, H. A.; Chen, Y. F.; Lin, H. N.; Tsai,

D. P. Near-Field Optical Imaging of a Porous Au Film: Influences of Topographic Artifacts and Surface Plasmons. *Plasmonics* **2013**, *8* (2), 377–383.

(175) Mizuno, K.; Ishii, J.; Kishida, H.; Hayamizu, Y.; Yasuda, S.; Futaba, D. N.; Yumura, M.; Hata, K. A Black Body Absorber from Vertically Aligned Single-Walled Carbon Nanotubes. *Proceedings of the National Academy of Sciences of the United States of America* **2009**, *106* (15), 6044–6047.

(176) Kravets, V. G.; Schedin, F.; Grigorenko, a. N. Plasmonic Blackbody: Almost Complete Absorption of Light in Nanostructured Metallic Coatings. *Physical Review B - Condensed Matter and Materials Physics* **2008**, *78* (20), 97–99.

(177) Liu, X.; Tyler, T.; Starr, T.; Starr, A. F.; Jokerst, N. M.; Padilla, W. J. Taming the Blackbody with Infrared Metamaterials as Selective Thermal Emitters. *Physical Review Letters* **2011**, *107* (4), 4–7.

(178) Liu, N.; Mesch, M.; Weiss, T.; Hentschel, M.; Giessen, H. Infrared Perfect Absorber and Its Application as Plasmonic Sensor. *Nano Letters* **2010**, *10* (7), 2342–2348.

(179) Moreau, A.; Ciracì, C.; Mock, J. J.; Hill, R. T.; Wang, Q.; Wiley, B. J.; Chilkoti, A.; Smith, D. R. Controlled-Reflectance Surfaces with Film-Coupled Colloidal Nanoantennas. *Nature* **2012**, *492* (7427), 86–89.

(180) Lee, Y. K.; Jung, C. H.; Park, J.; Seo, H.; Somorjai, G. A.; Park, J. Y. Surface Plasmon-Driven Hot Electron Flow Probed with Metal-Semiconductor

Nanodiodes. *Nano Letters* **2011**, *11* (10), 4251–4255.

(181) Park, J. Y.; Baker, L. R.; Somorjai, G. A. Role of Hot Electrons and Metal–Oxide Interfaces in Surface Chemistry and Catalytic Reactions. *Chemical Reviews* **2015**, *115* (8), 2781–2817.

(182) Clavero, C. Plasmon-Induced Hot-Electron Generation at Nanoparticle/metal-Oxide Interfaces for Photovoltaic and Photocatalytic Devices. *Nature Photonics* **2014**, *8* (2), 95–103.

(183) Lehman, J.; Theocharous, E.; Eppeldauer, G.; Pannell, C. Gold-Black Coatings for Freestanding Pyroelectric Detectors. *Measurement Science and Technology* **2003**, *14* (7), 916–922.

(184) Bian, Z.; Tachikawa, T.; Zhang, P.; Fujitsuka, M.; Majima, T. Au/TiO2 Superstructure-Based Plasmonic Photocatalysts Exhibiting Efficient Charge Separation and Unprecedented Activity. *Journal of the American Chemical Society* **2014**, *136* (1), 458–465.

(185) Englebienne, P. Use of Colloidal Gold Surface Plasmon Resonance Peak Shift to Infer Affinity Constants from the Interactions between Protein Antigens and Antibodies Specific for Single or Multiple Epitopes. *The Analyst* **1998**, *123* (7), 1599–1603.

(186) Ozbay, E. Plasmonics : Merging Photonics and electronics at nanoscale dimensions. *Science* **2006**, *311* (5758), 189–193.

(187) Paris, A.; Vaccari, A.; Lesina, A. C.; Serra, E.; Calliari, L. Plasmonic Scattering by Metal Nanoparticles for Solar Cells. *Plasmonics* **2012**, *7* (3), 525–534.